

Image biomarker standardisation initiative
version 1.5

Alex Zwanenburg Stefan Leger Martin Vallières Steffen Löck
on behalf of the image biomarker standardisation initiative

4th March 2022

The image biomarker standardisation initiative

The image biomarker standardisation initiative (IBSI) is an independent international collaboration which works towards standardisation of image biomarkers. Reproducibility and validation of studies in quantitative image analysis and radiomics is a major challenge for the field (Gillies et al., 2015; Yip and Aerts, 2016; Hatt et al., 2017). The IBSI therefore aims to provide a common nomenclature for image biomarkers, common biomarkers definitions, benchmarks for image processing and feature extraction, as well as reporting guidelines.

Copyright

This work is licensed under the Creative Commons Attribution 4.0 International License. To view a copy of this license, visit <http://creativecommons.org/licenses/by/4.0/> or send a letter to Creative Commons, PO Box 1866, Mountain View, CA 94042, USA.

Contact

Dr. Alex Zwanenburg
alexander.zwanenburg@nct-dresden.de

IBSI contributors

Mahmoud A. Abdalah	Department of cancer imaging and metabolism, Moffitt Cancer Center, Tampa (FL), USA
Hugo Aerts	Computational Imaging and Bioinformatics Laboratory, Dana-Farber Cancer Institute and Harvard Medical School, Harvard University, Cambridge (MA), USA
Aditya Apte	Department of medical physics, Memorial Sloan Kettering Cancer Center, New York (NY), USA
Vincent Andrearczyk	Institute of information systems, University of Applied Sciences Western Switzerland (HES-SO), Vallais-Wallis, Switzerland
Saeed Ashrafinia	Department of radiology and radiological science, School of Medicine, Johns Hopkins University, Baltimore (MD), USA
Jorn Beukinga	Department of nuclear medicine and molecular imaging, University of Groningen, University Medical Center Groningen (UMCG), Groningen, the Netherlands

continued on next page

Ronald Boellaard	Department of nuclear medicine and molecular imaging, University of Groningen, University Medical Center Groningen (UMCG), Groningen, the Netherlands
Marta Bogowicz	Department of radiation oncology, University Hospital Zurich, University of Zurich, Switzerland
Luca Boldrini	Department of radiation oncology, Gemelli ART, Università Cattolica del Sacro Cuore, Rome, Italy
Adrien Depeursinge	Institute of information systems, University of Applied Sciences Western Switzerland (HES-SO), Sierre, Switzerland <i>and</i> Biomedical imaging group, École Polytechnique Fédérale de Lausanne, Lausanne, Switzerland
Marie-Charlotte Desseroit	Laboratory of medical information processing (LaTIM)–team ACTION (image-guided therapeutic action in oncology), INSERM, UMR 1101, University of Brest, IBSAM, Brest France
Nicola Dinapoli	Department of radiation oncology, Gemelli ART, Università Cattolica del Sacro Cuore, Rome, Italy
Cuong Viet Dinh	Imaging technology for radiation therapy group, the Netherlands Cancer Institute (NKI), Amsterdam, the Netherlands
Hesham Elhawalani	Division of radiation oncology, MD Anderson Cancer Center, University of Texas, Houston (TX), USA
Issam El Naqa	Medical physics unit, department of oncology, McGill University, Montreal, Canada
Andriy Y. Fedorov	Surgical Planning Laboratory, Brigham and Women’s Hospital and Harvard Medical School, Harvard University, Cambridge (MA), USA
Nils Gähler	Department of medical image computing, German Cancer Research Center (DKFZ), Heidelberg, Germany
Robert Gillies	Department of cancer imaging and metabolism, Moffitt Cancer Center, Tampa (FL), USA
Michael Götz	Department of medical image computing, German Cancer Research Center (DKFZ), Heidelberg, Germany
Matthias Guckenberger	Department of radiation oncology, University Hospital Zurich, University of Zurich, Switzerland
Mathieu Hatt	Laboratory of medical information processing (LaTIM)–team ACTION (image-guided therapeutic action in oncology), INSERM, UMR 1101, University of Brest, IBSAM, Brest France
Fabian Isensee	Department of medical image computing, German Cancer Research Center (DKFZ), Heidelberg, Germany
Jayashree Kalpathy-Cramer	Athinoula A. Martinos Center for Biomedical Imaging, Massachusetts General Hospital (MGH) and Harvard Medical School, Harvard University, Cambridge (MA), USA
Philippe Lambin	Department of radiation oncology (MAASTRO), GROW–School for Oncology and Developmental Biology, Maastricht University Medical Centre+, Maastricht, the Netherlands
Stefan Leger	OncoRay–National Center for Radiation Research in Oncology, faculty of medicine and university hospital Carl Gustav Carus, Technische Universität Dresden, and Helmholtz-Zentrum Dresden-Rossendorf, Dresden, Germany

continued on next page

Ralph T.H. Leijenaar	Department of Radiation Oncology (The D-lab), GROW–School for Oncology and Developmental Biology, Maastricht University Medical Centre+, Maastricht, the Netherlands
Jacopo Lenkowicz	Department of radiation oncology, Gemelli ART, Università Cattolica del Sacro Cuore, Rome, Italy
Fiona Lippert	Section for biomedical physics, department of radiation oncology, Universitätsklinikum Tübingen, Eberhard Karls University Tübingen, Germany
Steffen Löck	OncoRay–National Center for Radiation Research in Oncology, faculty of medicine and university hospital Carl Gustav Carus, Technische Universität Dresden, and Helmholtz-Zentrum Dresden-Rossendorf, Dresden, Germany
Are Losnegård	Department of clinical medicine, University of Bergen, Bergen, Norway
Dennis S. Mackin	Department of radiation physics, University of Texas MD Anderson Cancer Center, Houston (TX), USA
Klaus H. Maier-Hein	Department of medical image computing, German Cancer Research Center (DKFZ), Heidelberg, Germany
Olivier Morin	Department of radiation oncology, University of California, San Francisco (CA), USA
Arman Rahmim	Department of radiology and radiological science, School of Medicine, Johns Hopkins University, Baltimore (MD), USA
Henning Müller	Institute of information systems, University of Applied Sciences Western Switzerland (HES-SO), Sierre, Switzerland <i>and</i> University Hospital and University of Geneva, Switzerland
Arvind U.K. Rao	Department of bioinformatics and computational biology, The University of Texas MD Anderson Cancer Center, Houston (TX), USA
Christian Richter	OncoRay–National Center for Radiation Research in Oncology, faculty of medicine and university hospital Carl Gustav Carus, Technische Universität Dresden, and Helmholtz-Zentrum Dresden-Rossendorf, Dresden, Germany
Nanna M. Sijtsema	Department of radiation oncology, University of Groningen, University Medical Center Groningen (UMCG), Groningen, The Netherlands
Jairo Socarras Fernandez	Section for biomedical physics, department of radiation oncology, Universitätsklinikum Tübingen, Eberhard Karls University Tübingen, Germany
Emiliano Spezi	Cardiff School of Engineering, Cardiff University, Cardiff, United Kingdom
Roel J.H.M Steenbakkens	Department of radiation oncology, University of Groningen, University Medical Center Groningen (UMCG), Groningen, The Netherlands
Stephanie Tanadini-Lang	Department of radiation oncology, University Hospital Zurich, University of Zurich, Switzerland
Daniela Thorwarth	Section for biomedical physics, department of radiation oncology, Universitätsklinikum Tübingen, Eberhard Karls University Tübingen, Germany

continued on next page

Esther Troost	OncoRay–National Center for Radiation Research in Oncology, faculty of medicine and university hospital Carl Gustav Carus, Technische Universität Dresden, and Helmholtz-Zentrum Dresden-Rossendorf, Dresden, Germany
Taman Upadhaya	Laboratory of medical information processing (LaTIM)–team ACTION (image-guided therapeutic action in oncology), INSERM, UMR 1101, University of Brest, IBSAM, Brest France
Vincenzo Valentini	Department of radiation oncology, Gemelli ART, Università Cattolica del Sacro Cuore, Rome, Italy
Martin Vallières	Laboratory of medical information processing (LaTIM), INSERM, UMR 1101, IBSAM, UBO, UBL, Brest, France <i>and</i> Medical Physics Unit, McGill University, Montréal, Québec, Canada
Uulke van der Heide	Imaging technology for radiation therapy group, the Netherlands Cancer Institute (NKI), Amsterdam, the Netherlands
Lisanne V. van Dijk	Department of radiation oncology, University of Groningen, University Medical Center Groningen (UMCG), Groningen, The Netherlands
Floris H.P. van Velden	Department of radiology, Leiden University Medical Center (LUMC), Leiden, the Netherlands
Joost van Griethuysen	Department of radiology, the Netherlands Cancer Institute (NKI), Amsterdam, the Netherlands
Philip Whybra	Cardiff School of Engineering, Cardiff University, Cardiff, United Kingdom
Alex Zwanenburg	National Center for Tumor Diseases (NCT), partner site Dresden, Germany <i>and</i> OncoRay–National Center for Radiation Research in Oncology, faculty of medicine and university hospital Carl Gustav Carus, Technische Universität Dresden, and Helmholtz-Zentrum Dresden-Rossendorf, Dresden, Germany

Table 1: Alphabetical list of IBSI contributors.

Contents

1 Document changes	1
2 Introduction	3
3 Image processing	4
3.1 Data conversion	4
3.2 Image post-acquisition processing	6
3.3 Segmentation	6
3.4 Interpolation	8
3.5 Re-segmentation	13
3.6 ROI extraction	14
3.7 Grey level discretisation	14
3.8 Feature calculation	17
4 Image features	18
4.1 Morphological features	19
4.2 Local intensity features	28
4.3 Intensity-based statistical features	28
4.4 Intensity histogram features	31
4.5 Intensity-volume histogram features	36
4.6 Texture features - Grey level co-occurrence based features	38
4.7 Texture features - Grey level run length based features	47
4.8 Texture features - Grey level size zone based features	51
4.9 Texture features - Grey level distance zone based features	55
4.10 Texture features - Neighbourhood grey tone difference based features	60
4.11 Texture features - Neighbouring grey level dependence based features	63
5 Novel and uncommon imaging features	69
5.1 Texture features - Distance weighted texture matrices	69
5.2 Texture features - Neighbourhood grey level co-occurrence matrix	70
5.3 Texture features - Extended emphasis features	70
6 Reporting guidelines	72
7 Benchmarking data sets	74
7.1 Digital phantom	74
7.2 Patient data	75

Chapter 1

Document changes

The following is a list of changes to the document from previous versions.

Version 1.5 – current

- Added sections on the benchmark data sets and reporting guidelines from the IBSI internal work document.
- Added notes on numerical precision for voxel and ROI representations.
- The section on discretisation was mostly restructured.
- Added table with recommended interactions between image, re-segmentation and discretisation.
- Rewritten the intensity-volume histogram section for better clarity. Beware of discretisation definitions and how this affects the calculation of the intensity-volume histogram.
- Added notes on the equivalence of GLCM *sum variance* and *cluster tendency* features, of *difference average* and *dissimilarity* and the direct relationship between *sum average* and *joint average* features. Another note was added to note the potential equivalence of IH *uniformity* and NGLDM *grey level non-uniformity normalised* features.
- Revised and updated wording and notation throughout the document.

Version 1.4

- Removed spatial filtering from the image processing section. This may be investigated at a later time.
- Swapped position of distance zone matrix and neighbourhood grey tone difference matrix (NGTDM) sections.
- Added note on NGTDM voxels without any valid neighbours.
- Changed font type from *Computer Modern Roman* to *New Century Schoolbook* for better readability.

- Added chapter on image processing from the IBSI internal work document.
- Reintroduced *approximate volume* for consistency with common clinical volume calculation.
- Updated description of intensity-volume histogram feature family.
- Updated section on novel and uncommon imaging features.

Version 1.3

- Updated and revised definitions of morphological features to handle inconsistencies due to mixed voxel representations. Notably *volume* is now calculated from the ROI mesh instead of directly from the ROI voxels. Likewise, *diameter*, *volume density* and *area density* features are (where possible) based on vertices of the ROI mesh, instead of the voxel centre point set. The introductory description of the morphological feature set was updated to introduce nomenclature and definitions used in meshes.
- Added *approximate volume* feature, which captures tumour volume based on voxel counts.
- Added figures to show feature calculation process for texture features.
- Clarified definitions for *Neighbourhood grey tone difference matrix*-based features.

Version 1.2

- Updated the section on *Intensity volume histogram*-based features.
- Updated description for the local intensity feature set.
- Updated the description of the *area density - approximate enclosing ellipsoid* to provide a maximum degree for the Legendre polynomials.
- Updated the description of the *volume density - minimum volume enclosing ellipsoid* to provide a stopping tolerance for Khachiyan's method.
- Feature sets are ordered differently. The morphological features are now presented first, followed by local intensity features and statistical features.
- Fixed various typos.

Version 1.1

- Fixed errors in the definition of *dependence count energy* feature.
- Fixed errors in the definitions of *major axis length*, *minor axis length* and *least axis length* features.
- Updated descriptions of the *volume density - approximate enclosing ellipsoid* and *area density - approximate enclosing ellipsoid* features.
- Added descriptions of the *volume density - minimum volume enclosing ellipsoid* and *area density - minimum volume enclosing ellipsoid* features.
- Fixed errors in layout.

Chapter 2

Introduction

Biomarkers are single-value representations relevant to a biological process. Biomarkers may come from a wide variety of sources, such as gene expressions, clinical records and medical images. The latter are often referred to as imaging biomarkers. Imaging biomarkers consist of both qualitative biomarkers, which require subjective interpretation, and quantitative biomarkers which are based on mathematical definitions and are directly based on the image itself. The latter we refer to as image biomarkers. Image biomarkers characterise (regions of) an image, such as volume or mean intensity. Because of the historically close relationship with the computer vision field, image biomarkers are also called image features. The term *features*, instead of biomarkers, will be used throughout the document, as the contents are generally applicable and not limited to life sciences specifically.

Images require processing before image features can be calculated. A basic image processing framework is proposed and detailed in **Chapter 3**. These image processing steps are later benchmarked so that software implementations may be checked.

Image feature definitions are described in **Chapter 4**. These image features are later benchmarked so that software implementations may be checked.

During the work of the Image Biomarker Standardisation Initiative, a number of novel and uncommon texture features were likewise identified. While these are not benchmarked, their definitions are included in **Chapter 5**.

Reporting on image processing and image feature extraction increases reproducibility of findings. Reporting guidelines are described in **Chapter 6** for this purpose.

The benchmark data used for benchmarking image processing and feature extraction are described in **Chapter 7**. The respective benchmark values are listed in **Chapter ??**.

Chapter 3

Image processing

Image processing is the sequence of operations required to derive image biomarkers (features) from images. In this work we focus on the extraction of features from a region of interest (ROI) segmented in an image.

Image processing may be conducted using a wide variety of schemes. We therefore designed a general image processing scheme for image feature calculation based on various schemes used within scientific literature. The image processing scheme is shown in figure 3.1. The processing steps referenced in the figure are described below.

The process leading from a medical image to a set or overlay of image features can be viewed as a sequence of operations on the image data, such as segmentation, interpolation and discretisation. Our starting point is the image stack as read from e.g. a series of DICOM or NIFTI files. Various other sources of variability exist, such as acquisition protocol, scanner type, quantitative corrections and image reconstruction algorithms. Since these are often vendor-specific, and/or standardised elsewhere e.g. (Boellaard et al., 2015), these will not be treated here.

3.1 Data conversion

Some imaging modalities, notably positron emission tomography (PET), require conversion of image data into a more meaningful presentation.

SUV Activity due to uptake of the PET tracer fluid is converted to a standardised uptake value (SUV) in each voxel. SUV is commonly defined as (Boellaard et al., 2010):

$$SUV_k = \frac{A_k}{A_{adm}/BM}$$

Here, A_k is the activity in kBq/ml in voxel k measured by PET. A_{adm} is the administered activity in MBq, corrected for activity loss due to time between administration and image acquisition and tracer losses during administration. Thus

$$A_{adm} = \left(A_0 - A_{loss} (1/2)^{-\frac{\Delta t_{loss}}{t_{1/2}}} \right) (1/2)^{\frac{\Delta t_{acq}}{t_{1/2}}}$$

A_0 is the initially measured activity in MBq. A_{loss} is the loss in activity due to administration, measured at t_{loss} . Hence the first factor represent the activity of the injected volume

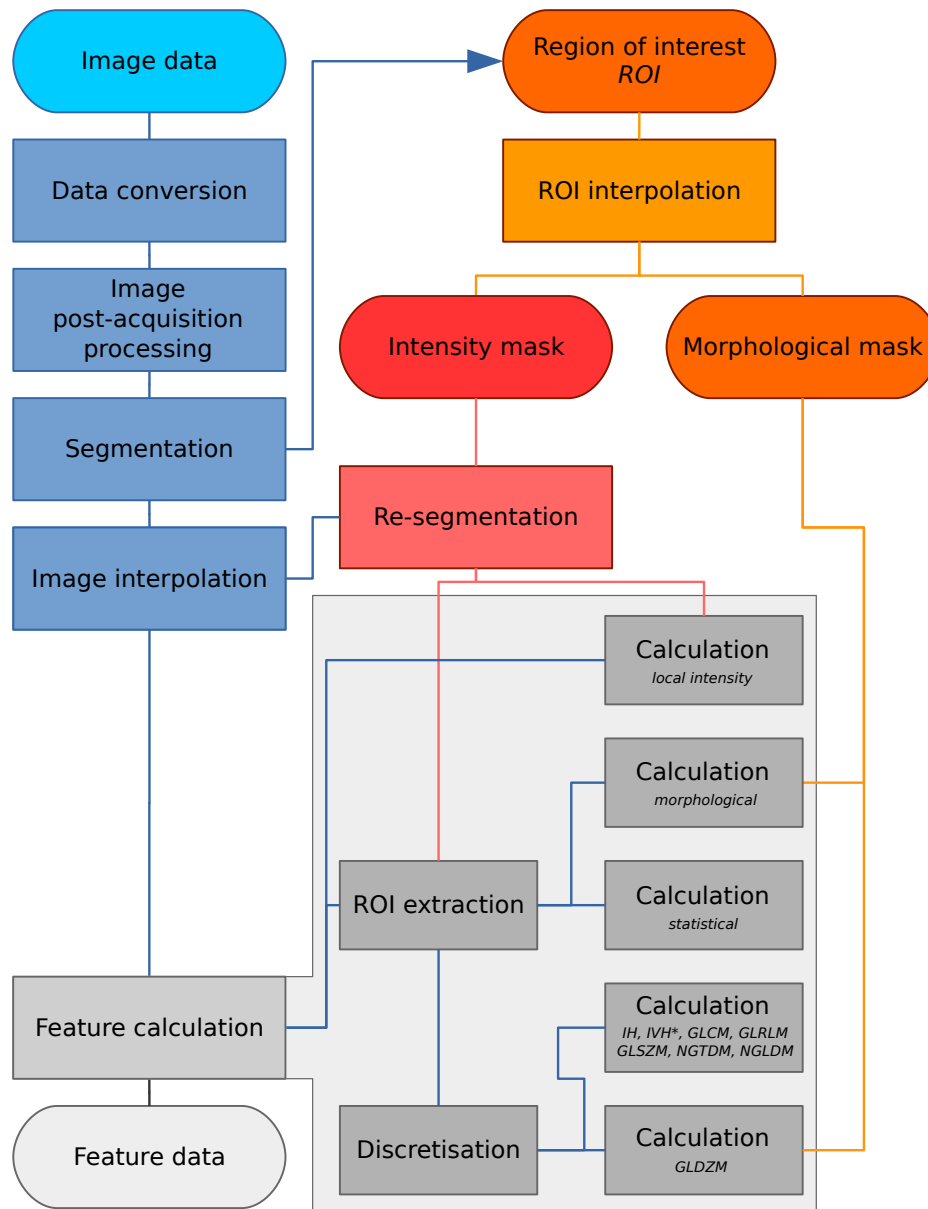


Figure 3.1: Image processing scheme for image biomarker calculation. Depending on the specific imaging modality and purpose, some steps may be omitted. The region of interest (ROI) is explicitly split into two masks, namely an intensity and morphological mask, after interpolation to the same grid as the interpolated image. Feature calculation is expanded to show the different feature families with specific pre-processing. IH: intensity histogram; IVH: intensity-volume histogram; GLCM: grey level cooccurrence matrix; GLRLM: grey level run length matrix; GLSZM: grey level size zone matrix; NGTDM: neighbourhood grey tone difference matrix; NGLDM: Neighbouring grey level dependence matrix; GLDZM: grey level distance zone matrix; *Discretisation of IVH differs from IH and texture features, see section 4.5.

at time 0. Δt_{acq} is the time between initial activity measurement and image acquisition and $t_{1/2}$ the half life of the tracer isotope. BM is the patients body mass in kg.

A plasma glucose correction to SUV may be applied (Boellaard et al., 2010):

$$SUV_{gluc,k} = SUV_k \frac{C_{gluc,plasma}}{5.0}$$

Here, $C_{gluc,plasma}$ is the glucose concentration in the plasma in mmol/l.

SUL (Boellaard et al., 2015) recommended additional calculation of standard uptake value normalised to lean body mass (SUL). SUL is defined as:

$$SUL_k = \frac{A_k}{A_{adm}/LBM}$$

Lean body mass (LBM) is defined as (Janmahasatian et al., 2005):

$$LBM = \begin{cases} \frac{9270 BM}{6680 + 216 (BM/h^2)} & \text{if male} \\ \frac{9270 BM}{8780 + 244 (BM/h^2)} & \text{if female} \end{cases}$$

h is the patient height in meters. The factor BM/h^2 is thus equal to the body mass index (BMI) of the patient.

As with SUV, a plasma glucose may be applied:

$$SUL_{gluc,k} = SUL_k \frac{C_{gluc,plasma}}{5.0}$$

3.2 Image post-acquisition processing

Images are post-processed to enhance image quality. For instance, MRI contains both Gaussian and Rician noise (Gudbjartsson and Patz, 1995) and may benefit from denoising. As another example, intensities measured using MR may be non-uniform across an image and could require correction (Sled et al., 1998). FDG-PET-based may furthermore be corrected for partial volume effects (Soret et al., 2007; Boussion et al., 2009). In CT imaging, metal objects, e.g. pacemakers and tooth implants, introduce artifacts and may require artifact suppression (Gjesteby et al., 2016). Evaluation and standardisation of various image post-acquisition processing methods falls outside the scope of the current work.

3.3 Segmentation

Radiomics analysis, within the current paradigm, relies on the definition of regions of interest (ROIs). These ROIs represent anatomical structures, such as a tumour volume or organs at risk, and are used to define areas or volumes from which image features are calculated. ROIs can be defined manually by experts or automatically by algorithms. A review of the numerous segmentation methods and their merits is beyond the scope of this work.

From a process point-of-view, segmentation leads to the creation of a ROI mask R , for which every voxel $j \in R$ (R_j) is defined as:

$$R_j = \begin{cases} 1 & j \text{ in ROI} \\ 0 & \text{otherwise} \end{cases}$$

An example is shown in figure 3.2.

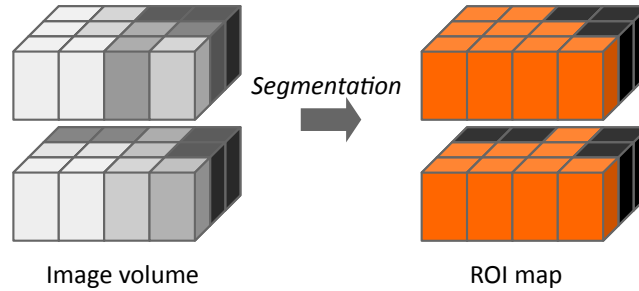


Figure 3.2: Segmentation of the image volume leads to the creation of a region of interest (ROI). In this example, segmentation is performed by excluding voxels with $> 50\%$ grey from the ROI. All orange voxels in the ROI are considered to be part of the ROI, while black voxels are excluded.

ROIs are typically saved with the corresponding image. Some image formats directly store ROI masks as voxels (e.g. NIfTI and NRRD), and generating the ROI mask is conducted by loading the corresponding image. In other cases such as DICOM RTstruct files, the ROI is saved as a set of XYZ points defining closed loops of (planar) polygons. Defining the ROI mask then consists of determining which voxel centers lie within the space enclosed by the contour polygon in each slice.

A common method to determine whether a point in an image slice lies in a 2D polygon is the *crossing number* algorithm, for which a number of implementations exists (Schirra, 2008). The main concept of this algorithm is that for any point inside the polygon, any line originating outside the polygon will cross the polygon an uneven number of times. A simple example is shown in Figure 3.3. The example implementation makes use of the fact that the ROI mask is a regular grid to scan entire rows at a time. The contour polygon is considered to be composed of a connected set of edges. The simple implementation consists of the following steps:

1. (optional) A ray is cast horizontally from outside the polygon for each of the n image rows. As we iterate over the rows, it is computationally beneficial to exclude polygon edges that will not be crossed by the ray for the current row j . If the current row has y -coordinate y_j , and edge k has two vertices with y -coordinates y_{k1} and y_{k2} , the ray will not cross the edge if both vertices lie either above or below y_j , i.e. $y_j < y_{k1}, y_{k2}$ or $y_j > y_{k1}, y_{k2}$. For each row j , find those polygon edges whose y -component of the vertices do not both lie on the same side of the row coordinate y_j . This step is used to limit calculation of intersection points to only those that cross a ray cast from outside the polygon – e.g. ray with origin $(-1, y_j)$ and direction $(1, 0)$. This an optional step.
2. Determine intersection points x_i of the (remaining) polygon edges with the ray.
3. Iterate over intersection points and add 1 to the count of each pixel center with $x \geq x_i$.
4. Apply even-odd rule. Pixels with an odd count are inside the polygon, whereas pixels with an even count are outside.

Note that the example represents a relatively naive implementation that will not consistently assign voxel centers positioned on the polygon itself to the interior.

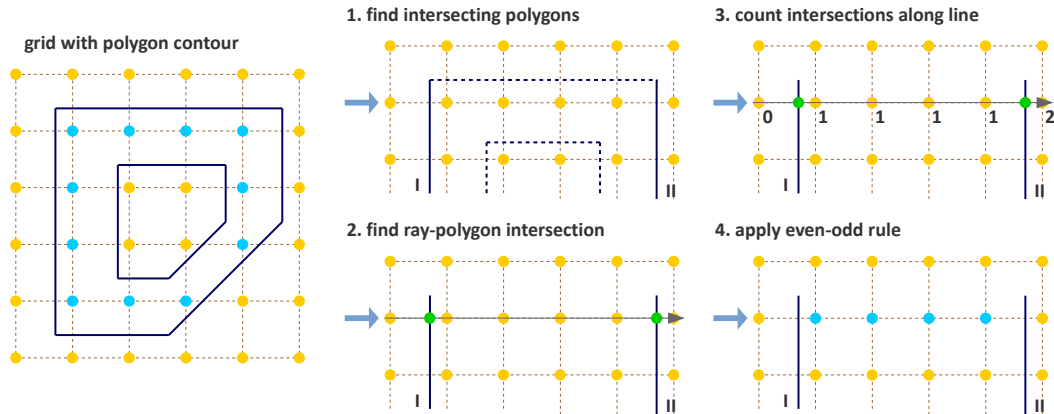


Figure 3.3: Simple algorithm to determine which pixels are inside a 2D polygon. The suggested implementation consists of four steps: (1) Omit edges that will not intersect with the current row of voxel centers. (2) Calculate intersection points of edges I and II with the ray for the current row. (3) Determine the number of intersections crossed from ray origin to the row voxel centers. (4) Apply even-odd rule to determine whether voxel centers are inside the polygon.

3.4 Interpolation

Texture feature sets require interpolation to isotropic voxel sizes to be rotationally invariant, and to allow comparison between image data from different patients. Voxel interpolation affects image feature values as many image features are sensitive to changes in voxel size (Yan et al., 2015; Shafiq-Ul-Hassan et al., 2017). Maintaining consistent isotropic voxel dimensions across different patients and institutions is therefore important for reproducibility. The isotropic voxel dimension depends on the imaging modality used for image acquisition. At the moment there are no clear indications whether upsampling or downsampling schemes are preferable. Consider, for example, an image stack of slices with $1.0 \times 1.0 \times 3.0 \text{ mm}^3$ voxels. Down-sampling ($1.0 \times 1.0 \times 1.0 \text{ mm}^3$) requires inference and introduces artificial information, while conversely upsampling to the largest dimension ($3.0 \times 3.0 \times 3.0 \text{ mm}^3$) incurs information loss.

While in general we consider three-dimensional (3D) interpolation for an image stack, two-dimensional (2D) voxel interpolation within the image slice plane may be recommended in some situations. In 2D, voxels are not interpolated between slices. For example, if slice thickness is large compared to in-plane voxel dimensions, a 2D approach may be preferable, as applying 3D interpolation would either require inferencing a large number of voxels between slices, or the loss of a large fraction of in-plane information. However, the disadvantage of using the 2D approach is that the distance parameters are not anymore equivalent in the three directions of space and that rotation invariance is lost.

Interpolation algorithms. Interpolation algorithms translate the grey level values from the original grid to an interpolation grid in a different space. In such grids, voxels are spatially represented by their center. A number of algorithms are available for interpolation. Common choices are *nearest neighbour*, *trilinear*, *tricubic convolution* and *tricubic spline*

interpolation. In short, *nearest neighbour interpolation* assigns grey levels in the output grid to the values of the closest voxels in the input grid. *Trilinear interpolation* uses the eight closest voxels in the input grid to calculate the new grey level value using linear interpolation. *Tricubic convolution* and *tricubic spline interpolation* draw upon a larger neighbourhood to evaluate a smooth, continuous third-order polynomial at the points of the output grid. The difference between *tricubic convolution* and *tricubic spline interpolation* lies in the implementation. Whereas *tricubic spline interpolation* evaluates the smooth and continuous third-order polynomial at every point, *tricubic convolution* approximates the solution using a convolution filter. Though *tricubic convolution* is faster, with modern hardware and common image sizes, the difference in execution speed is practically meaningless. Both interpolation algorithms produce similar results, and both are often referred to as *tricubic interpolation*.

While no consensus exists concerning the optimal choice of interpolation algorithm, *trilinear interpolation* is a conservative choice. It does not lead to the blockiness produced by *nearest neighbour interpolation*, and does not lead to out-of-range grey values which may occur due to overshoot with *tricubic* and higher order interpolations. The latter problem can occur in acute transitions in grey levels, where the local neighbourhood itself is not sufficiently smooth to evaluate the polynomial within the allowed range. *Tricubic* methods, however, may retain tissue contrast differences better. In a phantom study, Larue et al. (2017) compared *nearest neighbour*, *trilinear* and *tricubic* interpolation and indicated that feature reproducibility is dependent on the selected interpolation algorithm, i.e. some features were more reproducible using one particular algorithm.

Image intensities may require rounding after interpolation, or the application of cut-off values. For example, in CT images grey levels represent Hounsfield Units, and these do not take non-integer values. Following voxel interpolation, interpolated CT grey levels are thus rounded to the nearest integer.

Voxel interpolation also requires interpolation of the ROI mask R to the same dimensions as the interpolated image. Interpolation of the ROI mask is best conducted using either the *nearest neighbour* and *trilinear interpolation* methods, as these are guaranteed to produce meaningful masks. *Trilinear interpolation* of the ROI mask leads to partial volume effects, with some voxels containing fractions of the original voxels. Since the ROI mask is a binary mask, such fractions need to be binarised by setting a partial volume threshold δ :

$$R_j = \begin{cases} 1 & R_{interp,j} \geq \delta \\ 0 & R_{interp,j} < \delta \end{cases}$$

A common choice for the partial volume threshold is $\delta = 0.5$. For *nearest neighbour interpolation* the ROI mask does not contain partial volume fractions, and may be used in its entirety.

Interpolation furthermore depends on the floating point representation used for the image and ROI masks. Floating point representations should at least be full precision (32-bit) to avoid rounding errors.

Interpolation grid. Interpolated voxel centers lie on a regular mesh grid. Coordinates of a mesh grid are represented by two coordinate systems. The first coordinate system is the grid coordinate system, with origin at (0.0, 0.0, 0.0) and distance between directly neighbouring voxel centers (spacing) of 1.0. The grid coordinate system is the coordinate system typically used by computers, and consequentially, by interpolation algorithms. The second

coordinate system is the world coordinate system, which is typically found in (medical) imaging and provides an image scale. As the desired isotropic spacing is commonly defined in world coordinate dimensions, conversions between world coordinates and grid coordinates are necessary, and are treated in more detail after assessing grid alignment methods.

Grid alignment affects feature values and is non-trivial. Three common grid alignments may be identified, and are shown in Figure 3.4:

1. **Fit to original grid.** In this case the interpolation mesh grid is deformed so that the voxel centers at the grid vertices overlap with the original grid vertices. For an original 4×4 voxel grid with spacing $(3.00, 3.00)$ mm and a desired interpolation spacing of $(2.00, 2.00)$ mm we first calculate the extent of the original voxel grid in world coordinates leading to an extent of $((4 - 1) 3.00, ((4 - 1) 3.00) = (9.00, 9.00)$ mm. In this case the interpolated grid will not exactly fit the original grid. Therefore we try to find the closest fitting grid, which leads to a 6×6 grid by rounding up $(9.00/2.00, 9.00/2.00)$. The resulting voxel grid has a grid spacing of $(1.80, 1.80)$ mm in world coordinates, significantly differing from the desired grid spacing of $(2.00, 2.00)$ mm.
2. **Align grid origins** A simple approach which conserves the desired grid spacing is the alignment of the origins of the interpolation and original grids. Keeping with the same example, the interpolation grid is (6×6) . The resulting voxel grid has a grid spacing of $(2.00, 2.00)$ mm in world coordinates. By definition both grids are aligned at the origin, $(0.00, 0.00)$.
3. **Align grid centers.** An implementation-independent solution is to align both grids on the grid center. Again, keeping with the same example, the interpolation grid is (6×6) . Again, the resulting voxel grid has a grid spacing of $(2.00, 2.00)$ mm in world coordinates.

Alignment by center. is preferred as it is implementation-independent and achieves the desired voxel spacing. Technical details of implementing *alignment by center* are described below.

Determining interpolation grid dimensions. The dimensions of the interpolation grid are determined as follows. Let n_a be the number of points along one axis of the original grid and $s_{a,w}$ their spacing in world coordinates. Then, let $s_{b,w}$ be the desired spacing after interpolation. The axial dimension of the interpolated mesh grid is then:

$$n_b = \lceil \frac{n_a s_a}{s_b} \rceil$$

Rounding towards infinity guarantees that the interpolation grid exists even when the original grid contains few voxels. However, it also means that the interpolation mesh grid partially falls outside of the original grid and thus is extrapolated. Padding the original grid with the voxel values at the borders is recommended. Some implementations of interpolation algorithms may perform padding internally.

Determining interpolation grid position. For the *align grid centers* method, the positions of the interpolation grid points are determined as follows. As before, let n_a and n_b be the dimensions of one axis in the original and interpolation grid, respectively. Moreover, let

$s_{a,w}$ be the original spacing and $s_{b,w}$ the desired spacing for the same axis in world coordinates. Then, with $x_{a,w}$ the origin of the original grid in world coordinates, the origin of the interpolation grid is located at:

$$x_{b,w} = x_{a,w} + \frac{s_a(n_a - 1) - s_b(n_b - 1)}{2}$$

In the grid coordinate system, the original grid origin is located at $x_{a,g} = 0$. The origin of the interpolation grid is then located at:

$$x_{b,g} = \frac{1}{2} \left(n_a - 1 - \frac{s_{b,w}}{s_{a,w}} (n_b - 1) \right)$$

Here the fraction $s_{b,w}/s_{a,w} = s_{b,g}$ is the desired spacing in grid coordinates. Thus, the interpolation grid points along the considered axis are located at grid coordinates:

$$x_{b,g}, x_{b,g} + s_{b,g}, x_{b,g} + 2s_{b,g}, \dots, x_{b,g} + (n_b - 1)s_{b,g}$$

Naturally, the above description applies to every grid axis.

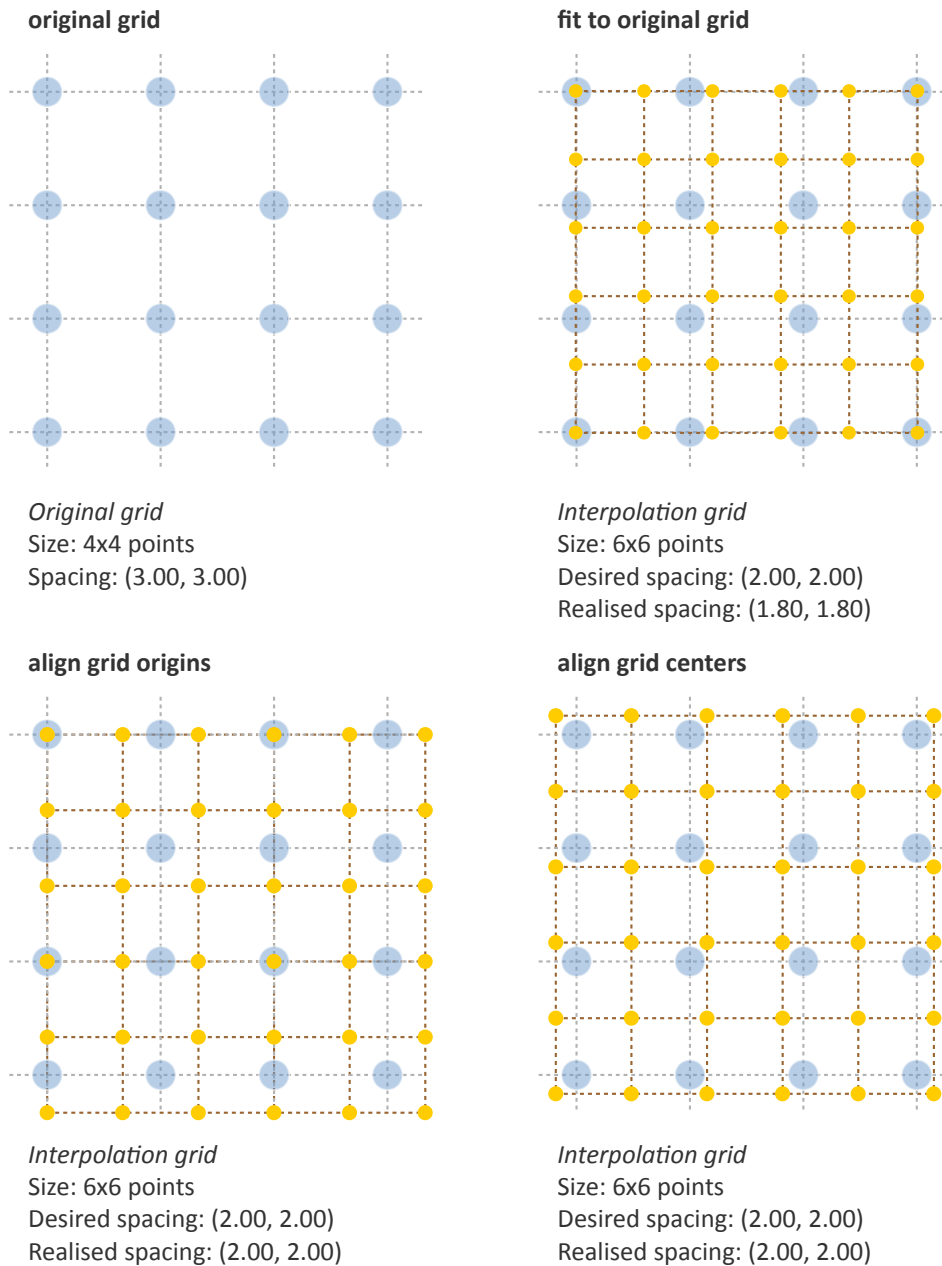


Figure 3.4: Different interpolation mesh grids based on an original 4×4 grid with (3.00, 3.00) mm spacing. The desired interpolation spacing is (2.00, 2.00) mm. *Fit to original grid* creates an interpolation mesh grid that overlaps with the corners of the original grid. *Align grid origins* creates an interpolation mesh grid that is positioned at the origin of the original grid. *Align grid centers* creates an interpolation grid that is centered on the center of original and interpolation grids.

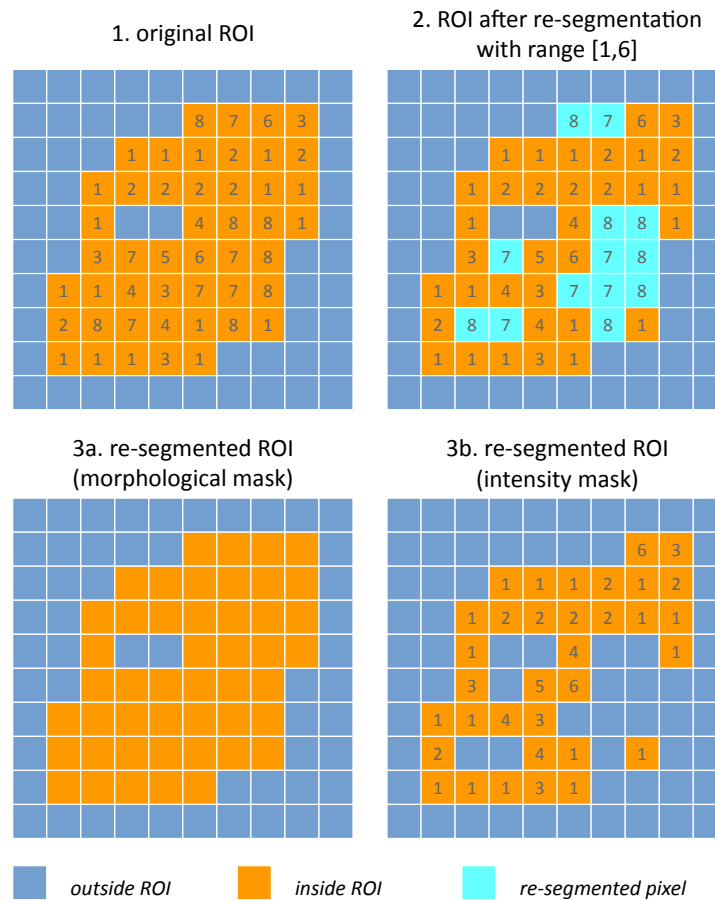


Figure 3.5: Example showing how intensity and morphological masks may differ due to re-segmentation. (1) The original region of interest (ROI) is shown with pixel intensities. (2) Subsequently, the ROI is re-segmented to only contain values in the range [1, 6]. Pixels outside this range are marked for removal from the intensity mask. (3a) Resulting morphological mask, which is identical to the original ROI. (3b) Re-segmented intensity mask. Note that due to re-segmentation, intensity and morphological masks are different.

3.5 Re-segmentation

Re-segmentation entails updating the ROI mask \mathbf{R} based on corresponding voxel intensities X_{gl} . Re-segmentation may be performed to exclude voxels from a previously segmented ROI, and is performed after interpolation.

Intensity and morphological masks of a ROI Conventionally, a ROI consists of a single mask. However, re-segmentation may lead to exclusion of internal voxels, or divide the ROI into sub-volumes. To avoid undue complexity by again updating the re-segmented ROI for a more plausible morphology, we define two separate ROI masks. The morphological mask is not re-segmented and maintains the original morphology as defined by an ex-

pert and/or (semi-)automatic segmentation algorithms. The intensity mask is re-segmented and will only contain selected voxels. For many feature families, only the intensity mask is important. However, for morphological and grey level distance zone matrix (GLDZM) feature families, both intensity and morphological masks are used. A two-dimensional example is shown in Figure 3.5.

Two common re-segmentation methods are described below. Combining multiple re-segmentation methods is possible.

Range re-segmentation. Re-segmentation may be performed to remove voxels from the intensity mask that fall outside of a specified range. An example is the exclusion of voxels with Hounsfield Units indicating air and bone tissue in the tumour ROI within CT images, or low activity areas in PET images. Such ranges of intensities of included voxels are usually presented as a closed interval $[a, b]$ or half-open interval $[a, \infty)$, respectively. For arbitrary intensity units (e.g. raw MRI data and many spatial filters), no re-segmentation range can be provided.

When a re-segmentation range is defined by the user, it needs to be propagated and used for the calculation of features that require a specified intensity range (e.g. intensity-volume histogram features) and/or that employs *fixed bin size* discretisation. Recommendations for the possible combinations of different imaging intensity definitions, re-segmentation ranges and discretisation algorithms are provided in Table 3.1.

Intensity outlier filtering. ROI voxels with outlier intensities may be removed from the intensity mask. One method for defining outliers was suggested by Vallières et al. (2015) after Collewet et al. (2004). The mean μ and standard deviation σ of grey levels of voxels assigned to the ROI are calculated. Voxels outside the range $[\mu - 3\sigma, \mu + 3\sigma]$ are subsequently excluded from the intensity mask.

3.6 ROI extraction

Many feature families require that the ROI is isolated from the surrounding voxels. The ROI intensity mask is used to extract the image volume to be studied. Excluded voxels are commonly replaced by a placeholder value, often *NaN*. This placeholder value is then used to exclude these voxels from calculations. Voxels included in the ROI mask naturally retain their original grey level value.

3.7 Grey level discretisation

Grey level discretisation or quantisation of the ROI is often required to make calculation of texture features tractable (Yip and Aerts, 2016), and has noise-suppressing properties as well. An example of discretisation is shown in Figure 3.6.

Two approaches to discretisation are commonly used. One involves the discretisation to a fixed number of bins, and the other discretisation with a fixed bin width. As we will observe, there is no inherent preference for one or the other method. However, both methods have particular characteristics (as described below) that may make them better suited for specific purposes. Note that the lowest bin always has value 1, and not 0. This ensures consistency for calculations of texture features, where grey level 0 is not allowed for some features.

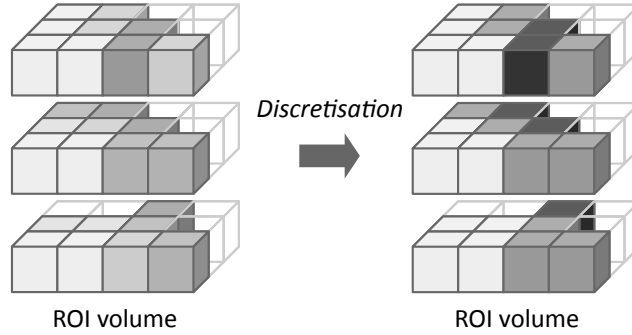


Figure 3.6: The image volume contained in the region of interest (ROI) is discretised. Here, grey levels from the original ROI volume were assigned to 3 intensity bins to create a discretised volume.

Fixed bin number. In the *fixed bin number* method, grey levels X_{gl} are discretised to a fixed number of N_g bins. It is defined as follows:

$$X_{d,k} = \begin{cases} 1 & X_{gl,k} = X_{gl,min} \\ \lceil N_g \frac{X_{gl,k} - X_{gl,min}}{X_{gl,max} - X_{gl,min}} \rceil & X_{gl,k} > X_{gl,min} \end{cases}$$

In short, the grey level $X_{gl,k}$ of voxel k is corrected by the lowest occurring grey level $X_{gl,min}$ in the ROI, divided by the bin width $(X_{gl,max} - X_{gl,min})/N_g$, and subsequently rounded up to the nearest integer.

The *fixed bin number* method breaks the relationship between image intensity and physiological meaning (if any). However, it introduces a normalising effect which may be beneficial when intensity units are arbitrary (e.g. raw MRI data and many spatial filters), and where contrast is considered important. Furthermore, as the absolute values of many features are dependent on the number of grey levels X_{gl} within a given ROI, using a *fixed bin number* discretisation algorithm allows for a direct comparison of feature values across multiple analysed ROIs (e.g. across different patients).

Fixed bin size. *Fixed bin size* discretisation is conceptually simple. A new bin is assigned every w_b grey levels; i.e. w_b is the bin width, starting at a minimum $X_{gl,min}$. The minimum may be a user-set value as defined by the lower bound of the re-segmentation range, or data-driven as defined by the minimum grey level in the ROI $X_{gl,min} = \min(X_{gl})$. In all cases, the method used and/or set minimum value must be clearly reported. However, to maintain consistency between subjects, we strongly recommend to always set the same minimum value for all subjects as defined by the lower bound of the re-segmentation range (e.g. HU of -500 for CT, SUV of 0 for PET, etc.). In the case that no re-segmentation range may be defined due to arbitrary intensity units (e.g. raw MRI data and many spatial filters), the use of the *fixed bin size* discretisation algorithm is not recommended.

Discretisation using the *fixed bin size* method proceeds as follows:

$$X_{d,k} = \begin{cases} 1 & X_{gl,k} = X_{gl,min} \\ \lceil \frac{X_{gl,k} - X_{gl,min}}{w_b} \rceil & X_{gl,k} > X_{gl,min} \end{cases}$$

The *fixed bin size* method has the advantage of maintaining a direct relationship with

the original intensity scale, which could be useful for functional imaging modalities such as PET.

Other methods. Many other methods and variations for discretisation exist. Vallières et al. (2015) described the use of *intensity histogram equalisation* and *Lloyd-Max* algorithms for discretisation. *Intensity histogram equalisation* involves redistributing grey levels so that the resulting bins contain a similar number of voxels, i.e. contrast is increased by flattening the histogram as much as possible (Hall et al., 1971). The *Lloyd-Max* algorithm is an iterative clustering method that seeks to minimise mean squared discretisation errors (Max, 1960; Lloyd, 1982).

A comparison of discretisation methods. As mentioned earlier, the discretisation method that leads to best feature inter- and intra-patient reproducibility is modality-dependent. Recommendations for the possible combinations of different imaging intensity definitions, re-segmentation ranges and discretisation algorithms are provided in Table 3.1.

The effect of the number of bins for *fixed bin number* discretisation was studied by Hatt et al. (2015), in a large methodological study with 555 pretreatment FDG-PET images covering a range of different tumours. They found that *fixed bin number* discretisation using 64 bins provides the best compromise between differentiation and resolution.

Leijenaar et al. (2015) compared the effect of *fixed bin size* and *fixed bin number* discretisation methods on texture features from FDG-PET images recorded in a cohort of 35 non-small cell lung cancer patients. They concluded that *fixed bin size* may be more appropriate for inter- and intra-patient comparison of texture feature values in a clinical setting.

In another methodological study van Velden et al. (2016) also assessed the effect of *fixed bin number* versus *fixed bin size* methods. They concluded that texture features from FDG-PET images had better repeatability and lower sensitivity to delineation changes using the *fixed bin size* discretisation method.

It should also be noted that several studies have used *fixed bin size* for CT images, e.g. (Aerts et al., 2014; van Dijk et al., 2017). Both studies used a bin size of 25 HU. However, the authors of both studies did not report on the minimum grey level used in the discretisation process, which essentially precludes the reproducibility of their findings.

Imaging intensity units ⁽¹⁾	Re-segmentation range	FBN ⁽²⁾	FBS ⁽³⁾
definite	$[a, b]$	✓	✓
	$[a, \infty)$	✓	✓
	none	✓	×
arbitrary	none	✓	×

Table 3.1: Recommendations for the possible combinations of different imaging intensity definitions, re-segmentation ranges and discretisation algorithms. Checkmarks (✓) represent recommended combinations of re-segmentation range and discretisation algorithm, whereas crossmarks (×) represent non-recommended combinations.

⁽¹⁾ PET and CT are examples of imaging modalities with *definite* intensity units (e.g. SUV and HU, respectively), and raw MRI data of arbitrary intensity units.

⁽²⁾ *Fixed bin number* (FBN) discretisation uses the actual range of intensities in the analysed ROI (re-segmented or not), and not the re-segmentation range itself (when defined).

⁽³⁾ *Fixed bin number* (FBS) discretisation uses the lower bound of the re-segmentation range as the minimum set value. When the re-segmentation range is not or cannot be defined (e.g. arbitrary intensity units), the use of the FBS algorithm is not recommended.

3.8 Feature calculation

Feature calculation is the final processing step where feature descriptors are used to quantify characteristics of the ROI. After calculation such features may be used as image biomarkers by relating them physiological and medical outcomes of interest. Feature calculation is handled in full details in the next chapter.

Let us recall that the image processing steps leading to image biomarker calculations can be performed in many different ways, notably in terms of spatial filtering, segmentation, interpolation and discretisation parameters. Furthermore, it is plausible that different texture features will better quantify the characteristics of the ROI when computed using different image processing parameters. For example, a lower number of grey levels in the discretisation process (e.g. 8 or 16) may allow to better characterize the sub-regions of the ROI using *grey level size zone matrix* (GLSZM) features, whereas *grey level co-occurrence matrix* (GLCM) features may be better modeled with a higher number of grey levels (e.g. 32 or 64). Overall, these possible differences opens the door to the optimization of image processing parameters for each different feature in terms of a specific endgoal. For the specific case of the optimization of image interpolation and discretisation prior to texture analysis, Vallières et al. (2015) have named this process *texture optimization*. The authors notably suggested that the *texture optimization* process could have significant influence of the prognostic capability of subsequent features. In another study, Vallières et al. (2017) constructed predictive models using textures calculated from all possible combinations of PET and CT images interpolated at four isotropic resolutions and discretised with two different algorithms and four numbers of grey levels.

Chapter 4

Image features

In this chapter we will describe a set of quantitative image features. The feature set presented here largely builds upon the feature sets proposed by Aerts et al. (2014) and Hatt et al. (2017), which are themselves largely derived from earlier works. References to earlier work are provided where possible.

The set of features can be divided into a number of families, of which intensity-based statistical, intensity histogram-based, intensity-volume histogram-based, morphological features, local intensity, and texture matrix-based features are treated here. All texture matrices are rotationally and translationally invariant. Illumination invariance of texture matrices may be achieved by particular discretisation schemes, e.g. *histogram matching*. None of the texture matrices are scale invariant, a property which can be useful in many (biomedical) applications for scale optimization. What the presented texture matrices lack, however, is directionality in combination with rotation invariance. These may be achieved by local binary patterns and steerable filters, which however fall beyond the scope of the current work. For these and other texture features, see Depeursinge et al. (2014).

Features are calculated on the base image, as well as transformed images (e.g. images transformed using wavelet or Gabor filters). To calculate features, it is assumed that an image segmentation mask exists, which identifies the voxels located within a region of interest (ROI). The ROI itself consists of two masks, an intensity mask and a morphological mask. These masks may be identical, but not necessarily so, as described in Section 3.5.

Different feature families require additional image processing steps before feature calculation. Several feature families require prior discretisation of grey levels into grey level bins, notably intensity histogram and texture feature families. Other feature families do not require discretisation before calculations. For more details on image processing, see figure 3.1 in the previous chapter.

Below is an overview table summarising some image processing requirements of the different feature families.

Feature family	count	ROI mask		
		morph.	int.	discr.
morphology	29	×	×	
local intensity	2		×	
intensity-based statistics	18		×	
intensity histogram	23		×	×
intensity-volume histogram	5		×	(×)
grey level co-occurrence matrix	25		×	×
grey level run length matrix	16		×	×
grey level size zone matrix	16		×	×
grey level distance zone matrix	16	×	×	×
neighbourhood grey tone difference matrix	5		×	×
neighbouring grey level dependence matrix	17		×	×

Table 4.1: Feature families and required image processing. For each feature family, the number of features in the document, the required input of a morphological (morph.) and/or intensity (int.) ROI mask, as well as the requirement of image discretisation (discr.) is provided. Note that the image discretisation of intensity-volume histogram features is performed differently as compared to other feature families.

4.1 Morphological features

Morphological features describe geometric aspects of a region of interest (ROI), such as area and volume. Morphological features are based on ROI voxel representations of the volume. Three voxel representations of the volume are conceivable. First, the volume can be represented by a collection of voxels with each voxel taking up a certain volume. Second, the voxel point set X_c consisting of coordinates of the voxel centers may be used. Third, the volume is represented as an outer surface mesh. We use the second representation when the inner structure of the volume is important, and the third representation when only the outer surface structure is important. The first representation is not used because it does not handle partial volume effects at the ROI edge well, and also to avoid inconsistencies in feature values introduced by mixing representations in small voxel volumes.

Mesh-based representation. A mesh-based representation of the outer surface allows consistent evaluation of the surface volume and area independent of size. Voxel-based representations lead to partial volume effects and over-estimation of surface area. The surface of the ROI volume is translated into a triangle mesh using a meshing algorithm. While multiple meshing algorithms exist, we suggest the use of the *Marching Cubes* algorithm (Lorenson and Cline, 1987; Lewiner et al., 2003) because of its widespread availability in different programming languages and reasonable approximation of the surface area and volume (Stelllinger et al., 2007). In practice, mesh-derived feature values depend upon the meshing algorithm used and small differences may occur.

Meshing algorithms use the ROI voxel point set X_c to create a closed mesh. Dependent on the algorithm, a parameter is required to specify where the mesh should be drawn. A default level of 0.5 times the voxel spacing is used for marching cube algorithms. Alternatively a value of 0.5 can be used for isosurface algorithms, when the ROI mask consists

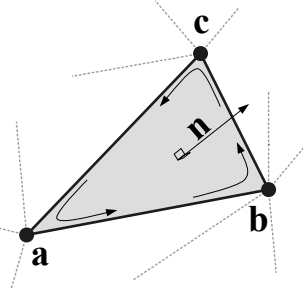


Figure 4.1: Meshing algorithms draw faces and vertices to cover the ROI. One face, spanned by vertices a , b and c , is highlighted. Moreover, the vertices define the three edges $ab = b - a$, $bc = c - b$ and $ca = a - c$. The face normal n is determined using the right-hand rule, and calculated as $n = (ab \times bc) / \|ab \times bc\|$, i.e. the outer product of edge ab with edge bc , normalised by its length.

of 0 and 1 values. Depending on implementation, isosurface algorithms may also require padding of the ROI mask with non-ROI voxels to correctly estimate the isosurface contours in places where ROI voxels would otherwise be located at the edge of the mask.

The closed mesh drawn by the meshing algorithm consists of N_{fc} triangle faces spanned by N_{vx} vertex points. An example triangle face is drawn in Figure 4.1. The set of vertex points is then X_{vx} .

The calculation of the mesh volume requires that all faces have the same orientation of the face normal. Consistent orientation can be checked by the fact that in a regular, closed mesh, all edges are shared between exactly two faces. Given the edge spanned by vertices a and b , the edge must be $ab = b - a$ for one face and $ba = a - b$ for the adjacent face. This ensures consistent application of the right-hand rule, and thus consistent orientation of the face normals. Algorithm implementations may return consistently orientated faces by default.

ROI morphological and intensity masks. The ROI consists of a morphological and an intensity mask. The morphological mask is used to calculate many of the morphological features and to generate the voxel point set X_c . Any holes within the morphological map are understood to be the result of segmentation decisions, and thus to be intentional. The intensity mask is used to generate the voxel intensity set X_{gl} with corresponding point set $X_{c,gl}$. In the benchmark data sets (Chapter 7), the masks are identical for the digital phantom, but differ due to re-segmentation of the intensity mask.

4.1.1 Volume

The *volume* V is calculated from the ROI mesh as follows (Zhang and Chen, 2001). A tetrahedron is formed by each face k and the origin. By placing the origin vertex of each tetrahedron at $(0, 0, 0)$, the signed volume of the tetrahedron is:

$$V_k = \frac{\mathbf{a} \cdot (\mathbf{b} \times \mathbf{c})}{6}$$

Here a , b and c are the vertex points of face k . Depending on the orientation of the normal, the signed volume may be positive or negative. Hence, the orientation of face normals

should be consistent, e.g. all normals must be either pointing outward or inward. The *volume* V is then calculated by summing over the face volumes, and taking the absolute value:

$$V = \left| \sum_{k=1}^{N_{fc}} V_k \right|$$

For positron emission tomography, *volume* is equivalent to the *metabolically active tumour volume* (MATV).

4.1.2 Approximate volume

In clinical practice, volumes are commonly determined by counting voxels. For volumes consisting of a large number of voxels (1000s), the differences between *approximate volume* and mesh-based *volume* are usually negligible. However for volumes with a low number of voxels (10s to 100s), *approximate volume* will overestimate volume compared to mesh-based *volume*. It is therefore only used as a reference feature, and not in the calculation of other morphological features.

Approximate volume is defined as:

$$F_{morph.approx.vol} = \sum_{k=1}^{N_v} V_k$$

Here N_v is the number of voxels in the morphological mask of the ROI, and V_k the volume of voxel k .

4.1.3 Surface area

The *surface area* A is also calculated from the ROI mesh by summing over the triangular face surface areas (Aerts et al., 2014). By definition, the area of face k is:

$$A_k = \frac{|\mathbf{ab} \times \mathbf{ac}|}{2}$$

As in Figure 4.1, edge $\mathbf{ab} = \mathbf{b} - \mathbf{a}$ is the vector from vertex \mathbf{a} to vertex \mathbf{b} , and edge $\mathbf{ac} = \mathbf{c} - \mathbf{a}$ the vector from vertex \mathbf{a} to vertex \mathbf{c} . The total *surface area* A is then:

$$A = \sum_{k=1}^{N_{fc}} A_k$$

4.1.4 Surface to volume ratio

The *surface to volume ratio* is given as (Aerts et al., 2014):

$$F_{morph.av} = \frac{A}{V}$$

4.1.5 Compactness 1

Several features (4.1.5-4.1.9) quantify the deviation of the ROI volume from a representative spheroid. All these definitions can be derived from one another. As a result these features are highly correlated and may thus be redundant. *Compactness 1* (Aerts et al., 2014) is a measure for how compact, or sphere-like the volume is. It is defined as:

$$F_{morph.comp.1} = \frac{V}{\pi^{1/2} A^{3/2}}$$

Some definitions use $A^{2/3}$ instead of $A^{3/2}$, e.g. (Aerts et al., 2014), but this is not dimensionless.

4.1.6 Compactness 2

Compactness 2 (Aerts et al., 2014) also quantifies how sphere-like the volume is:

$$F_{morph.comp.2} = 36\pi \frac{V^2}{A^3}$$

By definition $F_{morph.comp.1} = 1/6\pi (F_{morph.comp.2})^{1/2}$.

4.1.7 Spherical disproportion

Spherical disproportion (Aerts et al., 2014) likewise describes how sphere-like the volume is:

$$F_{morph.sph.dispr} = \frac{A}{4\pi R^2} = \frac{A}{(36\pi V^2)^{1/3}}$$

By definition $F_{morph.sph.dispr} = (F_{morph.comp.2})^{-1/3}$.

4.1.8 Sphericity

Sphericity (Aerts et al., 2014) is a further measure to describe how sphere-like the volume is:

$$F_{morph.sphericity} = \frac{(36\pi V^2)^{1/3}}{A}$$

By definition $F_{morph.sphericity} = (F_{morph.comp.2})^{1/3}$.

4.1.9 Asphericity

Asphericity (Apostolova et al., 2014) also describes how much the ROI deviates from a perfect sphere, with perfectly spherical volumes having an asphericity of 0. Asphericity is defined as:

$$F_{morph.asphericity} = \left(\frac{1}{36\pi} \frac{A^3}{V^2} \right)^{1/3} - 1$$

By definition $F_{morph.asphericity} = (F_{morph.comp.2})^{-1/3} - 1$

4.1.10 Centre of mass shift

The distance between the ROI volume centroid and the intensity-weighted ROI volume is an abstraction of the spatial distribution of low/high intensity regions within the ROI. Let $N_{v,m}$ be the number of voxels in the morphological mask. The ROI volume centre of mass is calculated from the morphological voxel point set \mathbf{X}_c as follows:

$$\overrightarrow{CoM}_{geom} = \frac{1}{N_{v,m}} \sum_{k=1}^{N_{v,m}} \vec{X}_{c,k}$$

The intensity-weighted ROI volume is based on the intensity mask. The position of each voxel centre in the intensity mask voxel set $\mathbf{X}_{c,gl}$ is weighted by its corresponding intensity \mathbf{X}_{gl} . Therefore, with $N_{v,gl}$ the number of voxels in the intensity mask:

$$\overrightarrow{CoM}_{gl} = \frac{\sum_{k=1}^{N_{v,gl}} X_{gl,k} \vec{X}_{c,gl,k}}{\sum_{k=1}^{N_{v,gl}} X_{gl,k}}$$

The distance between the two centres of mass is then:

$$F_{morph.com} = \|\overrightarrow{CoM}_{geom} - \overrightarrow{CoM}_{gl}\|_2$$

4.1.11 Maximum 3D diameter

The *maximum 3D diameter* (Aerts et al., 2014) is the distance between the two most distant vertices in the ROI mesh vertex set \mathbf{X}_{vx} :

$$F_{morph.diam} = \max \left(\|\vec{X}_{vx,k_1} - \vec{X}_{vx,k_2}\|_2 \right), \quad k_1 = 1, \dots, N \quad k_2 = 1, \dots, N$$

A practical way of determining the *maximum 3D diameter* is to first construct the convex hull of the ROI mesh. The convex hull vertex set $\mathbf{X}_{vx,convex}$ is guaranteed to contain the two most distant vertices of \mathbf{X}_{vx} . This significantly reduces the computational cost of calculating distances between all vertices. Despite the remaining $O(n^2)$ cost of calculating distances between different vertices, $\mathbf{X}_{vx,convex}$ is usually considerably smaller in size than \mathbf{X}_{vx} . Moreover, the convex hull is later used for the calculation of other morphological features (4.1.25-4.1.26).

4.1.12 Major axis length

Principal component analysis (PCA) can be used to determine the main orientation of the ROI (Solomon and Breckon, 2011). On a three dimensional object, PCA yields three orthogonal eigenvectors $\{e_1, e_2, e_3\}$ and three eigenvalues $(\lambda_1, \lambda_2, \lambda_3)$. These eigenvalues and eigenvectors geometrically describe a triaxial ellipsoid. The three eigenvectors determine the orientation of the ellipsoid, whereas the eigenvalues provide a measure of how far the ellipsoid extends along each eigenvector. Several features (4.1.12-4.1.16, 4.1.21-4.1.22) make use of principal component analysis.

The eigenvalues can be ordered so that $\lambda_{major} \geq \lambda_{minor} \geq \lambda_{least}$ correspond to the major, minor and least axes of the ellipsoid respectively. The semi-axes lengths a , b and c for the major, minor and least axes are then $2\sqrt{\lambda_{major}}$, $2\sqrt{\lambda_{minor}}$ and $2\sqrt{\lambda_{least}}$ respectively. The *major axis length* is twice the semi-axis length a , determined using the largest eigenvalue obtained by PCA on the point set of voxel centers \mathbf{X}_c (Heiberger and Holland, 2015):

$$F_{morph.pca.major} = 2a = 4\sqrt{\lambda_{major}}$$

4.1.13 Minor axis length

The *minor axis length* of the ROI provides a measure of how far the volume extends along the second largest axis. The *minor axis length* is twice the semi-axis length b , determined using the second largest eigenvalue obtained by PCA, as described in Section 4.1.12:

$$F_{morph.pca.minor} = 2b = 4\sqrt{\lambda_{minor}}$$

4.1.14 Least axis length

The least axis is the axis along which the object is least extended. The *least axis length* is twice the semi-axis length c , determined using the smallest eigenvalue obtained by PCA, as described in Section 4.1.12:

$$F_{morph.pca.least} = 2c = 4\sqrt{\lambda_{least}}$$

4.1.15 Elongation

The ratio of the major and minor principal axis lengths could be viewed as the extent to which a volume is longer than it is wide, i.e. is eccentric. For computational reasons, we express *elongation* as an inverse ratio. 1 is thus completely non-elongated, e.g. a sphere, and smaller values express greater elongation of the ROI volume.

$$F_{morph.pca.elongation} = \sqrt{\frac{\lambda_{minor}}{\lambda_{major}}}$$

4.1.16 Flatness

The ratio of the major and least axis lengths could be viewed as the extent to which a volume is flat relative to its length. For computational reasons, we express *flatness* as an inverse ratio. 1 is thus completely non-flat, e.g. a sphere, and smaller values express objects which are increasingly flatter.

$$F_{morph.pca.flatness} = \sqrt{\frac{\lambda_{least}}{\lambda_{major}}}$$

4.1.17 Volume density - axis-aligned bounding box

Volume density is the fraction of the ROI volume and a comparison volume. Here the comparison volume is that of the axis-aligned bounding box (AABB) of the ROI mesh vertex set X_{vx} or the ROI mesh convex hull vertex set $X_{vx,convex}$. Both vertex sets generate an identical bounding box, which is the smallest box enclosing the vertex set, and aligned with the axes of the reference frame. Thus:

$$F_{morph.v.dens.aabb} = \frac{V}{V_{aabb}}$$

This feature is also called *extent* (El Naqa et al., 2009; Solomon and Breckon, 2011).

4.1.18 Area density - axis-aligned bounding box

Conceptually similar to the *volume density - axis-aligned bounding box* feature, *area density* considers the ratio of the ROI surface area and the surface area A_{aabb} of the axis-aligned bounding box enclosing the ROI mesh vertex set \mathbf{X}_{vx} (van Dijk et al., 2017). The bounding box is identical to the one used in the *volume density - axis-aligned bounding box* feature. Thus:

$$F_{morph.a.dens.aabb} = \frac{A}{A_{aabb}}$$

4.1.19 Volume density - oriented minimum bounding box

The volume of an axis-aligned bounding box is generally not the smallest obtainable volume enclosing the ROI. By orienting the box along a different set of axes, a smaller enclosing volume may be attainable. The oriented minimum bounding box of the ROI mesh vertex set \mathbf{X}_{vx} or $\mathbf{X}_{vx,convex}$ encloses the vertex set and has the smallest possible volume. A 3D rotating callipers technique was devised by O'Rourke (1985) to derive the oriented minimum bounding box. Due to computational complexity of the rotating callipers technique, the oriented minimum bounding box is commonly approximated at lower complexity, see e.g. Barequet and Har-Peled (2001) and Chan and Tan (2001). Thus:

$$F_{morph.v.dens.ombb} = \frac{V}{V_{ombb}}$$

Here V_{ombb} is the volume of the oriented minimum bounding box.

4.1.20 Area density - oriented minimum bounding box

The *area density* is estimated as:

$$F_{morph.a.dens.ombb} = \frac{A}{A_{ombb}}$$

Here A_{ombb} is the surface area of the same bounding box as calculated for the *volume density - oriented minimum bounding box* feature.

4.1.21 Volume density - approximate enclosing ellipsoid

The eigenvectors and eigenvalues from PCA of the ROI voxel center point set \mathbf{X}_c can be used to describe an ellipsoid approximating the point cloud (Mazurowski et al., 2016). The volume of an ellipsoid is $V_{aee} = 4\pi abc/3$, with a , b , and c being the lengths of the ellipsoid's semi-principal axes, see Section 4.1.12. The *volume density* is then:

$$F_{morph.v.dens.aee} = \frac{3V}{4\pi abc}$$

4.1.22 Area density - approximate enclosing ellipsoid

The surface area of an ellipsoid can generally not be evaluated in an elementary form. However, it is possible to approximate the surface using an infinite series. We use the same

semi-principal axes as for the *volume density - approximate ellipsoid* feature and define:

$$A_{aee}(a, b, c) = 4\pi ab \sum_{\nu=0}^{\infty} \frac{(\alpha\beta)^\nu}{1-4\nu^2} P_\nu \left(\frac{\alpha^2 + \beta^2}{2\alpha\beta} \right)$$

Here $\alpha = \sqrt{1-b^2/a^2}$ and $\beta = \sqrt{1-c^2/a^2}$ are eccentricities of the ellipsoid and P_ν is the Legendre polynomial function for degree ν . Though infinite, the series converges, and calculation may be stopped early. Gains in precision past $\nu = 20$ are limited, and as a default we stop calculations at this polynomial degree.

The *area density* is then approximated as:

$$F_{morph.a.dens.aee} = \frac{A}{A_{aee}}$$

4.1.23 Volume density - minimum volume enclosing ellipsoid

The approximate ellipsoid may not enclose the ROI or be the smallest enclosing ellipsoid. The minimum volume enclosing ellipsoid is generally approximated to make calculation more feasible. Various algorithms have been described, e.g. (Todd and Yldrm, 2007; Ahipaaolu, 2015), which are usually elaborations on Khachiyan's barycentric coordinate descent method (Khachiyan, 1996).

The minimum volume enclosing ellipsoid (MVEE) encloses the ROI mesh vertex set \mathbf{X}_{vx} , and by definition $\mathbf{X}_{vx,convex}$ as well. Use of the convex mesh set $\mathbf{X}_{vx,convex}$ is recommended due to its sparsity compared to the full vertex set. The volume of the MVEE is defined by its semi-axes lengths $V_{mvee} = 4\pi abc/3$. Then:

$$F_{morph.v.dens.mvee} = \frac{V}{V_{mvee}}$$

For Khachiyan's barycentric coordinate descent-based methods we use a default tolerance $\tau = 0.001$ as stopping criterion.

4.1.24 Area density - minimum volume enclosing ellipsoid

The surface area of an ellipsoid does not have a general elementary form, but should be approximated as noted in Section 4.1.22. Let the approximated surface area of the MVEE be A_{mvee} . Then:

$$F_{morph.a.dens.mvee} = \frac{A}{A_{mvee}}$$

4.1.25 Volume density - convex hull

The convex hull encloses ROI mesh vertex set \mathbf{X}_{vx} and consists of the vertex set $\mathbf{X}_{vx,convex}$ and corresponding faces, see Section 4.1.11. The volume of the ROI mesh convex hull set V_{convex} is calculated as for the *volume* feature (4.1.1). The *volume density* can then be calculated as follows:

$$F_{morph.v.dens.conv.hull} = \frac{V}{V_{convex}}$$

This feature is also called *solidity* (El Naqa et al., 2009; Solomon and Breckon, 2011).

4.1.26 Area density - convex hull

The area of the convex hull A_{convex} is the sum of the areas of the faces of the convex hull, as in the calculation of the *area* feature (4.1.3). The convex hull is identical to the one used in the *volume density - convex hull* feature. Then:

$$F_{morph.a.dens.conv.hull} = \frac{A}{A_{convex}}$$

4.1.27 Integrated intensity

Integrated intensity is the average grey level multiplied by the volume. In the context of ^{18}F -FDG-PET, this feature is called *total legion glycolysis* (Vaidya et al., 2012). Thus:

$$F_{morph.integ.int} = V \frac{1}{N_{v,gl}} \sum_{k=1}^{N_{v,gl}} X_{gl,k}$$

$N_{v,gl}$ is the number of voxels in the intensity mask.

4.1.28 Moran's I index

Moran's I index is an indicator of spatial autocorrelation (Moran, 1950; Dale et al., 2002). It is defined as:

$$F_{morph.moran.i} = \frac{N_{v,gl}}{\sum_{k_1=1}^{N_{v,gl}} \sum_{k_2=1}^{N_{v,gl}} w_{k_1 k_2}} \frac{\sum_{k_1=1}^{N_{v,gl}} \sum_{k_2=1}^{N_{v,gl}} w_{k_1 k_2} (X_{gl,k_1} - \mu) (X_{gl,k_2} - \mu)}{\sum_{k=1}^{N_{v,gl}} (X_{gl,k} - \mu)^2}, \quad k_1 \neq k_2$$

As before $N_{v,gl}$ is the number of voxels in the ROI intensity mask, μ is the mean of \mathbf{X}_{gl} and $w_{k_1 k_2}$ is a weight factor, equal to the inverse Euclidean distance between voxels k_1 and k_2 of the point set $\mathbf{X}_{c,gl}$ of the ROI intensity mask (Da Silva et al., 2008). Values of Moran's I close to 1.0, 0.0 and -1.0 indicate high spatial autocorrelation, no spatial autocorrelation and high spatial anti-autocorrelation, respectively. Note that for a ROI containing many voxels, calculating Moran's I index may be computationally expensive due to $O(n^2)$ behaviour. Approximation by repeated subsampling of the ROI may be required to make the calculation tractable, at the cost of accuracy.

4.1.29 Geary's C measure

Geary's C measure assesses spatial autocorrelation, similar to Moran's I index (Geary, 1954; Dale et al., 2002). In contrast to Moran's I index, Geary's C measure directly assesses grey level differences between voxels and is more sensitive to local spatial autocorrelation. This measure is defined as:

$$F_{morph.geary.c} = \frac{N_{v,gl} - 1}{2 \sum_{k_1=1}^{N_{v,gl}} \sum_{k_2=1}^{N_{v,gl}} w_{k_1 k_2}} \frac{\sum_{k_1=1}^{N_{v,gl}} \sum_{k_2=1}^{N_{v,gl}} w_{k_1 k_2} (X_{gl,k_1} - X_{gl,k_2})^2}{\sum_{k=1}^{N_{v,gl}} (X_{gl,k} - \mu)^2}, \quad k_1 \neq k_2$$

As with Moran's I , $N_{v,gl}$ is the number of voxels in the ROI intensity mask, μ is the mean of \mathbf{X}_{gl} and $w_{k_1 k_2}$ is a weight factor, equal to the inverse Euclidean distance between voxels k_1 and k_2 of the ROI voxel point set $\mathbf{X}_{c,gl}$ (Da Silva et al., 2008). Just Moran's I , Geary's C measure exhibits $O(n^2)$ behaviour and an approximation scheme may be required to make calculation feasible for large ROIs.

4.2 Local intensity features

Voxel intensities within a defined neighbourhood around a center voxel are considered for local intensity features. Unlike many feature sets, local features do not draw solely on intensities within the ROI. While only voxels within the ROI intensity map are used as a center voxel, the corresponding local neighbourhood draws upon all voxels regardless of being in a ROI.

4.2.1 Local intensity peak

The local intensity peak was originally devised for reducing variance in determining standardised uptake values (Wahl et al., 2009). It is defined as the mean grey level in a 1 cm^3 spherical volume, centered on the voxel with the maximum grey level in the ROI intensity mask.

To calculate $F_{loc.peak.local}$, we first select all the voxels with centers within radius $r = \left(\frac{3}{4\pi}\right)^{1/3} \approx 0.62 \text{ cm}$ of the voxel containing the maximum grey level. Subsequently, the mean grey level of the selected voxels, including the center voxel, are calculated.

In case the maximum grey level is found in multiple ROI voxels, *local intensity peak* is calculated for each of these voxels, and the highest local intensity peak is chosen.

4.2.2 Global intensity peak

The *global intensity peak* feature $F_{loc.peak.global}$ is similar to the *local intensity peak* (Frings et al., 2014). However, instead of calculating the mean intensity for the voxel(s) with the maximum grey level, the mean intensity is calculated within a neighbourhood for every voxel in the ROI intensity mask. The highest intensity peak value is then selected. Calculation of the *global intensity peak* feature may be accelerated by construction and application of an appropriate spatial spherical mean convolution filter, due to the convolution theorem.

4.3 Intensity-based statistical features

The intensity-based statistical features describe how grey levels within the region of interest (ROI) are distributed. The features in this set do not require discretisation, and may be used to describe a continuous intensity distribution. Intensity-based statistical features are not meaningful if the intensity scale is arbitrary.

Let $\mathbf{X}_{gl} = \{X_{gl,1}, X_{gl,2}, \dots, X_{gl,N_v}\}$ be the set of grey levels of the N_v voxels included in the ROI intensity mask.

4.3.1 Mean

The *mean* grey level of \mathbf{X}_{gl} is calculated as:

$$F_{stat.mean} = \frac{1}{N_v} \sum_{k=1}^{N_v} X_{gl,k}$$

4.3.2 Variance

The grey level *variance* of \mathbf{X}_{gl} is defined as:

$$F_{stat.var} = \frac{1}{N_v} \sum_{k=1}^{N_v} (X_{gl,k} - \mu)^2$$

4.3.3 Skewness

The *skewness* of the grey level distribution of \mathbf{X}_{gl} is defined as:

$$F_{stat.skew} = \frac{\frac{1}{N_v} \sum_{k=1}^{N_v} (X_{gl,k} - \mu)^3}{\left(\frac{1}{N_v} \sum_{k=1}^{N_v} (X_{gl,k} - \mu)^2 \right)^{3/2}}$$

Here $\mu = F_{stat.mean}$. If the grey level *variance* $F_{stat.var} = 0$, $F_{stat.skew} = 0$.

4.3.4 Kurtosis

Kurtosis, or technically excess kurtosis, is a measure of peakedness in the grey level distribution \mathbf{X}_{gl} :

$$F_{stat.kurt} = \frac{\frac{1}{N_v} \sum_{k=1}^{N_v} (X_{gl,k} - \mu)^4}{\left(\frac{1}{N_v} \sum_{k=1}^{N_v} (X_{gl,k} - \mu)^2 \right)^2} - 3$$

Here $\mu = F_{stat.mean}$. Note that kurtosis is corrected by a Fisher correction of -3 to center it on 0 for normal distributions. If the grey level *variance* $F_{stat.var} = 0$, $F_{stat.kurt} = 0$.

4.3.5 Median

The *median* $F_{stat.median}$ is the sample median of \mathbf{X}_{gl} .

4.3.6 Minimum grey level

The *minimum grey level* is equal to the lowest grey level present in \mathbf{X}_{gl} .

4.3.7 10th percentile

P_{10} is the 10th percentile of \mathbf{X}_{gl} . P_{10} is more robust to grey level outliers than the *minimum grey level*.

4.3.8 90th percentile

P_{90} is the 90th percentile of \mathbf{X}_{gl} . P_{90} is more robust to grey level outliers than the *maximum grey level*.

4.3.9 Maximum grey level

The *maximum grey level* is equal to the highest grey level present in \mathbf{X}_{gl} .

4.3.10 Interquartile range

The *interquartile range* (IQR) of \mathbf{X}_{gl} is defined as:

$$F_{stat.iqr} = P_{75} - P_{25}$$

P_{25} and P_{75} are the 25th and 75th percentiles of \mathbf{X}_{gl} , respectively.

4.3.11 Range

The *range* of grey levels is defined as:

$$F_{stat.range} = \max(\mathbf{X}_{gl}) - \min(\mathbf{X}_{gl})$$

4.3.12 Mean absolute deviation

Mean absolute deviation is a measure of dispersion from the mean of \mathbf{X}_{gl} :

$$F_{stat.mad} = \frac{1}{N_v} \sum_{k=1}^{N_v} |X_{gl,k} - \mu|$$

Here $\mu = F_{stat.mean}$.

4.3.13 Robust mean absolute deviation

The *mean absolute deviation* feature may be influenced by outliers. To increase robustness, the set of grey levels can be restricted to those which lie closer to the center of the distribution. Let

$$\mathbf{X}_{gl,10-90} = \{x \in \mathbf{X}_{gl} | P_{10}(\mathbf{X}_{gl}) \leq x \leq P_{90}(\mathbf{X}_{gl})\}$$

Thus $\mathbf{X}_{gl,10-90}$ is the set of $N_{v,10-90} \leq N_v$ voxels in \mathbf{X}_{gl} whose grey levels are equal to, or lie between, the values corresponding to the 10th and 90th percentiles of \mathbf{X}_{gl} . The robust mean absolute deviation is then:

$$F_{stat.rmad} = \frac{1}{N_{v,10-90}} \sum_{k=1}^{N_{v,10-90}} |X_{gl,10-90,k} - \bar{X}_{gl,10-90}|$$

$\bar{X}_{gl,10-90}$ denotes the sample mean of $\mathbf{X}_{gl,10-90}$.

4.3.14 Median absolute deviation

Median absolute deviation is similar in concept to *mean absolute deviation*, but measures dispersion from the median instead of mean. Thus

$$F_{stat.medad} = \frac{1}{N_v} \sum_{k=1}^{N_v} |X_{gl,k} - M|$$

Here, median $M = F_{stat.median}$.

4.3.15 Coefficient of variation

The *coefficient of variation* measures the dispersion of the X_{gl} distribution. It is defined as

$$F_{stat.cov} = \frac{\sigma}{\mu}$$

Here $\sigma = F_{stat.var}^{1/2}$ and $\mu = F_{stat.mean}$ are the standard deviation and mean of the grey level distribution, respectively.

4.3.16 Quartile coefficient of dispersion

The *quartile coefficient of dispersion* is a robust alternative to *coefficient of variance*. It is defined as

$$F_{stat.qcod} = \frac{P_{75} - P_{25}}{P_{75} + P_{25}}$$

P_{25} and P_{75} are the 25th and 75th percentile of X_{gl} , respectively.

4.3.17 Energy

Energy (Aerts et al., 2014) of X_{gl} is defined as:

$$F_{stat.energy} = \sum_{k=1}^{N_v} X_{gl,k}^2$$

4.3.18 Root mean square

The *root mean square* feature (Aerts et al., 2014), also called the quadratic mean, of X_{gl} is defined as:

$$F_{stat.rms} = \sqrt{\frac{\sum_{k=1}^{N_v} X_{gl,k}^2}{N_v}}$$

4.4 Intensity histogram features

An intensity histogram is generated by discretising the original set of grey levels X_{gl} into grey level bins. Approaches to discretisation are described in Section 3.7.

Let $\mathbf{X}_d = \{X_{d,1}, X_{d,2}, \dots, X_{d,N_v}\}$ be the set of N_g discretised grey levels of the N_v voxels in the ROI intensity mask. Let $\mathbf{H} = \{n_1, n_2, \dots, n_{N_g}\}$ be the histogram with frequency count n_i of each discretised grey level i in \mathbf{X}_d . The occurrence probability p_i for each grey level bin i is then approximated as $p_i = n_i/N_v$.

4.4.1 Intensity histogram mean

The *mean* (Aerts et al., 2014) of \mathbf{X}_d is calculated as:

$$F_{ih.mean} = \frac{1}{N_v} \sum_{k=1}^{N_v} X_{d,k}$$

An equivalent formulation is:

$$F_{ih.mean} = \sum_{i=1}^{N_g} i p_i$$

4.4.2 Intensity histogram variance

The *variance* (Aerts et al., 2014) of \mathbf{X}_d is defined as:

$$F_{ih.var} = \frac{1}{N_v} \sum_{k=1}^{N_v} (X_{d,k} - \mu)^2$$

Here $\mu = F_{ih.mean}$. This formulation is equivalent to:

$$F_{ih.var} = \sum_{i=1}^{N_g} (i - \mu)^2 p_i$$

4.4.3 Intensity histogram skewness

The *skewness* (Aerts et al., 2014) of \mathbf{X}_d is defined as:

$$F_{ih.skew} = \frac{\frac{1}{N_v} \sum_{k=1}^{N_v} (X_{d,k} - \mu)^3}{\left(\frac{1}{N_v} \sum_{k=1}^{N_v} (X_{d,k} - \mu)^2 \right)^{3/2}}$$

Here $\mu = F_{ih.mean}$. This formulation is equivalent to:

$$F_{ih.skew} = \frac{\sum_{i=1}^{N_g} (i - \mu)^3 p_i}{\left(\sum_{i=1}^{N_g} (i - \mu)^2 p_i \right)^{3/2}}$$

If the discretised grey level variance $F_{ih.var} = 0$, $F_{ih.skew} = 0$.

4.4.4 Intensity histogram kurtosis

Kurtosis (Aerts et al., 2014), or technically excess kurtosis, is calculated as measure of peakedness of the distribution \mathbf{X}_d :

$$F_{ih.kurt} = \frac{\frac{1}{N_v} \sum_{k=1}^{N_v} (X_{d,k} - \mu)^4}{\left(\frac{1}{N_v} \sum_{k=1}^{N_v} (X_{d,k} - \mu)^2 \right)^2} - 3$$

Here $\mu = F_{ih.mean}$. The alternative, but equivalent, formulation is:

$$F_{ih.kurt} = \frac{\sum_{i=1}^{N_g} (i - \mu)^4 p_i}{\left(\sum_{i=1}^{N_g} (i - \mu)^2 p_i \right)^2} - 3$$

Note that kurtosis is corrected by a Fisher correction of -3 to center kurtosis on 0 for normal distributions. If the discretised grey level $F_{ih.var} = 0$, $F_{ih.kurt} = 0$.

4.4.5 Intensity histogram median

The *median* $F_{ih.median}$ is the sample median of X_d (Aerts et al., 2014).

4.4.6 Intensity histogram minimum grey level

The *minimum grey level* (Aerts et al., 2014) is equal to the lowest discretised grey level present in X_d . For *fixed bin number* discretisation $F_{ih.min} = 1$ by definition, but it may deviate for *fixed bin size* discretisation.

4.4.7 Intensity histogram 10th percentile

P_{10} is the 10th percentile of X_d .

4.4.8 Intensity histogram 90th percentile

P_{90} is the 90th percentile of X_d .

4.4.9 Intensity histogram maximum grey level

The *maximum grey level* (Aerts et al., 2014) is equal to the highest discretised grey level present in X_d . $F_{ih.max} = N_g$ by definition.

4.4.10 Intensity histogram mode

The *mode* of X_d is the most common discretised grey level present, i.e. i for which count n_i is maximal. The mode may not be uniquely defined. When multiple bins contain the highest grey level count, the bin closest to the histogram mean is chosen as $F_{ih.mode}$. In pathological cases with two such bins equidistant to the mean, the bin to the left of the mean is selected.

4.4.11 Intensity histogram interquartile range

The *interquartile range* (IQR) of X_d is defined as:

$$F_{ih.iqr} = P_{75} - P_{25}$$

P_{25} and P_{75} are the 25th and 75th percentile of X_d , respectively. The interquartile range of X_d is always an integer.

4.4.12 Intensity histogram range

The *range* of grey levels (Aerts et al., 2014) in the histogram is defined as:

$$F_{ih.range} = \max(X_d) - \min(X_d)$$

The *intensity histogram range* is therefore equal to the width of the histogram. For *fixed bin number* discretisation $F_{ih.range} = N_g$ by definition.

4.4.13 Intensity histogram mean absolute deviation

The *mean absolute deviation* (Aerts et al., 2014) is a measure of dispersion from the mean of \mathbf{X}_d :

$$F_{ih.mad} = \frac{1}{N_v} \sum_{i=1}^{N_v} |X_{d,i} - \mu|$$

Here $\mu = F_{ih.mean}$.

4.4.14 Intensity histogram robust mean absolute deviation

Histogram mean absolute deviation may be influenced by outliers. To increase robustness, the set of discretised grey levels under consideration can be restricted to those which are closer to the center of the distribution. Let

$$\mathbf{X}_{d,10-90} = \{x \in \mathbf{X}_d | P_{10}(\mathbf{X}_d) \leq x \leq P_{90}(\mathbf{X}_d)\}$$

In short, $\mathbf{X}_{d,10-90}$ is the set of $N_{v,10-90} \leq N_v$ voxels in \mathbf{X}_d whose discretised grey levels are equal to, or lie between, the values corresponding to the 10th and 90th percentiles of \mathbf{X}_d . The robust mean absolute deviation is then:

$$F_{ih.rmad} = \frac{1}{N_{v,10-90}} \sum_{k=1}^{N_{v,10-90}} |X_{d,10-90,k} - \bar{X}_{d,10-90}|$$

$\bar{X}_{d,10-90}$ denotes the sample mean of $\mathbf{X}_{d,10-90}$.

4.4.15 Intensity histogram median absolute deviation

Histogram median absolute deviation is conceptually similar to *histogram mean absolute deviation*, but measures dispersion from the median instead of mean. Thus:

$$F_{ih.medmad} = \frac{1}{N_v} \sum_{k=1}^{N_v} |X_{d,k} - M|$$

Here, median $M = F_{ih.median}$.

4.4.16 Intensity histogram coefficient of variation

The *coefficient of variation* measures the dispersion of the histogram. It is defined as:

$$F_{ih.cov} = \frac{\sigma}{\mu}$$

Here $\sigma = F_{ih.var}^{1/2}$ and $\mu = F_{ih.mean}$ are the standard deviation and mean of the discretised grey level distribution, respectively.

4.4.17 Intensity histogram quartile coefficient of dispersion

The *quartile coefficient of dispersion* is a robust alternative to *coefficient of variance*. It is defined as:

$$F_{ih.qcod} = \frac{P_{75} - P_{25}}{P_{75} + P_{25}}$$

P_{25} and P_{75} are the 25th and 75th percentile of \mathbf{X}_d , respectively.

4.4.18 Intensity histogram entropy

Entropy (Aerts et al., 2014) is an information-theoretic concept that gives a metric for the information contained within \mathbf{X}_d . The particular metric used is Shannon entropy, which is defined as:

$$F_{ih.entropy} = - \sum_{i=1}^{N_g} p_i \log_2 p_i$$

4.4.19 Intensity histogram uniformity

Uniformity (Aerts et al., 2014) of \mathbf{X}_d is defined as:

$$F_{ih.uniformity} = \sum_{i=1}^{N_g} p_i^2$$

Note that this feature is also referred to as energy.

4.4.20 Maximum histogram gradient

The histogram gradient \mathbf{H}' can be calculated as:

$$H'_i = \begin{cases} H(2) - H(1) & i = 1 \\ (H(i+1) - H(i-1)) / 2 & 1 < i < N_g \\ H(N_g) - H(N_g - 1) & i = N_g \end{cases}$$

Histogram \mathbf{H} should be non-sparse, i.e. bins where $n_i = 0$ should not be omitted. Ostensibly, the histogram gradient can be calculated in different ways. The method above has the advantages of being easy to implement and leading to a gradient \mathbf{H}' with same size as \mathbf{H} . This helps avoid ambiguity concerning correspondence between the discretised grey level and the bin. The *maximum histogram gradient* (van Dijk et al., 2017) is:

$$F_{ih.max.grad} = \max(\mathbf{H}')$$

4.4.21 Maximum histogram gradient grey level

The *maximum histogram gradient grey level* (van Dijk et al., 2017) is the discretised grey level corresponding to the *maximum histogram gradient*, i.e. i for which \mathbf{H}' was maximal.

4.4.22 Minimum histogram gradient

The *minimum histogram gradient* (van Dijk et al., 2017) is:

$$F_{ih.min.grad} = \min(\mathbf{H}')$$

4.4.23 Minimum histogram gradient grey level

The *minimum histogram gradient grey level* (van Dijk et al., 2017) is the discretised grey level corresponding to the *minimum histogram gradient*, i.e. i for which \mathbf{H}' was minimal.

4.5 Intensity-volume histogram features

The (cumulative) intensity-volume histogram (IVH) of the voxel grey level set \mathbf{X}_{gl} of the ROI intensity mask describes the relationship between discretised grey level i and the fraction of the volume containing at least grey level i , ν (El Naqa et al., 2009). Dependent on the imaging modality, the calculation of IVH features requires discretising \mathbf{X}_{gl} to generate a discretised grey level voxel set $\mathbf{X}_{d,gl}$. Moreover, the total range G of discretised grey level values with discretisation interval w_d should be provided or determined. The total range determines the range of discretised grey level values to be included in the IVH, whereas the discretisation interval determines the difference between adjacent discretised grey levels in the IVH. For images with definite intensity units, the discretisation interval matches the bin width for discretisation. However, it differs for images with arbitrary intensity units. For consistency of IVH metric comparisons, it is recommended to use a range G as defined by the re-segmentation range whenever it is possible for imaging modalities with definite intensity units (both discrete and continuous cases).

Definite intensity units – discrete case. Some imaging modalities by default generate voxels with calibrated, discrete intensities, for example CT. In this case, the discretised ROI voxel set $\mathbf{X}_{d,gl} = \mathbf{X}_{gl}$ (i.e. no discretisation required). If a re-segmentation range is provided (see Section 3.5), the total range G is equal to the re-segmentation range. In the case of a half-open re-segmentation range, the upper limit of the range is $\max(\mathbf{X}_{gl})$. When no range is provided, $G = [\min(\mathbf{X}_{gl}), \max(\mathbf{X}_{gl})]$. The discretisation interval is $w_d = 1$.

Definite intensity units – continuous case. Imaging with calibrated, continuous intensities such as PET requires discretisation to determine the IVH, while preserving the quantitative intensity information. The use of a *fixed bin size* discretisation method is thus recommended, see Section 3.7. Proper use of this method requires to set the minimum grey level $X_{gl,min}$, the maximum grey level $X_{gl,max}$ and the bin width w_b prior to discretisation. If a re-segmentation range is defined (see Section 3.5), $X_{gl,min}$ is set to the lower bound of the re-segmentation range and $X_{gl,max}$ to the upper bound; otherwise $X_{gl,min} = \min(\mathbf{X}_{gl})$ and $X_{gl,max} = \max(\mathbf{X}_{gl})$ (i.e. the minimum and maximum grey levels in the imaging volume prior to discretisation). The bin width w_b is modality dependent, but should be small relative to the intensity range, e.g. 0.10 SUV for ^{18}F -FDG-PET.

Next, *fixed bin size* discretisation produces the voxel set \mathbf{X}_d of bin numbers, which needs to be converted to bin centers in order to maintain a direct relationship with the original intensities. We thus replace bin numbers \mathbf{X}_d with the intensity corresponding to the bin center:

$$\mathbf{X}_{d,gl} = X_{gl,min} + (\mathbf{X}_d - 0.5) w_b$$

i	γ	ν
1	0.0	1.000
2	0.2	0.324
3	0.4	0.324
4	0.6	0.311
5	0.8	0.095
6	1.0	0.095

Table 4.2: Example intensity-volume histogram evaluated at discrete grey levels i of the digital phantom. The total range $\mathbf{G} = [1, 6]$, with discretisation interval $w = 1$. Thus γ is the fractional grey level and ν is the corresponding volume fraction that contains grey level i or greater.

The total range is then $\mathbf{G} = [X_{gl,min} + 0.5w_b, X_{gl,max} - 0.5w_b]$. In this case, the discretisation interval matches the bin width, i.e. $w_d = w_b$.

Arbitrary intensity units. Some imaging modalities such as raw MRI data have arbitrary intensities. In such cases, a *fixed bin number* discretisation method with $N_g = 1000$ bins is recommended, see Section 3.7. The discretisation bin width is $w_b = (X_{gl,max} - X_{gl,min}) / N_g$, with $X_{gl,max} = \max(\mathbf{X}_{gl})$ and $X_{gl,min} = \min(\mathbf{X}_{gl})$, as re-segmentation ranges generally cannot be provided for non-calibrated intensities. The *fixed bin number* discretisation produces the voxel set $\mathbf{X}_d \in \{1, 2, \dots, N_g\}$. Because of the lack of calibration, $\mathbf{X}_{d,gl} = \mathbf{X}_d$, and consequentially the discretisation interval is $w_d = 1$ and the total range is $\mathbf{G} = [1, N_g]$

Calculating the IV histogram. We use $\mathbf{X}_{d,gl}$ to calculate fractional volumes and fractional grey levels.

As voxels for the same image stack generally all have the same dimensions, we may define fractional volume ν for discrete grey level i in the range \mathbf{G} with discretisation interval w_d as:

$$\nu_i = 1 - \frac{1}{N_v} \sum_{k=1}^{N_v} [X_{d,gl,k} < i]$$

Here $[..]$ is an Iverson bracket, yielding 1 if the condition is true and 0 otherwise. In essence, we count the voxels containing a discretised grey level smaller than i , divide by the total number of voxels, and then subtract this volume fraction to find ν_i .

The grey level fraction γ for discrete grey level i in the range \mathbf{G} with discretisation interval w_d is calculated as:

$$\gamma_i = \frac{i - \min(\mathbf{G})}{\max(\mathbf{G}) - \min(\mathbf{G})}$$

Note that we evaluate grey levels that may actually be absent in $\mathbf{X}_{d,gl}$. For the digital phantom of the benchmark data sets (Chapter 7) grey levels 2 and 5 are absent, but still evaluated to determine both the fractional volume and the grey level fraction. An example IVH for the digital phantom is shown in Table 4.2.

4.5.1 Volume at intensity fraction

The *volume at intensity fraction* V_x is the largest volume fraction ν that has an intensity fraction γ of at least $x\%$. This differs from conceptually similar dose-volume histograms used in radiotherapy planning, where V_{10} would indicate the volume fraction receiving at least 10 Gy planned dose. El Naqa et al. (2009) defined both V_{10} and V_{90} as features.

4.5.2 Intensity at volume fraction

The *intensity at volume fraction* I_x is the minimum discretised grey level i present in at most $x\%$ of the volume. El Naqa et al. (2009) defined both I_{10} and I_{90} as features.

4.5.3 Volume at intensity fraction difference

This feature is the difference between the volume fractions at two different intensity fractions, e.g. $V_{10} - V_{90}$ (El Naqa et al., 2009).

4.5.4 Intensity at volume fraction difference

This feature is the difference between discretised grey levels at two different fractional volumes, e.g. $I_{10} - I_{90}$ (El Naqa et al., 2009).

4.5.5 Area under IVH curve

The *area under the IVH curve* was defined by van Velden et al. (2011). The *area under the IVH curve* can be approximated by calculating the Riemann sum using the trapezoidal rule. Note that if there is only one grey level in the ROI, the *area under the IVH curve* $F_{ivh.auc} = 0$.

4.6 Texture features - Grey level co-occurrence based features

In image analysis, texture is one of the defining sets of features. Texture features were originally designed to assess surface texture in 2D images. Texture analysis is however not restricted to 2D slices, but can be extended to 3D objects. Image intensities are generally discretised before calculation of texture features, see Section 3.7.

The grey level co-occurrence matrix (GLCM) is a matrix that expresses how combinations of discretised grey levels of neighbouring pixels, or voxels in a 3D volume, are distributed along one of the image directions. Generally, the neighbourhood for GLCM is a 26-connected neighbourhood in 3D and a 8-connected neighbourhood in 2D. Thus, in 3D there are 13 unique direction vectors within the neighbourhood for distance $\delta = 1$, i.e. $(0, 0, 1)$, $(0, 1, 0)$, $(1, 0, 0)$, $(0, 1, 1)$, $(0, 1, -1)$, $(1, 0, 1)$, $(1, 0, -1)$, $(1, 1, 0)$, $(1, -1, 0)$, $(1, 1, 1)$, $(1, 1, -1)$, $(1, -1, 1)$ and $(1, -1, -1)$, whereas in 2D the corresponding direction vectors at distance 1 are $(1, 0, 0)$, $(1, 1, 0)$, $(0, 1, 0)$ and $(-1, 1, 0)$.

A GLCM is calculated for each direction vector, as follows. Let M_x be the $N_g \times N_g$ grey level co-occurrence matrix, with N_g the number of discretised grey levels present in the ROI intensity mask, and x the particular direction vector. Element (i, j) of the GLCM contains the frequency at which combinations of discretised grey levels i and j occur in neighbouring

voxels along direction $\mathbf{x}_+ = \mathbf{x}$ and along direction $\mathbf{x}_- = -\mathbf{x}$. Then, $\mathbf{M}_{\mathbf{x}} = \mathbf{M}_{\mathbf{x}_+} + \mathbf{M}_{\mathbf{x}_-} = \mathbf{M}_{\mathbf{x}_+} + \mathbf{M}_{\mathbf{x}_+}^T$ (Haralick et al., 1973). As a consequence the GLCM matrix $\mathbf{M}_{\mathbf{x}}$ is symmetric. An example of the calculation of a GLCM is shown in Table 4.3. Corresponding grey level co-occurrence matrices for each direction are shown in Table 4.4.

<table style="border-collapse: collapse; text-align: center;"> <tr><td>1</td><td>2</td><td>2</td><td>3</td></tr> <tr><td>1</td><td>2</td><td>3</td><td>3</td></tr> <tr><td>4</td><td>2</td><td>4</td><td>1</td></tr> <tr><td>4</td><td>1</td><td>2</td><td>3</td></tr> </table>	1	2	2	3	1	2	3	3	4	2	4	1	4	1	2	3	<table style="border-collapse: collapse; text-align: center;"> <tr><td colspan="4">j</td></tr> <tr><td></td><td>0</td><td>3</td><td>0</td><td>0</td></tr> <tr><td>i</td><td>0</td><td>1</td><td>3</td><td>1</td></tr> <tr><td></td><td>0</td><td>0</td><td>1</td><td>0</td></tr> <tr><td></td><td>2</td><td>1</td><td>0</td><td>0</td></tr> </table>	j					0	3	0	0	i	0	1	3	1		0	0	1	0		2	1	0	0	<table style="border-collapse: collapse; text-align: center;"> <tr><td colspan="4">j</td></tr> <tr><td></td><td>0</td><td>0</td><td>0</td><td>2</td></tr> <tr><td>i</td><td>3</td><td>1</td><td>0</td><td>1</td></tr> <tr><td></td><td>0</td><td>3</td><td>1</td><td>0</td></tr> <tr><td></td><td>0</td><td>1</td><td>0</td><td>0</td></tr> </table>	j					0	0	0	2	i	3	1	0	1		0	3	1	0		0	1	0	0
1	2	2	3																																																															
1	2	3	3																																																															
4	2	4	1																																																															
4	1	2	3																																																															
j																																																																		
	0	3	0	0																																																														
i	0	1	3	1																																																														
	0	0	1	0																																																														
	2	1	0	0																																																														
j																																																																		
	0	0	0	2																																																														
i	3	1	0	1																																																														
	0	3	1	0																																																														
	0	1	0	0																																																														
(a) Grey levels	(b) $\mathbf{M}_{\mathbf{x}_+ = \rightarrow}$	(c) $\mathbf{M}_{\mathbf{x}_- = \leftarrow}$																																																																

Table 4.3: Grey levels (a) and corresponding grey level co-occurrence matrices for the 0° (b) and 180° directions (c). In vector notation these directions are $\mathbf{x}_+ = (1, 0)$ and $\mathbf{x}_- = (-1, 0)$. To calculate the symmetrical co-occurrence matrix $\mathbf{M}_{\mathbf{x}}$ both matrices are summed by element.

GLCM features rely on the probability distribution for the elements of the GLCM. Let us consider $\mathbf{M}_{\mathbf{x}=(1,0)}$ from the example, as shown in Table 4.5. We derive a probability distribution for grey level co-occurrences, $\mathbf{P}_{\mathbf{x}}$, by normalising $\mathbf{M}_{\mathbf{x}}$ by the sum of its elements. Each element p_{ij} of $\mathbf{P}_{\mathbf{x}}$ is then the joint probability of grey levels i and j occurring in neighbouring voxels along direction \mathbf{x} . Then $p_{i\cdot} = \sum_{j=1}^{N_g} p_{ij}$ is the row marginal probability, and $p_{\cdot j} = \sum_{i=1}^{N_g} p_{ij}$ is the column marginal probability. As $\mathbf{P}_{\mathbf{x}}$ is by definition symmetric, $p_{i\cdot} = p_{\cdot j}$. Furthermore, let us consider diagonal and cross-diagonal probabilities p_{i-j} and p_{i+j} (Haralick et al., 1973; Unser, 1986):

$$\begin{aligned}
 p_{i-j,k} &= \sum_{i=1}^{N_g} \sum_{j=1}^{N_g} p_{ij} [k = |i - j|] & k = 0, \dots, N_g - 1 \\
 p_{i+j,k} &= \sum_{i=1}^{N_g} \sum_{j=1}^{N_g} p_{ij} [k = i + j] & k = 2, \dots, 2N_g
 \end{aligned}$$

Here, $[\dots]$ is an Iverson bracket, which equals 1 when the condition within the brackets is true and 0 otherwise. In effect we select only combinations of elements (i, j) for which the condition holds.

It should be noted that while a distance $\delta = 1$ is commonly used for GLCM, other distances are possible. For example, for $\delta = 3$ (in 3D) the voxels at $(0, 0, 3)$, $(0, 3, 0)$, $(3, 0, 0)$, $(0, 3, 3)$, $(0, 3, -3)$, $(3, 0, 3)$, $(3, 0, -3)$, $(3, 3, 0)$, $(3, -3, 0)$, $(3, 3, 3)$, $(3, 3, -3)$, $(3, -3, 3)$ and $(3, -3, -3)$ from the center voxel are considered.

Summarising features. To improve rotational invariance, GLCM feature values are calculated after combining information from the different matrices (Depeursinge and Fageot, 2017). Five methods can be used to aggregate GLCMs and arrive at a single feature value. A schematic example is shown in Figure 4.2. In three methods, matrices are merged by summing the co-occurrence counts in each matrix element (i, j) over the different matrices. Probability distributions are subsequently calculated for the merged GLCM, which is then used to calculate GLCM features. In the two other methods, features are calculated on the individual GLCMs, and subsequently averaged.

<table border="1" style="border-collapse: collapse; width: 100%;"> <thead> <tr><th colspan="4" style="border-top: 1px solid black; border-bottom: 1px solid black;">j</th></tr> </thead> <tbody> <tr><td style="border-right: 1px solid black; border-bottom: 1px solid black;"></td><td style="border-bottom: 1px solid black;">0</td><td style="border-bottom: 1px solid black;">3</td><td style="border-bottom: 1px solid black;">0</td><td style="border-bottom: 1px solid black;">2</td></tr> <tr><td style="border-right: 1px solid black; border-bottom: 1px solid black;">i</td><td style="border-bottom: 1px solid black;">3</td><td style="border-bottom: 1px solid black;">2</td><td style="border-bottom: 1px solid black;">3</td><td style="border-bottom: 1px solid black;">2</td></tr> <tr><td style="border-right: 1px solid black; border-bottom: 1px solid black;"></td><td style="border-bottom: 1px solid black;">0</td><td style="border-bottom: 1px solid black;">3</td><td style="border-bottom: 1px solid black;">2</td><td style="border-bottom: 1px solid black;">0</td></tr> <tr><td style="border-right: 1px solid black; border-bottom: 1px solid black;"></td><td style="border-bottom: 1px solid black;">2</td><td style="border-bottom: 1px solid black;">2</td><td style="border-bottom: 1px solid black;">0</td><td style="border-bottom: 1px solid black;">0</td></tr> </tbody> </table> <p style="text-align: center;">(a) $M_{\mathbf{x}=\rightarrow}$</p>	j					0	3	0	2	i	3	2	3	2		0	3	2	0		2	2	0	0	<table border="1" style="border-collapse: collapse; width: 100%;"> <thead> <tr><th colspan="4" style="border-top: 1px solid black; border-bottom: 1px solid black;">j</th></tr> </thead> <tbody> <tr><td style="border-right: 1px solid black; border-bottom: 1px solid black;"></td><td style="border-bottom: 1px solid black;">0</td><td style="border-bottom: 1px solid black;">2</td><td style="border-bottom: 1px solid black;">0</td><td style="border-bottom: 1px solid black;">1</td></tr> <tr><td style="border-right: 1px solid black; border-bottom: 1px solid black;">i</td><td style="border-bottom: 1px solid black;">2</td><td style="border-bottom: 1px solid black;">2</td><td style="border-bottom: 1px solid black;">1</td><td style="border-bottom: 1px solid black;">2</td></tr> <tr><td style="border-right: 1px solid black; border-bottom: 1px solid black;"></td><td style="border-bottom: 1px solid black;">0</td><td style="border-bottom: 1px solid black;">1</td><td style="border-bottom: 1px solid black;">2</td><td style="border-bottom: 1px solid black;">1</td></tr> <tr><td style="border-right: 1px solid black; border-bottom: 1px solid black;"></td><td style="border-bottom: 1px solid black;">1</td><td style="border-bottom: 1px solid black;">2</td><td style="border-bottom: 1px solid black;">1</td><td style="border-bottom: 1px solid black;">0</td></tr> </tbody> </table> <p style="text-align: center;">(b) $M_{\mathbf{x}=\nearrow}$</p>	j					0	2	0	1	i	2	2	1	2		0	1	2	1		1	2	1	0
j																																																	
	0	3	0	2																																													
i	3	2	3	2																																													
	0	3	2	0																																													
	2	2	0	0																																													
j																																																	
	0	2	0	1																																													
i	2	2	1	2																																													
	0	1	2	1																																													
	1	2	1	0																																													
<table border="1" style="border-collapse: collapse; width: 100%;"> <thead> <tr><th colspan="4" style="border-top: 1px solid black; border-bottom: 1px solid black;">j</th></tr> </thead> <tbody> <tr><td style="border-right: 1px solid black; border-bottom: 1px solid black;"></td><td style="border-bottom: 1px solid black;">2</td><td style="border-bottom: 1px solid black;">1</td><td style="border-bottom: 1px solid black;">2</td><td style="border-bottom: 1px solid black;">1</td></tr> <tr><td style="border-right: 1px solid black; border-bottom: 1px solid black;">i</td><td style="border-bottom: 1px solid black;">1</td><td style="border-bottom: 1px solid black;">4</td><td style="border-bottom: 1px solid black;">1</td><td style="border-bottom: 1px solid black;">1</td></tr> <tr><td style="border-right: 1px solid black; border-bottom: 1px solid black;"></td><td style="border-bottom: 1px solid black;">2</td><td style="border-bottom: 1px solid black;">1</td><td style="border-bottom: 1px solid black;">2</td><td style="border-bottom: 1px solid black;">1</td></tr> <tr><td style="border-right: 1px solid black; border-bottom: 1px solid black;"></td><td style="border-bottom: 1px solid black;">1</td><td style="border-bottom: 1px solid black;">1</td><td style="border-bottom: 1px solid black;">1</td><td style="border-bottom: 1px solid black;">2</td></tr> </tbody> </table> <p style="text-align: center;">(c) $M_{\mathbf{x}=\uparrow}$</p>	j					2	1	2	1	i	1	4	1	1		2	1	2	1		1	1	1	2	<table border="1" style="border-collapse: collapse; width: 100%;"> <thead> <tr><th colspan="4" style="border-top: 1px solid black; border-bottom: 1px solid black;">j</th></tr> </thead> <tbody> <tr><td style="border-right: 1px solid black; border-bottom: 1px solid black;"></td><td style="border-bottom: 1px solid black;">0</td><td style="border-bottom: 1px solid black;">2</td><td style="border-bottom: 1px solid black;">1</td><td style="border-bottom: 1px solid black;">1</td></tr> <tr><td style="border-right: 1px solid black; border-bottom: 1px solid black;">i</td><td style="border-bottom: 1px solid black;">2</td><td style="border-bottom: 1px solid black;">2</td><td style="border-bottom: 1px solid black;">2</td><td style="border-bottom: 1px solid black;">1</td></tr> <tr><td style="border-right: 1px solid black; border-bottom: 1px solid black;"></td><td style="border-bottom: 1px solid black;">1</td><td style="border-bottom: 1px solid black;">2</td><td style="border-bottom: 1px solid black;">0</td><td style="border-bottom: 1px solid black;">1</td></tr> <tr><td style="border-right: 1px solid black; border-bottom: 1px solid black;"></td><td style="border-bottom: 1px solid black;">1</td><td style="border-bottom: 1px solid black;">1</td><td style="border-bottom: 1px solid black;">1</td><td style="border-bottom: 1px solid black;">0</td></tr> </tbody> </table> <p style="text-align: center;">(d) $M_{\mathbf{x}=\nwarrow}$</p>	j					0	2	1	1	i	2	2	2	1		1	2	0	1		1	1	1	0
j																																																	
	2	1	2	1																																													
i	1	4	1	1																																													
	2	1	2	1																																													
	1	1	1	2																																													
j																																																	
	0	2	1	1																																													
i	2	2	2	1																																													
	1	2	0	1																																													
	1	1	1	0																																													

Table 4.4: Grey level co-occurrence matrices for the 0° (a), 45° (b), 90° (c) and 135° (d) directions. In vector notation these directions are $\mathbf{x} = (1, 0)$, $\mathbf{x} = (1, 1)$, $\mathbf{x} = (0, 1)$ and $\mathbf{x} = (-1, 1)$, respectively.

4.6.1 Joint maximum

Joint maximum (Aerts et al., 2014) is the probability corresponding to the most common grey level co-occurrence in the GLCM.

$$F_{cm.joint.max} = \max(p_{ij})$$

4.6.2 Joint average

Joint average (Unser, 1986) is the grey level weighted sum of joint probabilities.

$$F_{cm.joint.avg} = \sum_{i=1}^{N_g} \sum_{j=1}^{N_g} i p_{ij}$$

4.6.3 Joint variance

The *joint variance* (Unser, 1986) which is also called *sum of squares* (Haralick et al., 1973), is defined as:

$$F_{cm.joint.var} = \sum_{i=1}^{N_g} \sum_{j=1}^{N_g} (i - \mu)^2 p_{ij}$$

Here μ is equal to the value of $F_{cm.joint.avg}$, which was defined previously.

		j				\sum_j
i	0	3	0	2	5	
	3	2	3	2	10	
	0	3	2	0	5	
	2	2	0	0	4	
\sum_i	5	10	5	4	24	

(a) $M_{\Delta=(1,0)}$ with margins

		j				$p_{i.}$
i	0	0.00	0.13	0.00	0.08	0.21
	3	0.13	0.08	0.13	0.08	0.42
	0	0.00	0.13	0.08	0.00	0.21
	2	0.08	0.08	0.00	0.00	0.17
$p_{.j}$	0.21	0.42	0.21	0.17	1.00	

(b) $P_{\Delta=(1,0)}$ with margins

$k = i - j $	0	1	2	3
p_{i-j}	0.17	0.50	0.17	0.17

(c) Diagonal probability for $P_{\Delta=(1,0)}$

$k = i + j$	2	3	4	5	6	7	8
p_{i+j}	0.00	0.25	0.08	0.42	0.25	0.00	0.00

(d) Cross-diagonal probability for $P_{\Delta=(1,0)}$

Table 4.5: Grey level co-occurrence matrix for the 0° direction (a); its corresponding probability matrix $P_{\Delta=(1,0)}$ with marginal probabilities $p_{i.}$ and $p_{.j}$ (b); the diagonal probabilities p_{i-j} (c); and the cross-diagonal probabilities p_{i+j} (d). Discrepancies in panels b, c, and d are due to rounding errors caused by showing only two decimal places. Also, note that due to GLCM symmetry marginal probabilities $p_{i.}$ and $p_{.j}$ are the same in both row and column margins of panel b.

4.6.4 Joint entropy

Joint entropy (Haralick et al., 1973) is defined as:

$$F_{cm.joint.ent} = - \sum_{i=1}^{N_g} \sum_{j=1}^{N_g} p_{ij} \log_2 p_{ij}$$

4.6.5 Difference average

The *difference average* (Unser, 1986) for the diagonal probabilities is defined as:

$$F_{cm.diff.avg} = \sum_{k=0}^{N_g-1} k p_{i-j,k}$$

By definition *difference average* is equivalent to the *dissimilarity* feature (van Griethuysen et al., 2017).

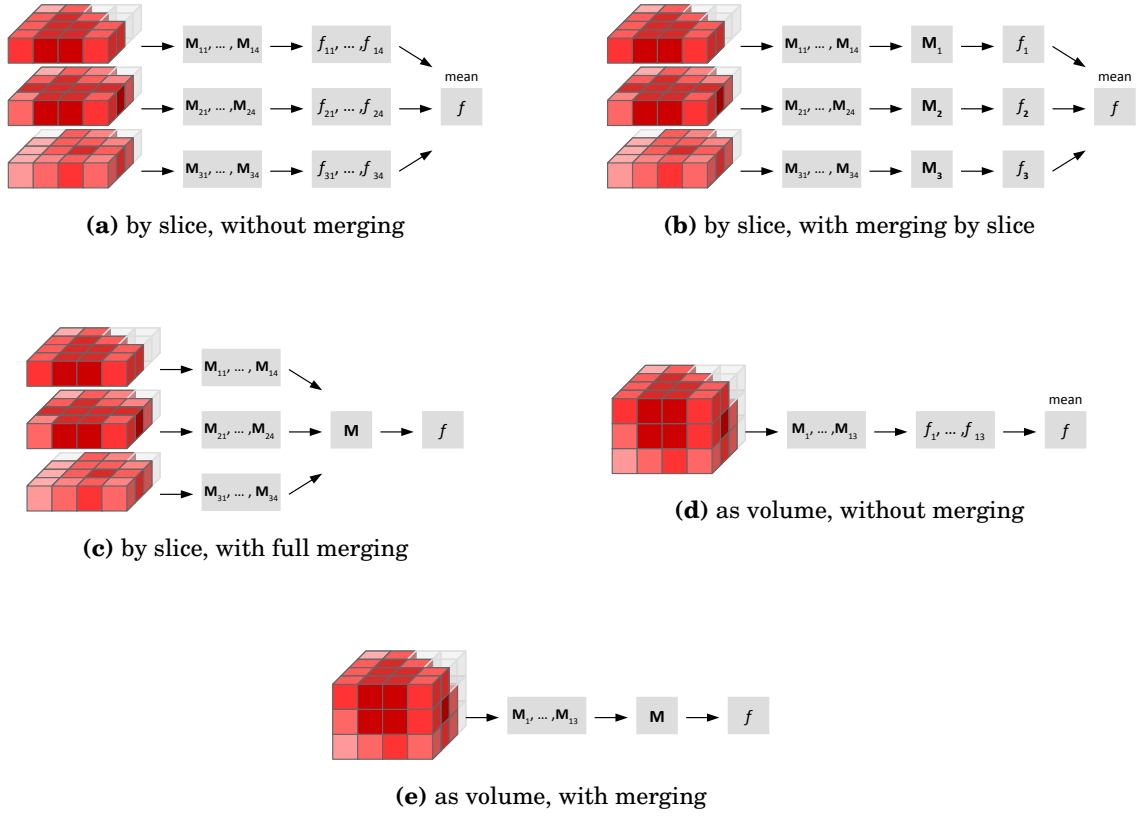


Figure 4.2: Approaches to calculating grey level co-occurrence matrix-based features. $M_{\Delta k}$ are texture matrices calculated for direction Δ in slice k (if applicable), and $f_{\Delta k}$ is the corresponding feature value. In (b), (c) and (e) the matrices are merged prior to feature calculation.

4.6.6 Difference variance

The *difference variance* for the diagonal probabilities (Haralick et al., 1973) is defined as:

$$F_{cm.diff.var} = \sum_{k=0}^{N_g-1} (k - \mu)^2 p_{i-j,k}$$

Here μ is equal to the value of *difference average*.

4.6.7 Difference entropy

The *difference entropy* for the diagonal probabilities (Haralick et al., 1973) is defined as:

$$F_{cm.diff.ent} = - \sum_{k=0}^{N_g-1} p_{i-j}(k) \log_2 p_{i-j,k}$$

4.6.8 Sum average

The *sum average* for the cross-diagonal probabilities (Haralick et al., 1973) is defined as:

$$F_{cm.sum.avg} = \sum_{k=2}^{2N_g} k p_{i+j,k}$$

By definition, $F_{cm.sum.avg} = 2F_{cm.joint.avg}$ (van Griethuysen et al., 2017).

4.6.9 Sum variance

The *sum variance* for the cross-diagonal probabilities (Haralick et al., 1973) is defined as:

$$F_{cm.sum.var} = \sum_{k=2}^{2N_g} (k - \mu)^2 p_{i+j,k}$$

Here μ is equal to the value of *sum average*. *Sum variance* is mathematically identical to the *cluster tendency* feature (van Griethuysen et al., 2017).

4.6.10 Sum entropy

The *sum entropy* for the cross-diagonal probabilities (Haralick et al., 1973) is defined as:

$$F_{cm.sum.entr} = - \sum_{k=2}^{2N_g} p_{i+j,k} \log_2 p_{i+j,k}$$

4.6.11 Angular second moment

The *angular second moment* (Haralick et al., 1973), which represents the energy of P_{Δ} , is defined as:

$$F_{cm.energy} = \sum_{i=1}^{N_g} \sum_{j=1}^{N_g} p_{ij}^2$$

This feature is also called *energy* (Unser, 1986; Aerts et al., 2014) and *uniformity* (Clausi, 2002).

4.6.12 Contrast

Contrast assesses grey level variations (Haralick et al., 1973). Hence elements of M_{Δ} that represent large grey level differences receive greater weight. *Contrast* is defined as (Clausi, 2002):

$$F_{cm.contrast} = \sum_{i=1}^{N_g} \sum_{j=1}^{N_g} (i - j)^2 p_{ij}$$

Note that the original definition by Haralick et al. (1973) is seemingly more complex, but simplifying terms leads to the formulation of *contrast* presented above.

4.6.13 Dissimilarity

Dissimilarity (Clausi, 2002) is conceptually similar to the *contrast* feature, and is defined as:

$$F_{cm.dissimilarity} = \sum_{i=1}^{N_g} \sum_{j=1}^{N_g} |i - j| p_{ij}$$

By definition is *dissimilarity* equivalent to the *difference average* feature (van Griethuysen et al., 2017).

4.6.14 Inverse difference

Inverse difference is a measure of homogeneity (Clausi, 2002). Grey level co-occurrences with a large difference in levels are weighed less, thus lowering the total feature value. The feature score is maximal if all grey levels are the same. Inverse difference is defined as:

$$F_{cm.inv.diff} = \sum_{i=1}^{N_g} \sum_{j=1}^{N_g} \frac{p_{ij}}{1 + |i - j|}$$

4.6.15 Inverse difference normalised

Clausi (2002) suggests normalising *inverse difference* to improve classification ability. The normalised feature is then defined as:

$$F_{cm.inv.diff.norm} = \sum_{i=1}^{N_g} \sum_{j=1}^{N_g} \frac{p_{ij}}{1 + |i - j|/N_g}$$

Note that in Clausi's definition, $|i - j|^2/N_g^2$ is used instead of $|i - j|/N_g$, which is likely an oversight, as this exactly the same definition as the *inverse difference moment normalised* function.

4.6.16 Inverse difference moment

Inverse difference moment (Haralick et al., 1973) is similar in concept to the *inverse difference* feature, but with lower weights for elements that are further from the diagonal.

$$F_{cm.inv.diff.mom} = \sum_{i=1}^{N_g} \sum_{j=1}^{N_g} \frac{p_{ij}}{1 + (i - j)^2}$$

This feature is also called *homogeneity* (Unser, 1986).

4.6.17 Inverse difference moment normalised

Clausi (2002) suggests normalising *inverse difference moment* to improve classification performance. This leads to the following definition:

$$F_{cm.inv.diff.mom.norm} = \sum_{i=1}^{N_g} \sum_{j=1}^{N_g} \frac{p_{ij}}{1 + (i - j)^2 / N_g^2}$$

4.6.18 Inverse variance

The *inverse variance* (Aerts et al., 2014) feature is defined as:

$$F_{cm.inv.var} = 2 \sum_{i=1}^{N_g} \sum_{j>i}^{N_g} \frac{p_{ij}}{(i-j)^2}$$

4.6.19 Correlation

Correlation (Haralick et al., 1973) is defined as:

$$F_{cm.corr} = \frac{1}{\sigma_i \sigma_j} \left(-\mu_i \mu_j + \sum_{i=1}^{N_g} \sum_{j=1}^{N_g} i j p_{ij} \right)$$

$\mu_i = \sum_{i=1}^{N_g} i p_i$ and $\sigma_i = \left(\sum_{i=1}^{N_g} (i - \mu_i)^2 p_i \right)^{1/2}$ are the mean and standard deviation of row marginal probability p_i , respectively. Likewise, μ_j and σ_j are the mean and standard deviation of the column marginal probability p_j , respectively. The calculation of *correlation* can be simplified since \mathbf{P}_Δ is symmetrical:

$$F_{cm.corr} = \frac{1}{\sigma_i^2} \left(-\mu_i^2 + \sum_{i=1}^{N_g} \sum_{j=1}^{N_g} i j p_{ij} \right)$$

An equivalent formulation of *correlation* is:

$$F_{cm.corr} = \frac{1}{\sigma_i \sigma_j} \sum_{i=1}^{N_g} \sum_{j=1}^{N_g} (i - \mu_i) (j - \mu_j) p_{ij}$$

Again, simplifying due to matrix symmetry yields:

$$F_{cm.corr} = \frac{1}{\sigma_i^2} \sum_{i=1}^{N_g} \sum_{j=1}^{N_g} (i - \mu_i) (j - \mu_i) p_{ij}$$

4.6.20 Autocorrelation

Aerts et al. (2014) defined *autocorrelation* as:

$$F_{cm.auto.corr} = \sum_{i=1}^{N_g} \sum_{j=1}^{N_g} i j p_{ij}$$

4.6.21 Cluster tendency

Cluster tendency (Aerts et al., 2014) is defined as:

$$F_{cm.clust.tend} = \sum_{i=1}^{N_g} \sum_{j=1}^{N_g} (i + j - \mu_i - \mu_j)^2 p_{ij}$$

Here $\mu_{i.} = \sum_{i=1}^{N_g} i p_{i.}$ and $\mu_{.j} = \sum_{j=1}^{N_g} j p_{.j}$. Because of the symmetric nature of P_{Δ} , the feature can also be formulated as:

$$F_{cm.clust.tend} = \sum_{i=1}^{N_g} \sum_{j=1}^{N_g} (i + j - 2\mu_{i.})^2 p_{ij}$$

Cluster tendency is mathematically equal to the *sum variance* feature (van Griethuysen et al., 2017).

4.6.22 Cluster shade

Cluster shade (Unser, 1986) is defined as:

$$F_{cm.clust.shade} = \sum_{i=1}^{N_g} \sum_{j=1}^{N_g} (i + j - \mu_{i.} - \mu_{.j})^3 p_{ij}$$

As with *cluster tendency*, $\mu_{i.} = \sum_{i=1}^{N_g} i p_{i.}$ and $\mu_{.j} = \sum_{j=1}^{N_g} j p_{.j}$. Because of the symmetric nature of P_{Δ} , the feature can also be formulated as:

$$F_{cm.clust.shade} = \sum_{i=1}^{N_g} \sum_{j=1}^{N_g} (i + j - 2\mu_{i.})^3 p_{ij}$$

4.6.23 Cluster prominence

Cluster prominence (Unser, 1986) is defined as:

$$F_{cm.clust.prom} = \sum_{i=1}^{N_g} \sum_{j=1}^{N_g} (i + j - \mu_{i.} - \mu_{.j})^4 p_{ij}$$

As before, $\mu_{i.} = \sum_{i=1}^{N_g} i p_{i.}$ and $\mu_{.j} = \sum_{j=1}^{N_g} j p_{.j}$. Because of the symmetric nature of P_{Δ} , the feature can also be formulated as:

$$F_{cm.clust.prom} = \sum_{i=1}^{N_g} \sum_{j=1}^{N_g} (i + j - 2\mu_{i.})^4 p_{ij}$$

4.6.24 First measure of information correlation

Information theoretic correlation is estimated using two different measures (Haralick et al., 1973). For symmetric P_{Δ} the first measure is defined as:

$$F_{cm.info.corr.1} = \frac{HXY - HXY_1}{HX}$$

$HXY = -\sum_{i=1}^{N_g} \sum_{j=1}^{N_g} p_{ij} \log_2 p_{ij}$ is the entropy for the joint probability. $HX = -\sum_{i=1}^{N_g} p_{i.} \log_2 p_{i.}$ is the entropy for the row marginal probability, which due to symmetry is equal to the entropy of the column marginal probability. HXY_1 is a type of entropy that is defined as:

$$HXY_1 = -\sum_{i=1}^{N_g} \sum_{j=1}^{N_g} p_{ij} \log_2 (p_{i.} p_{.j})$$

4.6.25 Second measure of information correlation

The *second measure of information theoretic correlation* (Haralick et al., 1973) is estimated as follows for symmetric P_{Δ} :

$$F_{cm.info.corr.2} = \sqrt{1 - \exp(-2(HXY_2 - HXY))}$$

As earlier, $HXY = -\sum_{i=1}^{N_g} \sum_{j=1}^{N_g} p_{ij} \log_2 p_{ij}$. HXY_2 is a type of entropy defined as:

$$HXY_2 = -\sum_{i=1}^{N_g} \sum_{j=1}^{N_g} p_{i.p.j} \log_2 (p_{i.p.j})$$

If $HXY > HXY_2$, $F_{cm.info.corr.2} = 0$, as this would otherwise lead to complex numbers.

4.7 Texture features - Grey level run length based features

The grey level run length matrix (GLRLM) was introduced by Galloway (1975) to define various texture features. Like the grey level co-occurrence matrix, GLRLM also assesses the distribution of discretised grey levels in an image or in a stack of images. However, whereas GLCM assesses co-occurrence of grey levels within neighbouring pixels or voxels, GLRLM assesses run lengths. A run length is defined as the length of a consecutive sequence of pixels or voxels with the same grey level along direction x , which was previously defined in Section 4.6. The GLRLM then contains the occurrences of runs with length j for a discretised grey level i .

A complete example for GLRLM construction from a 2D image is shown in Table 4.6. Let M_x be the $N_g \times N_r$ grey level run length matrix, where N_g is the number of discretised grey levels present in the ROI intensity mask and N_r the maximal possible run length along direction x . Matrix element r_{ij} of the GLRLM is the occurrence of grey level i with run length j . Then, let N_v be the total number of voxels in the ROI intensity mask, and $N_s = \sum_{i=1}^{N_g} \sum_{j=1}^{N_r} r_{ij}$ the sum over all elements in M_x . Marginal sums are also defined. Let $r_{i.}$ be the marginal sum of the runs over run lengths j for grey value i , that is $r_{i.} = \sum_{j=1}^{N_r} r_{ij}$. Similarly, the marginal sum of the runs over the grey values i for run length j is $r_{.j} = \sum_{i=1}^{N_g} r_{ij}$.

Summarising features. To improve rotational invariance, GLRLM feature values are calculated after combining information from the different matrices (Depeursinge and Fageot, 2017). Five methods can be used to aggregate GLRLMs and arrive at a single feature value. A schematic example was previously shown in Figure 4.2. In three methods, matrices are merged by summing run counts of each matrix element (i, j) for the different GLRLM matrices. Probability distributions are subsequently calculated for the merged GLRLM, which is then used to calculate GLRLM features. Note that when matrices are merged, N_v should likewise be summed to retain consistency. In the two other methods, features are calculated on the individual GLRLMs, and subsequently averaged.

1	2	2	3
1	2	3	3
4	2	4	1
4	1	2	3

(a) Grey levels

		Run length j						Run length j			
		1	2	3	4			1	2	3	4
i	1	4	0	0	0	i	1	4	0	0	0
	2	3	1	0	0		2	3	1	0	0
	3	2	1	0	0		3	2	1	0	0
	4	3	0	0	0		4	3	0	0	0

(b) $M_{\mathbf{x}=\rightarrow}$

(c) $M_{\mathbf{x}=\nearrow}$

		Run length j						Run length j			
		1	2	3	4			1	2	3	4
i	1	2	1	0	0	i	1	4	0	0	0
	2	2	0	1	0		2	3	1	0	0
	3	2	1	0	0		3	4	0	0	0
	4	1	1	0	0		4	3	0	0	0

(d) $M_{\mathbf{x}=\uparrow}$

(e) $M_{\mathbf{x}=\nwarrow}$

Table 4.6: Grey level run length matrices for the 0° (a), 45° (b), 90° (c) and 135° (d) directions. In vector notation these directions are $\mathbf{x} = (1, 0)$, $\mathbf{x} = (1, 1)$, $\mathbf{x} = (0, 1)$ and $\mathbf{x} = (-1, 1)$, respectively.

4.7.1 Short runs emphasis

This feature emphasises short run lengths (Galloway, 1975). It is defined as:

$$F_{rlm.sre} = \frac{1}{N_s} \sum_{j=1}^{N_r} \frac{r.j}{j^2}$$

4.7.2 Long runs emphasis

This feature emphasises long run lengths (Galloway, 1975). It is defined as:

$$F_{rlm.lre} = \frac{1}{N_s} \sum_{j=1}^{N_r} j^2 r.j$$

4.7.3 Low grey level run emphasis

This feature is a grey level analogue to *short runs emphasis* (Chu et al., 1990). Instead of short run lengths, low grey levels are emphasised. The feature is defined as:

$$F_{rlm.lgre} = \frac{1}{N_s} \sum_{i=1}^{N_g} \frac{r_i}{i^2}$$

4.7.4 High grey level run emphasis

The *high grey level run emphasis* feature is a grey level analogue to *long runs emphasis* (Chu et al., 1990). The feature emphasises high grey levels, and is defined as:

$$F_{rlm.hgre} = \frac{1}{N_s} \sum_{i=1}^{N_g} i^2 r_i$$

4.7.5 Short run low grey level emphasis

This feature emphasises runs in the upper left quadrant of the GLRLM, where short run lengths and low grey levels are located (Dasarathy and Holder, 1991). It is defined as:

$$F_{rlm.srlge} = \frac{1}{N_s} \sum_{i=1}^{N_g} \sum_{j=1}^{N_r} \frac{r_{ij}}{i^2 j^2}$$

4.7.6 Short run high grey level emphasis

This feature emphasises runs in the lower left quadrant of the GLRLM, where short run lengths and high grey levels are located (Dasarathy and Holder, 1991). The feature is defined as:

$$F_{rlm.srhge} = \frac{1}{N_s} \sum_{i=1}^{N_g} \sum_{j=1}^{N_r} \frac{i^2 r_{ij}}{j^2}$$

4.7.7 Long run low grey level emphasis

This feature emphasises runs in the upper right quadrant of the GLRLM, where long run lengths and low grey levels are located (Dasarathy and Holder, 1991). The feature is defined as:

$$F_{rlm.lrlge} = \frac{1}{N_s} \sum_{i=1}^{N_g} \sum_{j=1}^{N_r} \frac{j^2 r_{ij}}{i^2}$$

4.7.8 Long run high grey level emphasis

This feature emphasises runs in the lower right quadrant of the GLRLM, where long run lengths and high grey levels are located (Dasarathy and Holder, 1991). The feature is defined as:

$$F_{rlm.lrhge} = \frac{1}{N_s} \sum_{i=1}^{N_g} \sum_{j=1}^{N_r} i^2 j^2 r_{ij}$$

4.7.9 Grey level non-uniformity

This feature assesses the distribution of runs over the grey values (Galloway, 1975). The feature value is low when runs are equally distributed along grey levels. The feature is defined as:

$$F_{rlm.glnu} = \frac{1}{N_s} \sum_{i=1}^{N_g} r_i^2.$$

4.7.10 Grey level non-uniformity normalised

This is a normalised version of the *grey level non-uniformity feature*. It is defined as:

$$F_{rlm.glnu.norm} = \frac{1}{N_s^2} \sum_{i=1}^{N_g} r_i^2.$$

4.7.11 Run length non-uniformity

This features assesses the distribution of runs over the run lengths (Galloway, 1975). The feature value is low when runs are equally distributed along run lengths. It is defined as:

$$F_{rlm.rlnu} = \frac{1}{N_s} \sum_{j=1}^{N_r} r_j^2.$$

4.7.12 Run length non-uniformity normalised

This is normalised version of the *run length non-uniformity feature*. It is defined as:

$$F_{rlm.rlnu.norm} = \frac{1}{N_s^2} \sum_{j=1}^{N_r} r_j^2.$$

4.7.13 Run percentage

This feature assesses the fraction of the number of realised runs and the maximum number of potential runs (Galloway, 1975). Strongly linear or highly uniform ROI volumes produce a low *run percentage*. It is defined as:

$$F_{rlm.r.perc} = \frac{N_s}{N_v}$$

As noted before, when this feature is calculated using a merged GLRLM, N_v should be the sum of the number of voxels of the underlying matrices to allow proper normalisation.

4.7.14 Grey level variance

This feature estimates the variance in runs for the grey levels. Let $p_{ij} = r_{ij}/N_s$ be the joint probability estimate for finding discretised grey level i with run length j . *Grey level variance* is then defined as:

$$F_{rlm.gl.var} = \sum_{i=1}^{N_g} \sum_{j=1}^{N_r} (i - \mu)^2 p_{ij}$$

Here, $\mu = \sum_{i=1}^{N_g} \sum_{j=1}^{N_r} i p_{ij}$.

4.7.15 Run length variance

This feature estimates the variance in runs for run lengths. As before let $p_{ij} = r_{ij}/N_s$. The feature is defined as:

$$F_{rlm.rl.var} = \sum_{i=1}^{N_g} \sum_{j=1}^{N_r} (j - \mu)^2 p_{ij}$$

Mean run length is defined as $\mu = \sum_{i=1}^{N_g} \sum_{j=1}^{N_r} j p_{ij}$.

4.7.16 Run entropy

Run entropy was investigated by Albrechtsen et al. (2000). Again, let $p_{ij} = r_{ij}/N_s$. The entropy is then defined as:

$$F_{rlm.rl.entr} = - \sum_{i=1}^{N_g} \sum_{j=1}^{N_r} p_{ij} \log_2 p_{ij}$$

4.8 Texture features - Grey level size zone based features

The grey level size zone matrix (GLSZM) counts the number of groups (or zones) of linked voxels (Thibault et al., 2014). Voxels are linked if the neighbouring voxel has an identical discretised grey level. Whether a voxel classifies as a neighbour depends on its connectedness. In a 3D approach to texture analysis we consider 26-connectedness, which indicates that a center voxel is linked to all of the 26 neighbouring voxels with the same grey level. In the 2 dimensional approach, 8-connectedness is used. A potential issue for the 2D approach is that voxels which may otherwise be considered to belong to the same zone by linking across slices, are now two or more separate zones within the slice plane. Whether this issue negatively affects predictive performance of GLSZM-based features or their reproducibility has not been determined.

Let M be the $N_g \times N_z$ grey level size zone matrix, where N_g is the number of discretised grey levels present in the ROI intensity mask and N_z the maximum zone size of any group of linked voxels. Element s_{ij} of M is then the number of zones with discretised grey level i and size j . Furthermore, let N_v be the number of voxels in the intensity mask and $N_s = \sum_{i=1}^{N_g} \sum_{j=1}^{N_z} s_{ij}$ be the total number of zones. Marginal sums can likewise be defined. Let $s_{i.} = \sum_{j=1}^{N_z} s_{ij}$ be the number of zones with discretised grey level i , regardless of size. Likewise, let $s_{.j} = \sum_{i=1}^{N_g} s_{ij}$ be the number of zones with size j , regardless of grey level. A two dimensional example is shown in Table 4.7.

Summarising features. Feature values are calculated after determining the GLSZM(s) for the ROI intensity mask. Three methods can be used to arrive at a single feature value for each volume. Five methods were previously defined for GLCM and GLRLM, but as the GLSZM is not directionally dependent, only three methods remain applicable. A schematic

example is shown in Figure 4.3. One method involves merging GLSZMs by summing the number of zones s_{ij} over the GLSZM for the different slices. Features are subsequently calculated from the merged GLSZM. Note that when GLSZMs are merged, N_v should likewise be summed to retain consistency.

Note on feature references. GLSZM feature definitions are based on the definitions of GLRLM features (Thibault et al., 2014). Hence, references may be found in the section on GLRLM (4.7).

		Zone size j					
		1	2	3	4	5	
1	2	2	3				
1	2	3	3				
4	2	4	1				
4	1	2	3				
		i	1	2	3	4	5
		1	2	1	0	0	0
		2	0	0	0	0	1
		3	1	0	1	0	0
		4	1	1	0	0	0

(a) Grey levels

(b) Grey level size zone matrix

Table 4.7: Original image with grey levels (a); and corresponding grey level size zone matrix (GLSZM) under 8-connectedness (b). Element $s(i, j)$ of the GLSZM indicates the number of times a zone of j linked pixels and grey level i occurs within the image.

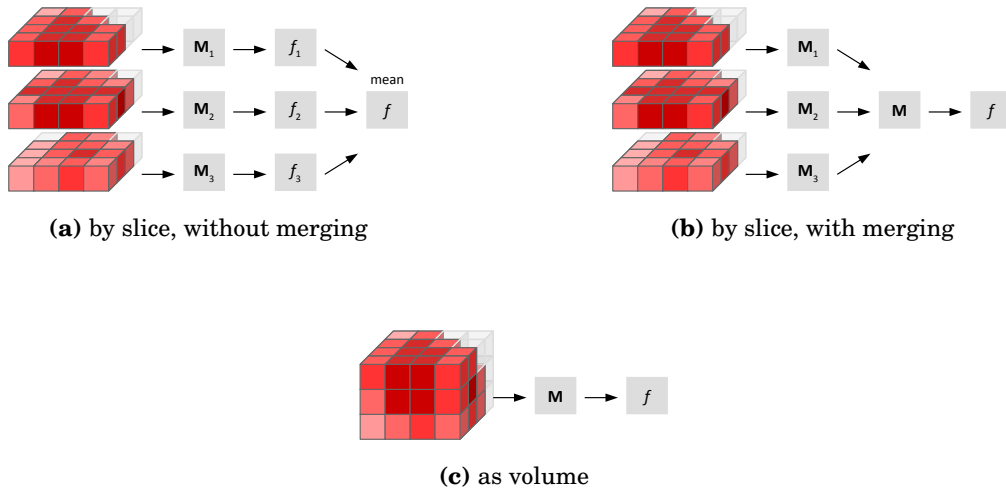


Figure 4.3: Approaches to calculating grey level size zone matrix-based features. M_k are texture matrices calculated for slice k (if applicable), and f_k is the corresponding feature value. In (b) the matrices from the different slices are merged prior to feature calculation.

4.8.1 Small zone emphasis

This feature emphasises small zones. It is defined as:

$$F_{szm.sze} = \frac{1}{N_s} \sum_{j=1}^{N_z} \frac{s_{.j}}{j^2}$$

4.8.2 Large zone emphasis

This feature emphasises large zones. It is defined as:

$$F_{szm.lze} = \frac{1}{N_s} \sum_{j=1}^{N_z} j^2 s_{.j}$$

4.8.3 Low grey level zone emphasis

This feature is a grey level analogue to *small zone emphasis*. Instead of small zone sizes, low grey levels are emphasised. The feature is defined as:

$$F_{szm.lgze} = \frac{1}{N_s} \sum_{i=1}^{N_g} \frac{s_{i.}}{i^2}$$

4.8.4 High grey level zone emphasis

The *high grey level zone emphasis* feature is a grey level analogue to *large zone emphasis*. The feature emphasises high grey levels, and is defined as:

$$F_{szm.hgze} = \frac{1}{N_s} \sum_{i=1}^{N_g} i^2 s_{i.}$$

4.8.5 Small zone low grey level emphasis

This feature emphasises zone counts within the upper left quadrant of the GLSZM, where small zone sizes and low grey levels are located. It is defined as:

$$F_{szm.szlgze} = \frac{1}{N_s} \sum_{i=1}^{N_g} \sum_{j=1}^{N_z} \frac{s_{ij}}{i^2 j^2}$$

4.8.6 Small zone high grey level emphasis

This feature emphasises zone counts in the lower left quadrant of the GLSZM, where small zone sizes and high grey levels are located. The feature is defined as:

$$F_{szm.szhge} = \frac{1}{N_s} \sum_{i=1}^{N_g} \sum_{j=1}^{N_z} \frac{i^2 s_{ij}}{j^2}$$

4.8.7 Large zone low grey level emphasis

This feature emphasises zone counts in the upper right quadrant of the GLSZM, where large zone sizes and low grey levels are located. The feature is defined as:

$$F_{szm.lzlgc} = \frac{1}{N_s} \sum_{i=1}^{N_g} \sum_{j=1}^{N_z} \frac{j^2 s_{ij}}{i^2}$$

4.8.8 Large zone high grey level emphasis

This feature emphasises zone counts in the lower right quadrant of the GLSZM, where large zone sizes and high grey levels are located. The feature is defined as:

$$F_{szm.lzhgc} = \frac{1}{N_s} \sum_{i=1}^{N_g} \sum_{j=1}^{N_z} i^2 j^2 s_{ij}$$

4.8.9 Grey level non-uniformity

This feature assesses the distribution of zone counts over the grey values. The feature value is low when zone counts are equally distributed along grey levels. The feature is defined as:

$$F_{szm.glnu} = \frac{1}{N_s} \sum_{i=1}^{N_g} s_i^2$$

4.8.10 Grey level non-uniformity normalised

This is a normalised version of the *grey level non-uniformity* feature. It is defined as:

$$F_{szm.glnu.norm} = \frac{1}{N_s^2} \sum_{i=1}^{N_g} s_i^2$$

4.8.11 Zone size non-uniformity

This feature assesses the distribution of zone counts over the different zone sizes. *Zone size non-uniformity* is low when zone counts are equally distributed along zone sizes. It is defined as:

$$F_{szm.zsnu} = \frac{1}{N_s} \sum_{j=1}^{N_z} s_{.j}^2$$

4.8.12 Zone size non-uniformity normalised

This is a normalised version of *zone size non-uniformity*. It is defined as:

$$F_{szm.zsnu.norm} = \frac{1}{N_s^2} \sum_{j=1}^{N_z} s_{.j}^2$$

4.8.13 Zone percentage

This feature assesses the fraction of the number of realised zones and the maximum number of potential zones. Highly uniform ROIs produce a low *zone percentage*. It is defined as:

$$F_{szm.z.perc} = \frac{N_s}{N_v}$$

4.8.14 Grey level variance

This feature estimates the variance in zone counts for the grey levels. Let $p_{ij} = s_{ij}/N_s$ be the joint probability estimate for finding zones with discretised grey level i and size j . The feature is then defined as:

$$F_{szm.gl.var} = \sum_{i=1}^{N_g} \sum_{j=1}^{N_z} (i - \mu)^2 p_{ij}$$

Here, $\mu = \sum_{i=1}^{N_g} \sum_{j=1}^{N_z} i p_{ij}$.

4.8.15 Zone size variance

This feature estimates the variance in zone counts for the different zone sizes. As before let $p_{ij} = s_{ij}/N_s$. The feature is defined as:

$$F_{szm.zs.var} = \sum_{i=1}^{N_g} \sum_{j=1}^{N_z} (j - \mu)^2 p_{ij}$$

Mean zone size is defined as $\mu = \sum_{i=1}^{N_g} \sum_{j=1}^{N_z} j p_{ij}$.

4.8.16 Zone size entropy

Let $p_{ij} = s_{ij}/N_s$. *Zone size entropy* is then defined as:

$$F_{szm.zs.ent} = - \sum_{i=1}^{N_g} \sum_{j=1}^{N_z} p_{ij} \log_2 p_{ij}$$

4.9 Texture features - Grey level distance zone based features

The grey level distance zone matrix (GLDZM) counts the number of groups (or zones) of linked voxels which share a specific discretised grey level value and possess the same distance to ROI edge (Thibault et al., 2014). The GLDZM thus captures the relation between location and grey level. Two maps are required to calculate the GLDZM. The first is a grey level zone map, which is identical to the one created for the grey level size zone matrix (GLSZM), see Section 4.8. The second is a distance map, which will be described in detail later.

As with GSLZM, neighbouring voxels are linked if they share the same grey level value. Whether a voxel classifies as a neighbour depends on its connectedness. We consider 26-connectedness for a 3D approach and 8-connectedness in the 2D approach.

The distance to the ROI edge is defined according to 6 and 4-connectedness for 3D and 2D, respectively. Because of the connectedness definition used, the distance of a voxel to the outer border is equal to the minimum number edges of neighbouring voxels that need to be crossed to reach the ROI edge. The distance for a linked group of voxels with the same grey value is equal to the minimum distance for the respective voxels in the distance map.

Our definition deviates from the original by Thibault et al. (2014). The original was defined in a rectangular 2D image, whereas ROIs are rarely rectangular cuboids. Approximating distance using Chamfer maps is then no longer a fast and easy solution. Determining distance iteratively in 6 or 4-connectedness is a relatively efficient solution, implemented as follows:

1. The ROI mask is morphologically eroded using the appropriate (6 or 4-connected) structure element.
2. All eroded ROI voxels are updated in the distance map by adding 1.
3. The above steps are performed iteratively until the ROI mask is empty.

A second difference with the original definition is that the lowest possible distance is 1 instead of 0 for voxels directly on the ROI edge. This prevents division by 0 for some features.

Let M be the $N_g \times N_d$ grey level size zone matrix, where N_g is the number of discretised grey levels present in the ROI intensity mask and N_d the largest distance of any zone. Element $d_{ij} = d(i, j)$ of M is then number of zones with discretised grey level i and distance j . Furthermore, let N_v be the number of voxels and $N_s = \sum_{i=1}^{N_g} \sum_{j=1}^{N_d} d_{ij}$ be the total zone count. Marginal sums can likewise be defined. Let $d_{i.} = \sum_{j=1}^{N_d} d_{ij}$ be the number of zones with discretised grey level i , regardless of distance. Likewise, let $d_{.j} = \sum_{i=1}^{N_g} d_{ij}$ be the number of zones with distance j , regardless of grey level. A two dimensional example is shown in Table 4.8.

Morphological and intensity masks. The GLDZM is special in that it uses both ROI masks. The distance map is determined using the morphological ROI mask, whereas the intensity mask is used for determining the zones, as with the GLSZM.

Summarising features. Feature values are calculated after determining the GLDZM(s) for the ROI intensity mask. Three methods can be used to arrive at a single feature value for each volume. Five methods were previously defined for GLCM and GLRLM, but as the GLDZM is not directionally dependent, only three methods remain applicable. A schematic example was shown previously in Figure 4.3. One method involves merging GLDZMs by summing the number of zones d_{ij} over the GLDZM for the different slices. Features are subsequently calculated from the merged GLDZM. Note that when GLDZMs are merged, N_v should likewise be summed to retain consistency.

Note on feature references. GLDZM feature definitions are based on the definitions of GLRLM features (Thibault et al., 2014). Hence, references may be found in the section on GLRLM (4.7).

		<u> </u>				<u> </u>				
									d	
									1 2	
		1	2	2	3	1	1	1	1	
		1	2	3	3	1	2	2	1	
		4	2	4	1	1	2	2	1	
		4	1	2	3	1	1	1	1	
		<u> </u>				<u> </u>				
		(a) Grey levels				(b) Distance map				
									i	
									1 3 0	
									2 2 0	
									3 2 0	
									4 1 1	
		<u> </u>				<u> </u>				

Table 4.8: Original image with grey levels (a); corresponding distance map for distance to border (b); and corresponding grey level distance zone matrix (GLDZM) under 4-connectedness (c). Element $d(i, j)$ of the GLDZM indicates the number of times a zone with grey level i and a minimum distance to border j occurs within the image.

4.9.1 Small distance emphasis

This feature emphasises small distances. It is defined as:

$$F_{dzm.sde} = \frac{1}{N_s} \sum_{j=1}^{N_d} \frac{d_{.j}}{j^2}$$

4.9.2 Large distance emphasis

This feature emphasises large distances. It is defined as:

$$F_{dzm.lde} = \frac{1}{N_s} \sum_{j=1}^{N_d} j^2 d_{.j}$$

4.9.3 Low grey level zone emphasis

This feature is a grey level analogue to *small distance emphasis*. Instead of small zone distances, low grey levels are emphasised. The feature is defined as:

$$F_{dzm.lgze} = \frac{1}{N_s} \sum_{i=1}^{N_g} \frac{d_{i.}}{i^2}$$

4.9.4 High grey level zone emphasis

The *high grey level zone emphasis* feature is a grey level analogue to *large distance emphasis*. The feature emphasises high grey levels, and is defined as:

$$F_{dzm.hgze} = \frac{1}{N_s} \sum_{i=1}^{N_g} i^2 d_{i.}$$

4.9.5 Small distance low grey level emphasis

This feature emphasises runs in the upper left quadrant of the GLDZM, where small zone distances and low grey levels are located. It is defined as:

$$F_{dzm..sdlge} = \frac{1}{N_s} \sum_{i=1}^{N_g} \sum_{j=1}^{N_d} \frac{d_{ij}}{i^2 j^2}$$

4.9.6 Small distance high grey level emphasis

This feature emphasises runs in the lower left quadrant of the GLDZM, where small zone distances and high grey levels are located. *Small distance high grey level emphasis* is defined as:

$$F_{dzm..sdhge} = \frac{1}{N_s} \sum_{i=1}^{N_g} \sum_{j=1}^{N_d} \frac{i^2 d_{ij}}{j^2}$$

4.9.7 Large distance low grey level emphasis

This feature emphasises runs in the upper right quadrant of the GLDZM, where large zone distances and low grey levels are located. The feature is defined as:

$$F_{dzm..ldlge} = \frac{1}{N_s} \sum_{i=1}^{N_g} \sum_{j=1}^{N_d} \frac{j^2 d_{ij}}{i^2}$$

4.9.8 Large distance high grey level emphasis

This feature emphasises runs in the lower right quadrant of the GLDZM, where large zone distances and high grey levels are located. *Large distance high grey level emphasis* feature is defined as:

$$F_{dzm..ldhge} = \frac{1}{N_s} \sum_{i=1}^{N_g} \sum_{j=1}^{N_d} i^2 j^2 d_{ij}$$

4.9.9 Grey level non-uniformity

This feature assesses the distribution of zone counts over the grey values. *Grey level non-uniformity* is low when zone counts are equally distributed along grey levels. The feature is defined as:

$$F_{dzm..glnu} = \frac{1}{N_s} \sum_{i=1}^{N_g} d_i^2$$

4.9.10 Grey level non-uniformity normalised

This is a normalised version of the *grey level non-uniformity feature*. It is defined as:

$$F_{dzm..glnu.norm} = \frac{1}{N_s^2} \sum_{i=1}^{N_g} d_i^2$$

4.9.11 Zone distance non-uniformity

Zone distance non-uniformity assesses the distribution of zone counts over the different zone distances. *Zone distance non-uniformity* is low when zone counts are equally distributed along zone distances. It is defined as:

$$F_{dzm.zdnu} = \frac{1}{N_s} \sum_{j=1}^{N_d} d_{\cdot j}^2$$

4.9.12 Zone distance non-uniformity normalised

This is a normalised version of the *zone distance non-uniformity* feature. It is defined as:

$$F_{dzm.zdnu.norm} = \frac{1}{N_s^2} \sum_{i=1}^{N_d} d_{\cdot i}^2$$

4.9.13 Zone percentage

This feature assesses the fraction of the number of realised zones and the maximum number of potential zones. Highly uniform ROIs produce a low *zone percentage*. It is defined as:

$$F_{dzm.z.perc} = \frac{N_s}{N_v}$$

4.9.14 Grey level variance

This feature estimates the variance in zone counts for the grey levels. Let $p_{ij} = d_{ij}/N_s$ be the joint probability estimate for finding zones with discretised grey level i at distance j . The feature is then defined as:

$$F_{dzm.gl.var} = \sum_{i=1}^{N_g} \sum_{j=1}^{N_d} (i - \mu)^2 p_{ij}$$

Here, $\mu = \sum_{i=1}^{N_g} \sum_{j=1}^{N_d} i p_{ij}$.

4.9.15 Zone distance variance

This feature estimates the variance in zone counts for the different zone distances. As before let $p_{ij} = d_{ij}/N_s$. The feature is defined as:

$$F_{dzm.zd.var} = \sum_{i=1}^{N_g} \sum_{j=1}^{N_d} (j - \mu)^2 p_{ij}$$

Mean zone size is defined as $\mu = \sum_{i=1}^{N_g} \sum_{j=1}^{N_d} j p_{ij}$.

4.9.16 Zone distance entropy

Again, let $p_{ij} = d_{ij}/N_s$. Zone distance entropy is then defined as:

$$F_{dzm.zd.ent} = - \sum_{i=1}^{N_g} \sum_{j=1}^{N_d} p_{ij} \log_2 p_{ij}$$

4.10 Texture features - Neighbourhood grey tone difference based features

Amadasun and King (1989) introduced an alternative to the grey level co-occurrence matrix. The neighbourhood grey tone difference matrix (NGTDM) contains the sum of grey level differences of pixels/voxels with discretised grey level i and the average discretised grey level of neighbouring pixels/voxels within a (*Chebyshev*) distance δ . For 3D volumes, we can extend the original definition by Amadasun and King. Let $X_{d,k}$ be the discretised grey level of a voxel at position $\mathbf{k} = (k_x, k_y, k_z)$. Then the average grey level within a neighbourhood centred at (k_x, k_y, k_z) , but excluding (k_x, k_y, k_z) itself is:

$$\bar{X}_k = \frac{1}{W} \sum_{m_z=-\delta}^{\delta} \sum_{m_y=-\delta}^{\delta} \sum_{m_x=-\delta}^{\delta} X_d(k_x+m_x, k_y+m_y, k_z+m_z)$$

$$(m_x, m_y, m_z) \neq (0, 0, 0)$$

$W = (2\delta+1)^3 - 1$ is the size of the 3D neighbourhood. For 2D $W = (2\delta+1)^2 - 1$, and averages are not calculated over slices. Neighbourhood grey tone difference s_i for discretised grey level i is then:

$$s_i = \sum_k^{N_v} |i - \bar{X}_k| [X_{d,k} = i \text{ and } k \text{ has a valid neighbourhood}]$$

Here, $[\dots]$ is an Iverson bracket, which is 1 if the conditions that the grey level $X_{d,k}$ of voxel k is equal to i and the voxel has a valid neighbourhood are both true; it is 0 otherwise. N_v is the number of voxels in the ROI intensity mask.

A 2D example is shown in Table 4.9. A distance of $\delta = 1$ is used in this example, leading to 8 neighbouring pixels. Entry $s_1 = 0$ because there are no valid pixels with grey level 1. Two pixels have grey level 2. The average value of their neighbours are $19/8$ and $21/8$. Thus $s_2 = |2 - 19/8| + |2 - 21/8| = 1$. Similarly $s_3 = |3 - 19/8| = 0.625$ and $s_4 = |4 - 17/8| = 1.825$.

Unlike Amadasun and King (1989), in our definition a valid neighbourhood is not necessarily completely inside the ROI, because complete neighbourhoods may not exist for distance δ inside an irregular ROI mask. Instead, a valid neighbourhood exists if there is at least one neighbouring voxel included in the ROI mask. Then, weight W is equal to the number of voxels in the neighbourhood that are part of the ROI mask and n_i is the total number of voxels with grey level i which have a valid neighbourhood.

Many NGTDM-based features depend on the N_g grey level probabilities $p_i = n_i/N_{v,c}$, where N_g is the number of discretised grey levels in the ROI intensity mask and $N_{v,c} = \sum n_i$ is total number of voxels that have at least one neighbour. If all voxels have at least one neighbour $N_{v,c} = N_v$. Furthermore, let $N_{g,p} \leq N_g$ be the number of discretised grey levels with $p_i > 0$. In the above example, $N_g = 4$ and $N_{g,p} = 3$.

Summarising features. Feature values are calculated after determining the NGTDM(s) for the ROI intensity mask. Three methods can be used to arrive at a single feature value for each volume. Five methods were previously defined for GLCM and GLRLM, but as the NGTDM is not directionally dependent, only three methods remain applicable. A schematic example was shown previously in Figure 4.3. One method involves merging NGTDMs by summing the neighbourhood grey tone difference s_i and the number of voxels with a valid neighbourhood n_i and grey level i for NGTDMs of the different slices. Features are subsequently calculated from the merged NGTDM. Note that when NGTDMs are merged, $N_{v,c}$ and p_i should be updated based on the merged NGTDM.

1	2	2	3
1	2	3	3
4	2	4	1
4	1	2	3

(a) Grey levels

	n_i	p_i	s_i
1	0	0.00	0.000
2	2	0.50	1.000
3	1	0.25	0.625
4	1	0.25	1.825

(b) Neighbourhood grey tone difference matrix

Table 4.9: Original image with grey levels (a) and corresponding neighbourhood grey tone difference matrix (NGTDM) (b). The $N_{v,c}$ pixels with valid neighbours at distance 1 are located within the rectangle in (a). The grey level voxel count n_i , the grey level probability $p_i = n_i/N_{v,c}$, and the neighbourhood grey level difference s_i for pixels with grey level i are included in the NGTDM. Note that our actual definition deviates from the original definition of Amadasun and King (1989), which is used here. In our definition complete neighbourhood are no longer required. In our definition the NGTDM would be calculated on the entire pixel area, and not solely on those pixels within the rectangle of panel (a).

4.10.1 Coarseness

Grey level differences in coarse textures are generally small due to large-scale patterns. Summing differences gives an indication of the level of the spatial rate of change in intensity (Amadasun and King, 1989). *Coarseness* is defined as:

$$F_{ngt.coarseness} = \frac{1}{\sum_{i=1}^{N_g} p_i s_i}$$

Because $\sum_{i=1}^{N_g} p_i s_i$ potentially evaluates to 0, the maximum *coarseness* value is set to an arbitrary number of 10^6 . Amadasun and King originally circumvented this issue by adding a unspecified small number ϵ to the denominator, but an explicit, though arbitrary, maximum value should allow for more consistency.

4.10.2 Contrast

Contrast depends on the dynamic range of the grey levels as well as the spatial frequency of intensity changes (Amadasun and King, 1989). Thus, *contrast* is defined as:

$$F_{ngt.contrast} = \left(\frac{1}{N_{g,p} (N_{g,p} - 1)} \sum_{i_1=1}^{N_g} \sum_{i_2=1}^{N_g} p_{i_1} p_{i_2} (i_1 - i_2)^2 \right) \left(\frac{1}{N_{v,c}} \sum_{i=1}^{N_g} s_i \right)$$

Grey level probabilities p_{i_1} and p_{i_2} are copies of p_i with different iterators, i.e. $p_{i_1} = p_{i_2}$ for $i_1 = i_2$. The first term considers the grey level dynamic range, whereas the second term is a measure for intensity changes within the volume. If $N_{g,p} = 1$, $F_{ngt.contrast} = 0$.

4.10.3 Busyness

Textures with large changes in grey levels between neighbouring voxels are said to be busy (Amadasun and King, 1989). *Busyness* was defined as:

$$F_{ngt.busyness} = \frac{\sum_{i=1}^{N_g} p_i s_i}{\sum_{i_1=1}^{N_g} \sum_{i_2=1}^{N_g} i_1 p_{i_1} - i_2 p_{i_2}}, \quad p_{i_1} \neq 0 \text{ and } p_{i_2} \neq 0$$

As before, $p_{i_1} = p_{i_2}$ for $i_1 = i_2$. The original definition was erroneously formulated as the denominator will always evaluate to 0. Therefore we use a slightly different definition (Hatt et al., 2017):

$$F_{ngt.busyness} = \frac{\sum_{i=1}^{N_g} p_i s_i}{\sum_{i_1=1}^{N_g} \sum_{i_2=1}^{N_g} |i_1 p_{i_1} - i_2 p_{i_2}|}, \quad p_{i_1} \neq 0 \text{ and } p_{i_2} \neq 0$$

If $N_{g,p} = 1$, $F_{ngt.busyness} = 0$.

4.10.4 Complexity

Complex textures are non-uniform and rapid changes in grey levels are common (Amadasun and King, 1989). Texture *complexity* is defined as:

$$F_{ntg.complexity} = \frac{1}{N_{v,c}} \sum_{i_1=1}^{N_g} \sum_{i_2=1}^{N_g} |i_1 - i_2| \frac{p_{i_1} s_{i_1} + p_{i_2} s_{i_2}}{p_{i_1} + p_{i_2}}, \quad p_{i_1} \neq 0 \text{ and } p_{i_2} \neq 0$$

As before, $p_{i_1} = p_{i_2}$ for $i_1 = i_2$, and likewise $s_{i_1} = s_{i_2}$ for $i_1 = i_2$.

4.10.5 Strength

Amadasun and King (1989) defined texture *strength* as:

$$F_{ngt.strength} = \frac{\sum_{i_1=1}^{N_g} \sum_{i_2=1}^{N_g} (p_{i_1} + p_{i_2}) (i_1 - i_2)^2}{\sum_{i=1}^{N_g} s_i}, \quad p_{i_1} \neq 0 \text{ and } p_{i_2} \neq 0$$

As before, $p_{i_1} = p_{i_2}$ for $i_1 = i_2$. If $\sum_{i=1}^{N_g} s_i = 0$, $F_{ngt.strength} = 0$.

4.11 Texture features - Neighbouring grey level dependence based features

Sun and Wee (1983) defined the neighbouring grey level dependence matrix (NGLDM) as an alternative to the grey level co-occurrence matrix. The NGLDM aims to capture the coarseness of the overall texture and is rotationally invariant.

NGLDM also works with concept of a neighbourhood around a central voxel. All voxels within (*Chebyshev*) distance δ are considered to belong to the neighbourhood of the center voxel. The discretised grey levels of the center voxel k and a neighbouring voxel m ($m \neq k$) are said to be dependent if $|X_{d,k} - X_{d,m}| \leq \alpha$, with α being a non-negative integer coarseness parameter. The number of grey level dependent voxels j within the neighbourhood is then counted as:

$$j_k = 1 + \sum_m^{N_m} [|X_{d,k} - X_{d,m}| \leq \alpha]$$

Here, $[\dots]$ is an Iverson bracket, which is 1 if the aforementioned condition is fulfilled, and 0 otherwise. N_m is the number of voxels within the neighbourhood. Note that the minimum dependence $j_k = 1$ and not $j_k = 0$. This is done because some feature definitions require a minimum dependence of 1 or are undefined otherwise. One may therefore also write j_k as:

$$j_k = \sum_m^{N_{m,c}} [|X_{d,k} - X_{d,m}| \leq \alpha]$$

Here $N_{m,c}$ is the neighbourhood including the center.

Dependence j_k is iteratively determined for each voxel k in the ROI intensity mask. M is then the $N_g \times N_n$ neighbouring grey level dependence matrix, where N_g is the number of discretised grey levels present in the ROI intensity mask and $N_n = \max(j_k)$ the maximum grey level dependence count found. Element s_{ij} of M is then the number of neighbourhoods with a center voxel with discretised grey level i and a neighbouring voxel dependence j . Furthermore, let N_v be the number of voxels in the ROI intensity mask, and $N_s = \sum_{i=1}^{N_g} \sum_{j=1}^{N_n} s_{ij}$ the number of neighbourhoods. Marginal sums can likewise be defined. Let $s_{i.} = \sum_{j=1}^{N_n} s_{ij}$ be the number of neighbourhoods with discretised grey level i , and let $s_{.j} = \sum_{i=1}^{N_g} s_{ij}$ be the number of neighbourhoods with dependence j , regardless of grey level. A two dimensional example is shown in Table 4.10.

The definition we use deviates from the original by Sun and Wee (1983). Because regions of interest are rarely cuboid, omission of neighbourhoods which contain voxels outside the ROI mask may lead to inconsistent results, especially for larger distance δ . Hence the neighbourhoods of all voxels in the within the ROI intensity mask are considered, and consequently $N_v = N_s$. Neighbourhood voxels located outside the ROI do not add to dependence j . Thus, small and tortuous ROI will be considered coarser as neighbouring grey level dependence j is low.

Note that while $\alpha = 0$ is a typical choice for the coarseness parameter, different α are possible. Likewise, a typical choice for neighbourhood radius δ is Chebyshev distance $\delta = 1$, which is effectively the same as Euclidean distance $\delta = \sqrt{3}$, but larger values may be useful as well.

Summarising features. Feature values are calculated after determining the GLDZM(s) for the ROI intensity mask. Three methods can be used to arrive at a single feature value

for each volume. Five methods were previously defined for GLCM and GLRLM, but as the GLDZM is not directionally dependent, only three methods remain applicable. A schematic example was shown previously in Figure 4.3. One method involves merging GLDZMs by summing the number of zones d_{ij} over the GLDZM for the different slices. Features are subsequently calculated from the merged GLDZM. Note that when GLDZMs are merged, N_v should likewise be summed to retain consistency.

Note on feature references. The NGLDM is structured similarly to the GLRLM, GLSZM and GLDZM. NGLDM feature definitions are therefore based on the definitions of GLRLM features, and references may be found in Section 4.7, except for the features originally defined by Sun and Wee (1983).

Summarising features. Feature values are calculated after determining the NGLDM(s) for the ROI intensity mask. Three methods can be used to arrive at a single feature value for each volume. Five methods were previously defined for GLCM and GLRLM, but as the NGLDM is not directionally dependent, only three methods remain applicable. A schematic example was shown previously in Figure 4.3. One method involves merging NGLDMs by summing the dependence count s_{ij} by element over the NGLDM of the different slices. Features are subsequently calculated from the merged NGLDM. Note that when NGLDMs are merged, N_v and N_s should likewise be summed to retain consistency.

				dependence k			
				0	1	2	3
1	2	2	3	1	0	0	0
1	2	3	3	2	0	0	1
4	2	4	1	3	0	0	1
4	1	2	3	4	1	0	0

(a) Grey levels

(b) Neighbouring grey level dependence matrix

Table 4.10: Original image with grey levels and pixels with a complete neighbourhood within the square (a); corresponding neighbouring grey level dependence matrix for distance $d = \sqrt{2}$ and coarseness parameter $a = 0$ (b). Element $s(i, j)$ of the NGLDM indicates the number of neighbourhoods with a center pixel with grey level i and neighbouring grey level dependence k within the image. Note that in our definition a complete neighbourhood is no longer required. Thus every voxel is considered as a center voxel with a neighbourhood, instead of being constrained to the voxels within the square in panel (a).

4.11.1 Low dependence emphasis

This feature emphasises low neighbouring grey level dependence counts. Sun and Wee (1983) refer to this feature as *small number emphasis*. It is defined as:

$$F_{ngl.lde} = \frac{1}{N_s} \sum_{j=1}^{N_n} \frac{s_{.j}}{j^2}$$

4.11.2 High dependence emphasis

This feature emphasises high neighbouring grey level dependence counts. Sun and Wee (1983) refer to this feature as *large number emphasis*. It is defined as:

$$F_{n\text{gl.hde}} = \frac{1}{N_s} \sum_{j=1}^{N_n} j^2 s_{.j}$$

4.11.3 Low grey level count emphasis

This feature is a grey level analogue to *lowdependenceemphasis*. Instead of low neighbouring grey level dependence counts, low grey levels are emphasised. The feature is defined as:

$$F_{n\text{gl.lgce}} = \frac{1}{N_s} \sum_{i=1}^{N_g} \frac{s_i}{i^2}$$

4.11.4 High grey level count emphasis

The *high grey level count emphasis* feature is a grey level analogue to *high dependence emphasis*. The feature emphasises high grey levels, and is defined as:

$$F_{n\text{gl.hgce}} = \frac{1}{N_s} \sum_{i=1}^{N_g} i^2 s_i$$

4.11.5 Low dependence low grey level emphasis

This feature emphasises neighbouring grey level dependence counts in the upper left quadrant of the NGLDM, where low dependence counts and low grey levels are located. It is defined as:

$$F_{n\text{gl.ldlge}} = \frac{1}{N_s} \sum_{i=1}^{N_g} \sum_{j=1}^{N_n} \frac{s_{ij}}{i^2 j^2}$$

4.11.6 Low dependence high grey level emphasis

This feature emphasises neighbouring grey level dependence counts in the lower left quadrant of the NGLDM, where low dependence counts and high grey levels are located. The feature is defined as:

$$F_{n\text{gl.ldhge}} = \frac{1}{N_s} \sum_{i=1}^{N_g} \sum_{j=1}^{N_n} \frac{i^2 s_{ij}}{j^2}$$

4.11.7 High dependence low grey level emphasis

This feature emphasises neighbouring grey level dependence counts in the upper right quadrant of the NGLDM, where high dependence counts and low grey levels are located. The feature is defined as:

$$F_{n\text{gl.hdlge}} = \frac{1}{N_s} \sum_{i=1}^{N_g} \sum_{j=1}^{N_n} \frac{j^2 s_{ij}}{i^2}$$

4.11.8 High dependence high grey level emphasis

The *high dependence high grey level emphasis* feature emphasises neighbouring grey level dependence counts in the lower right quadrant of the NGLDM, where high dependence counts and high grey levels are located. The feature is defined as:

$$F_{ngl.hdhge} = \frac{1}{N_s} \sum_{i=1}^{N_g} \sum_{j=1}^{N_n} i^2 j^2 s_{ij}$$

4.11.9 Grey level non-uniformity

Grey level non-uniformity assesses the distribution of neighbouring grey level dependence counts over the grey values. The feature value is low when dependence counts are equally distributed along grey levels. The feature is defined as:

$$F_{ngl.glnu} = \frac{1}{N_s} \sum_{i=1}^{N_g} s_i^2$$

4.11.10 Grey level non-uniformity normalised

This is a normalised version of the *grey level non-uniformity* feature. It is defined as:

$$F_{ngl.glnu.norm} = \frac{1}{N_s^2} \sum_{i=1}^{N_g} s_i^2$$

When calculating *grey level non-uniformity normalised* using a single 3D NGLDM matrix, it is equivalent to the *intensity histogram uniformity* feature (van Griethuysen et al., 2017).

4.11.11 Dependence count non-uniformity

This features assesses the distribution of neighbouring grey level dependence counts over the different dependence counts. The feature value is low when dependence counts are equally distributed. Sun and Wee (1983) refer to this feature as *number non-uniformity*. It is defined as:

$$F_{ngl.dcnu} = \frac{1}{N_s} \sum_{j=1}^{N_n} s_{.j}^2$$

4.11.12 Dependence count non-uniformity normalised

This is a normalised version of the *dependence count non-uniformity* feature. It is defined as:

$$F_{ngl.dcnu.norm} = \frac{1}{N_s^2} \sum_{j=1}^{N_n} s_{.j}^2$$

4.11.13 Dependence count percentage

This feature assesses the fraction of the number of realised neighbourhoods and the maximum number of potential neighbourhoods. *Dependence count percentage* may be completely omitted as it evaluates to 1 when complete neighbourhoods are not required, as is the case under our definition. It is defined as:

$$F_{ngl.dc.perc} = \frac{N_s}{N_v}$$

4.11.14 Grey level variance

This feature estimates the variance in dependence counts for the grey levels. Let $p_{ij} = s_{ij}/N_s$ be the joint probability estimate for finding discretised grey level i with dependence j . The feature is then defined as:

$$F_{ngl.gl.var} = \sum_{i=1}^{N_g} \sum_{j=1}^{N_n} (i - \mu)^2 p_{ij}$$

Here, $\mu = \sum_{i=1}^{N_g} \sum_{j=1}^{N_n} i p_{ij}$.

4.11.15 Dependence count variance

This feature estimates the variance in dependence counts for the different possible dependence counts. As before let $p_{ij} = s_{ij}/N_s$. The feature is defined as:

$$F_{ngl.dc.var} = \sum_{i=1}^{N_g} \sum_{j=1}^{N_n} (j - \mu)^2 p_{ij}$$

Mean dependence count is defined as $\mu = \sum_{i=1}^{N_g} \sum_{j=1}^{N_n} j p_{ij}$.

4.11.16 Dependence count entropy

This feature is referred to as *entropy* by Sun and Wee (1983). Let $p_{ij} = s_{ij}/N_s$. *Dependence count entropy* is then defined as:

$$F_{ngl.dc.entr} = - \sum_{i=1}^{N_g} \sum_{j=1}^{N_n} p_{ij} \log_2 p_{ij}$$

This definition remedies an error in the definition of Sun and Wee (1983), where the term within the logarithm is dependence count s_{ij} instead of count probability p_{ij} .

4.11.17 Dependence count energy

This feature is called *second moment* by Sun and Wee (1983). Let $p_{ij} = s_{ij}/N_s$. Then *dependence count energy* is defined as:

$$F_{ngl.dc.energy} = \sum_{i=1}^{N_g} \sum_{j=1}^{N_n} p_{ij}^2$$

This definition also remedies an error in the original definition, where squared dependence count s_{ij}^2 is divided by N_s only, thus leaving a major volume dependency. In the definition given here, s_{ij}^2 is normalised by N_s^2 through the use of count probability p_{ij} .

Chapter 5

Novel and uncommon imaging features

Several improvements to existing methods, and less commonly used image feature methods are described in this section.

5.1 Texture features - Distance weighted texture matrices

Changes to grey level co-occurrence, run length and neighbourhood grey tone difference matrices were suggested by Vallières et al. (2015). The contents of these matrices can be updated based on the distance between center voxels and reference voxels (GLCM, NGTDM) and the length of runs. Different definitions of distance exist and can be used. Let $\mathbf{m} = (m_x, m_y, m_z)$ be the vector from a center voxel at $\mathbf{k} = (k_x, k_y, k_z)$ to a neighbour voxel at $\mathbf{k} + \mathbf{m}$. For GLCM and GLRLM $\mathbf{m} = \mathbf{x}$ is the direction vector. Depending on definition of the norm, distance is defined as:

- ℓ_1 norm or *Manhattan* norm:

$$\delta_1 = |m_x| + |m_y| + |m_z|$$

- ℓ_2 norm or *Euclidian* norm:

$$\delta_2 = \sqrt{m_x^2 + m_y^2 + m_z^2}$$

- ℓ_∞ norm or *Chebyshev* norm:

$$\delta_\infty = \max(|m_x|, |m_y|, |m_z|)$$

Weighting factors may be defined to either correct distance or emphasise local textures: $w(\delta(\mathbf{m}))$. For conventional texture matrices $w = 1$.

Grey level co-occurrence matrix Correcting the GLCM for distance takes place by weighting each GLCM with distance $\delta(\mathbf{m})$ using e.g. the Euclidian or Manhattan norm. Using the Chebyshev norm conforms to the original definition and has no effect. Local

textures may furthermore be emphasised using an inverse distance function to weight each GLCM, e.g. $w = \delta^{-1}$ or $\exp(-\delta^2)$ (van Griethuysen et al., 2017).

Weighting the GLCM is only meaningful if, after weighting, GLCM matrices for all directions are merged into a single GLCM before feature calculation.

Grey level run length matrix The correction to the GLRLM matrix consists of replacing the run length by the actual distance, i.e. run length $j^* = \delta(\mathbf{m})j$. As with GLCM, using the Chebyshev norm for distances reverts to the original definition for GLRLM. Weighting is only meaningful if, after weighting, GLRLM matrices for all directions are merged before feature calculation.

Neighbourhood grey tone difference matrix The neighbourhood grey tone difference may be corrected for distance or locally emphasised. The calculation for the average grey level in the neighbourhood centred at \mathbf{j} may be updated:

$$\bar{X}_k = \frac{1}{W} \sum_{m_z=-\delta}^{\delta} \sum_{m_y=-\delta}^{\delta} \sum_{m_x=-\delta}^{\delta} w(\delta(\mathbf{m}))X_d(\mathbf{k} + \mathbf{m})$$

$$(\mathbf{m}) \neq (0, 0, 0)$$

Here $W = \sum_{m_z} \sum_{m_y} \sum_{m_x} w(\delta(\mathbf{m}))$. For $w = 1$, the NGTDM reverts to its original.

5.2 Texture features - Neighbourhood grey level co-occurrence matrix

The GLCM is defined along specific directions. The neighbourhood grey level co-occurrence matrix (NGLCM) is a modification which considers the neighbourhood of a voxel to consist of all voxels within distance δ . The remaining calculations are performed as for the conventional GLCM, see Section 4.6.

5.3 Texture features - Extended emphasis features

The *emphasis*-type features in the GLRLM, GLSZM, GLDZM and NGLDM-based feature sets put a particular emphasis on part of the respective matrices. They do so using a combination of squared indices. Such behaviour can be further generalised by using indices with different powers (van Dijk et al., 2017). For example, the *long run high grey level emphasis* feature is defined as:

$$F_{rlm.lrhge} = \frac{1}{N_s} \sum_{i=1}^{N_g} \sum_{j=1}^{N_r} i^2 j^2 r_{ij}$$

Emphases are changed by adjusting powers of the indices i and j . For example, $\frac{1}{N_s} \sum_{i=1}^{N_g} \sum_{j=1}^{N_r} i^3 j r_{ij}$ and $\frac{1}{N_s} \sum_{i=1}^{N_g} \sum_{j=1}^{N_r} i j^3 r_{ij}$ constitute new features with a different emphasis on run lengths and grey levels. We can therefore generate a large number of features by changing powers.

Nomenclature Many emphasis features will not have existing names. What is proposed therefore is to encode the respective powers in the name as *emphasis*(power of index i , power of index j). This naming scheme, when applied to grey level run length matrix-based features leads to, e.g. *emphasis*(2,2) for *long run high grey level emphasis*, *emphasis* (0,-2) for *short runs emphasis* and *emphasis* (-2,2) for *long run low grey level emphasis*.

Chapter 6

Reporting guidelines

Reliable reporting is necessary to ensure reproducibility and validation of results. To help provide a complete report on image processing and image biomarker extraction, we present the guidelines below. These guidelines are partially based on the work by Sollini et al. (2017), and otherwise derived from the image processing and feature calculation steps provided within this document.

General	
imaging acquisition	Describe which imaging was acquired from the scanner, e.g. CT.
reconstruction	Describe image acquisition details, i.e. scanner vendor, method of image acquisition (e.g. dynamic, contrast-enhanced), and imaging parameters (e.g. MR TE times, CT tube voltage and current).
approach	Describe how images were reconstructed from the acquired image, e.g. (iterative) reconstruction kernels and voxel dimensions.
process structure	Describe whether the image volume is analysed by slice (2D), or as a volume (3D).
software	Describe the sequence of image processing steps used for the analysis, preferably schematically.
data availability	Describe which software was used to perform image processing and feature extraction.
	Describe whether and where (imaging) data, ROIs and software code is made available.
Data conversion	
procedure	Describe how data was converted from reconstructed image data, e.g. by calculation of standard uptake values for PET. References to algorithms should be provided, or otherwise described in detail.
Image post-acquisition processing	
procedure	Describe post-processing steps and parameters, e.g. noise correction in MRI and partial volume effect corrections in PET. References to algorithms should be provided, or otherwise described in detail.

continued on next page

Segmentation	
ROI procedure	Describe which regions of interest were delineated and used for analysis. Describe how regions of interest were delineated in the image. Specify which algorithms and settings were used. References to algorithms should be provided, or otherwise described in detail.
Interpolation	
voxel dimensions	Specify original and interpolated voxel dimensions.
image interpolation method	Specify interpolation method used, e.g. <i>trilinear interpolation</i> . Specify how original and interpolation grids were aligned.
image intensity rounding	Specify rounding procedures for non-integer interpolated grey levels (if applicable).
ROI interpolation method	Specify interpolation method used to interpolate ROI morphological and intensity masks.
ROI partial volume	Specify minimum partial volume fraction required to include an interpolated ROI mask voxel in the interpolated ROI (if applicable).
Re-segmentation	
ROI mask criteria	Specify which criteria were used to include or exclude voxels from a ROI mask (if applicable).
Discretisation	
discretisation method	Specify which method is being used for discretising image intensities. References to the method should be provided, or otherwise described in detail.
discretisation parameters	Specify discretisation parameters for discretisation, e.g. number of bins.
Feature calculation	
feature set	Report which features were calculated. References to feature definitions should be provided, or otherwise described in detail.
feature parameters	Describe specific settings used for feature calculation, e.g. the distance setting and matrix merging method for the grey level co-occurrence matrix.
standardisation	State whether image processing and feature calculation were tested on the digital phantom and patient test data. State whether the feature values calculated match the benchmark values; otherwise state which ones do not match benchmark values, and indicate why.

Table 6.1: Guidelines for reporting on image biomarker extraction.

Chapter 7

Benchmarking data sets

Image features and image processing were benchmarked using a digital image phantom and the CT image of a lung cancer patient, which are described below.

7.1 Digital phantom

A digital phantom was developed to compare image features. The phantom is shown in Figure 7.1. The phantom has the following characteristics:

- The phantom consists of $5 \times 4 \times 4$ (x, y, z) voxels.
- Voxels are $2.0 \times 2.0 \times 2.0$ mm in size.
- Not all voxels are included in the region of interest (ROI). Aside from several excluded voxels on the outside, also an internal voxel was excluded. Voxels excluded from the ROI are shown in blue.
- Some grey level intensities are not present in the test volume. Notably grey levels 2 and 5 are absent.
- A slice consists of the voxels in (x, y) plane for a particular slice at position z . Therefore slices are stacked in the z direction.

7.1.1 Calculating image features

The digital phantom does not require the additional image processing that conventional images would normally require, and feature calculation is done directly on the phantom itself. The following should be taken into account for calculating image features:

- As image processing is not required, therefore discretisation is unnecessary. All features are to be calculated using the phantom as it is. Alternatively, one could use a *fixed bin size* discretisation of 1 or *fixed bin number* discretisation of 6 bins, which does not alter the contents of the phantom.
- Grey level co-occurrence matrices are symmetrical and calculated for (Chebyshev) distance $\delta = 1$.

- Neighbouring grey level dependence and neighbourhood grey tone difference matrices are likewise calculated for (Chebyshev) distance $\delta = 1$. Additionally, the neighbouring grey level dependence coarseness parameter $\alpha = 0$.
- Because discretisation is lacking, most intensity-based statistical features will match their intensity histogram-based analogues in value.
- The ROI morphological and intensity masks are identical for the digital phantom, due to lack of re-segmentation.

7.2 Patient data

A small dataset of CT images from four non-small-cell lung carcinoma patients was made publicly available to serve as radiomics validation phantoms (DOI:10.17195/candat.2016.08.1). We use the first of these patients (PAT1) to provide benchmarks for different image processing steps.

The images are stored as a stack of slices in DICOM format. The image slices can be identified by the DCM_IMG prefix. The gross tumour volume (GTV) was contoured and is used as region of interest (ROI). Contour information is stored as an RT structure set in the DICOM file starting with DCM_RS.

We define five cases, spanning a number of different image processing steps. These cases are defined in Table 7.1. While most settings are self-explanatory, there are several aspects that require some attention. Cases are divided in 2D and 3D approaches. For the 2D cases, image interpolation is conducted within the slice, and likewise texture features are extracted from the in-slice plane, and not volumetrically (3D). For the 3D cases interpolation is conducted in three dimensions, and features are likewise extracted volumetrically. Discretisation is moreover required for texture, intensity histogram and intensity-volume histogram features.

7.2.1 Notes on interpolation

Interpolation has a major influence on feature values. Different algorithm implementations of the same interpolation method may ostensibly provide the same functionality, but lead to different interpolation grids. It is therefore recommended to read the documentation of the particular implementation to assess if the implementation allows or implements the following guidelines:

- The spatial origin of the original grid in world coordinates matches the DICOM origin by definition.
- The size of the interpolation grid is determined by rounding the fractional grid size towards infinity, i.e. a ceiling operation. This prevents the interpolation grid from disappearing for very small images, but is otherwise an arbitrary choice.
- The centers of the interpolation and original image grids should be identical, i.e. the interpolation grid is centered on the center of the original image grid. This prevents spacing inconsistencies in the interpolation grid and avoids potential indexing issues.

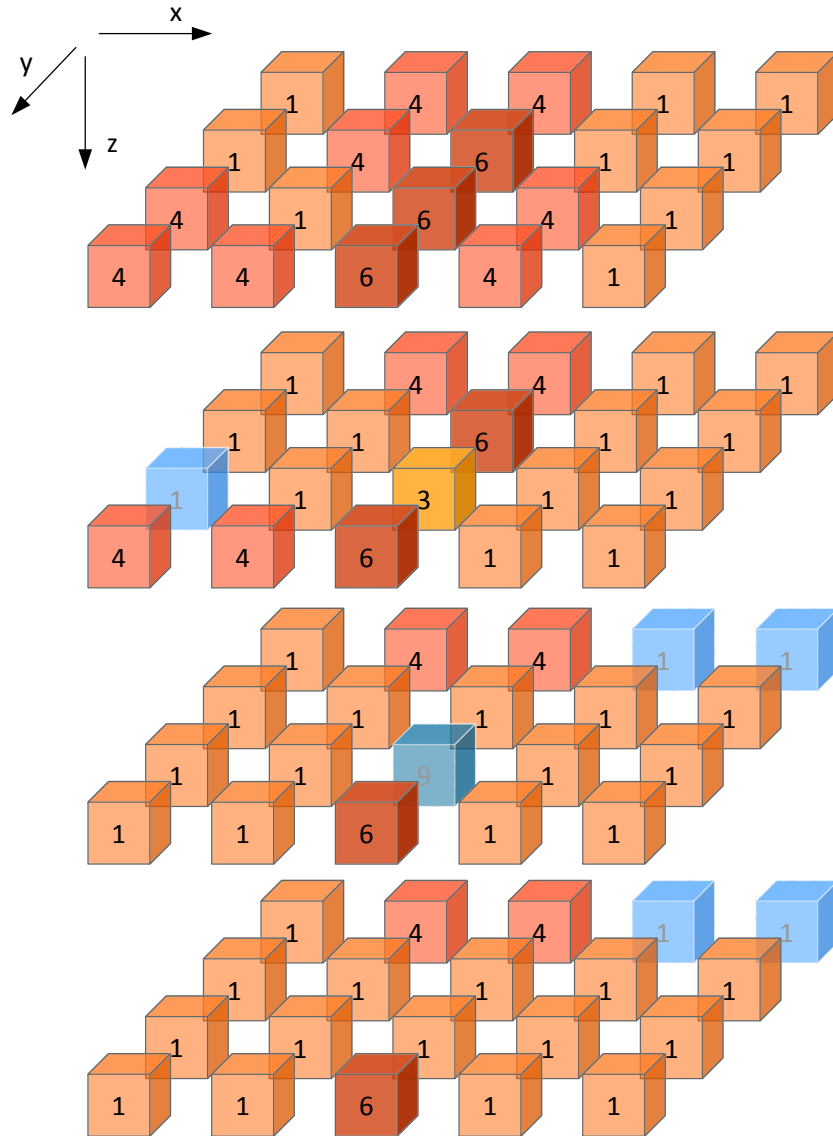


Figure 7.1: Exploded view of the test volume. The number in each voxel corresponds with its grey level. Blue voxels are excluded from the region of interest. The coordinate system is so that x increases from left to right, y increases from back to front and z increases from top to bottom, as is indicated by the axis definition in the top-left.

- The extent of the interpolation grid is, by definition, always equal or larger than that of the original grid. This means that at the edges, values are extrapolated. To facilitate this process, the image should be sufficiently padded with voxels taking on the nearest border value.
- Floating point representation of the image and the ROI masks affect interpolation precision, and consequentially feature values. Image and ROI masks should at least be represented at full precision (32-bit) to avoid rounding errors. One example is the unintended exclusion of voxels from the interpolated ROI mask, which occurs when interpolation yields 0.4999... instead of 0.5. When images and ROI masks are converted from lower precision (e.g. 16-bit), they may require rounding if the original data are integer, such as Hounsfield Units.

More details are provided in Section 3.4.

7.2.2 Diagnostic features

Identifying issues with an implementation of the image processing sequence may be challenging. Multiple steps follow one another and differences propagate. Hence we define a small number of diagnostic features that describe how the image and ROI masks change with each image processing step.

Initial image stack. The following features may be used to describe the initial image stack (i.e. after loading image data for processing):

- *Image dimensions.* This describes the image dimensions in voxels along the different image axes.
- *Voxel dimensions.* This describes the voxel dimensions in mm. The dimension along the z-axis is equal to the distance between the origin voxels of two adjacent slices, and is generally equal to the slice thickness.
- *Mean intensity.* This is the average intensity within the entire image.
- *Minimum intensity.* This is the lowest intensity within the entire image.
- *Maximum intensity.* This is the highest intensity within the entire image.

Interpolated image stack. The above features may also be used to describe the image stack after image interpolation.

Initial region of interest. The following descriptors are used to describe the region of interest (ROI) directly after segmentation of the image:

- *ROI intensity mask dimensions.* This describes the dimensions, in voxels, of the ROI intensity mask.
- *ROI intensity mask bounding box dimensions.* This describes the dimensions, in voxels, of the bounding box of the ROI intensity mask.
- *ROI morphological mask bounding box dimensions.* This describes the dimensions, in voxels, of the bounding box of the ROI morphological mask.

- *Number of voxels in the ROI intensity mask.* This describes the number of voxels included in the ROI intensity mask.
- *Number of voxels in the ROI morphological mask.* This describes the number of voxels included in the ROI intensity mask.
- *Mean ROI intensity.* This is the mean intensity of image voxels within the ROI intensity mask.
- *Minimum ROI intensity.* This is the lowest intensity of image voxels within the ROI intensity mask.
- *Maximum ROI intensity.* This is the highest intensity of image voxels within the ROI intensity mask.

Interpolated region of interest. The same features can be used to describe the ROI after interpolation of the ROI mask.

Re-segmented region of interest. Again, the same features as above can be used to describe the ROI after resegmentation.

7.2.3 Calculating image features

Unlike the digital phantom does require additional image processing, which is done using the settings in Table 7.1. The following should be taken into account for calculating image features for the patient cases:

- Grey level co-occurrence matrices are symmetrical and calculated for (Chebyshev) distance $\delta = 1$.
- Neighbouring grey level dependence and neighbourhood grey tone difference matrices are likewise calculated for (Chebyshev) distance $\delta = 1$. Additionally, the neighbouring grey level dependence coarseness parameter $\alpha = 0$.
- Intensity-based statistical features and their intensity histogram-based analogues will differ in value due to discretisation, in contrast to the same features for the digital phantom.
- The ROI morphological and intensity masks are different for all the patient cases, due to re-segmentation.
- Calculation of IVH feature: since by default CT contains definite and discrete intensities, no separate discretisation prior to the calculation of intensity-volume histogram features is required, as intended in cases 1, 2 and 4 (i.e. ‘definite intensity units – discrete case’). For cases 3 and 5, we re-discretise the ROI intensities prior to calculation of intensity-volume histogram features to further test our algorithms. Case 3 would simulate the ‘definite intensity units – continuous case’, and case 5 the ‘arbitrary intensity units’ case (re-segmentation range not to be used). For details, please consult section 4.5.

	Case 1	Case 2	Case 3	Case 4	Case 5
Patient	PAT1	PAT1	PAT1	PAT1	PAT1
ROI	GTV-1	GTV-1	GTV-1	GTV-1	GTV-1
Approach	2D	2D	3D	3D	3D
Interpolation	no	yes	yes	yes	yes
Voxel dimension (mm)		2×2	$2 \times 2 \times 2$	$2 \times 2 \times 2$	$2 \times 2 \times 2$
Interpolation method		bilinear	trilinear	trilinear	tricubic spline
Grey level rounding		nearest integer	nearest integer	nearest integer	nearest integer
ROI interp. method		bilinear	trilinear	trilinear	trilinear
ROI partial volume		0.5	0.5	0.5	0.5
Re-segmentation					
Range (HU)	$[-500, 400]$	$[-500, 400]$	$[-1000, 400]$	no	$[-500, 400]$
Outliers	no	no	no	3σ	3σ
Discretisation					
Texture and IH	FBS: 25 HU	FBN: 32 bins	FBS: 25 HU	FBN: 32 bins	FBN: 32 bins
IVH	no	no	FBS: 2.5 HU	no	FBN: 1000 bins

Table 7.1: Image processing steps and settings for different cases. For details, refer to the corresponding sections in chapter 3. ROI: region of interest; HU: Hounsfield Unit; IH: intensity histogram; FBS: fixed bin size; FBN: fixed bin number; IVH: intensity-volume histogram; NA: not applicable.

Bibliography

- Aerts, H. J. W. L., Rios-Velazquez, E., Leijenaar, R. T. H., Parmar, C., Grossmann, P., Cavalho, S., Bussink, J., Monshouwer, R., Haibe-Kains, B., Rietveld, D., Hoebers, F. J. P., Rietbergen, M. M., Leemans, C. R., Dekker, A., Quackenbush, J., Gillies, R. J., and Lambin, P. (2014). Decoding tumour phenotype by noninvasive imaging using a quantitative radiomics approach. *Nature communications*, 5:4006.
- Ahipaolu, S. D. (2015). Fast algorithms for the minimum volume estimator. *Journal of Global Optimization*, 62(2):351–370.
- Albregtsen, F., Nielsen, B., and Danielsen, H. (2000). Adaptive gray level run length features from class distance matrices. In *Proceedings 15th International Conference on Pattern Recognition. ICPR-2000*, volume 3, pages 738–741. IEEE Comput. Soc.
- Amadasun, M. and King, R. (1989). Textural features corresponding to textural properties. *IEEE Transactions on Systems, Man and Cybernetics*, 19(5):1264–1273.
- Apostolova, I., Steffen, I. G., Wedel, F., Lougovski, A., Marnitz, S., Derlin, T., Amthauer, H., Buchert, R., Hofheinz, F., and Brenner, W. (2014). Asphericity of pretherapeutic tumour FDG uptake provides independent prognostic value in head-and-neck cancer. *European radiology*, 24(9):2077–87.
- Barequet, G. and Har-Peled, S. (2001). Efficiently Approximating the Minimum-Volume Bounding Box of a Point Set in Three Dimensions. *Journal of Algorithms*, 38(1):91–109.
- Boellaard, R., Delgado-Bolton, R., Oyen, W. J. G., Giammarile, F., Tatsch, K., Eschner, W., Verzijlbergen, F. J., Barrington, S. F., Pike, L. C., Weber, W. A., Stroobants, S. G., Delbeke, D., Donohoe, K. J., Holbrook, S., Graham, M. M., Testanera, G., Hoekstra, O. S., Zijlstra, J. M., Visser, E. P., Hoekstra, C. J., Pruim, J., Willemsen, A. T., Arends, B., Kotzerke, J., Bockisch, A., Beyer, T., Chiti, A., and Krause, B. J. (2015). FDG PET/CT: EANM procedure guidelines for tumour imaging: version 2.0. *European journal of nuclear medicine and molecular imaging*, 42(2):328–54.
- Boellaard, R., O’Doherty, M. J., Weber, W. A., Mottaghy, F. M., Lonsdale, M. N., Stroobants, S. G., Oyen, W. J. G., Kotzerke, J., Hoekstra, O. S., Pruim, J., Marsden, P. K., Tatsch, K., Hoekstra, C. J., Visser, E. P., Arends, B., Verzijlbergen, F. J., Zijlstra, J. M., Comans, E. F. I., Lammertsma, A. A., Paans, A. M., Willemsen, A. T., Beyer, T., Bockisch, A., Schaefer-Prokop, C., Delbeke, D., Baum, R. P., Chiti, A., and Krause, B. J. (2010). FDG PET and PET/CT: EANM procedure guidelines for tumour PET imaging: version 1.0. *European Journal of Nuclear Medicine and Molecular Imaging*, 37(1):181–200.

- Boussion, N., Le Rest, C. C., Hatt, M., and Visvikis, D. (2009). Incorporation of wavelet-based denoising in iterative deconvolution for partial volume correction in whole-body PET imaging. *European journal of nuclear medicine and molecular imaging*, 36(7):1064–75.
- Chan, C. and Tan, S. (2001). Determination of the minimum bounding box of an arbitrary solid: an iterative approach. *Computers and Structures*, 79(15):1433–1449.
- Chu, A., Sehgal, C. M., and Greenleaf, J. F. (1990). Use of gray value distribution of run lengths for texture analysis. *Pattern Recognition Letters*, 11(6):415–419.
- Clausi, D. A. (2002). An analysis of co-occurrence texture statistics as a function of grey level quantization. *Canadian Journal of Remote Sensing*, 28(1):45–62.
- Collewet, G., Strzelecki, M., and Mariette, F. (2004). Influence of MRI acquisition protocols and image intensity normalization methods on texture classification. *Magnetic resonance imaging*, 22(1):81–91.
- Da Silva, E. C., Silva, A. C., De Paiva, A. C., and Nunes, R. A. (2008). Diagnosis of lung nodule using Moran’s index and Geary’s coefficient in computerized tomography images. *Pattern Analysis and Applications*, 11(1):89–99.
- Dale, M. R. T., Dixon, P., Fortin, M.-J., Legendre, P., Myers, D. E., and Rosenberg, M. S. (2002). Conceptual and mathematical relationships among methods for spatial analysis. *Ecography*, 25(5):558–577.
- Dasarathy, B. V. and Holder, E. B. (1991). Image characterizations based on joint gray levelrun length distributions. *Pattern Recognition Letters*, 12(8):497–502.
- Depeursinge, A. and Fageot, J. (2017). Biomedical Texture Operators and Aggregation Functions. In Depeursinge, A., Fageot, J., and Al-Kadi, O., editors, *Biomedical texture analysis*, chapter 3, pages 63–101. Academic Press, London, UK, 1st edition.
- Depeursinge, A., Foncubierta-Rodriguez, A., Van De Ville, D., and Müller, H. (2014). Three-dimensional solid texture analysis in biomedical imaging: review and opportunities. *Medical image analysis*, 18(1):176–96.
- El Naqa, I., Grigsby, P. W., Apte, A., Kidd, E., Donnelly, E., Khullar, D., Chaudhari, S., Yang, D., Schmitt, M., Laforest, R., Thorstad, W. L., and Deasy, J. O. (2009). Exploring feature-based approaches in PET images for predicting cancer treatment outcomes. *Pattern recognition*, 42(6):1162–1171.
- Frings, V., van Velden, F. H. P., Velasquez, L. M., Hayes, W., van de Ven, P. M., Hoekstra, O. S., and Boellaard, R. (2014). Repeatability of metabolically active tumor volume measurements with FDG PET/CT in advanced gastrointestinal malignancies: a multicenter study. *Radiology*, 273(2):539–48.
- Galloway, M. M. (1975). Texture analysis using gray level run lengths. *Computer Graphics and Image Processing*, 4(2):172–179.
- Geary, R. C. (1954). The Contiguity Ratio and Statistical Mapping. *The Incorporated Statistician*, 5(3):115–145.
- Gillies, R. J., Kinahan, P. E., and Hricak, H. (2015). Radiomics: Images Are More than Pictures, They Are Data. *Radiology*, 278(2):151169.

- Gjestebj, L., De Man, B., Jin, Y., Paganetti, H., Verburg, J., Giantsoudi, D., and Wang, G. (2016). Metal Artifact Reduction in CT: Where Are We After Four Decades? *IEEE Access*, 4:5826–5849.
- Gudbjartsson, H. and Patz, S. (1995). The Rician distribution of noisy MRI data. *Magnetic resonance in medicine*, 34(6):910–4.
- Hall, E. L., Kruger, R. P., Samuel, J., Dwyer, D., McLaren, R. W., Hall, D. L., and Lodwick, G. (1971). A Survey of Preprocessing and Feature Extraction Techniques for Radiographic Images. *IEEE Transactions on Computers*, C-20(9):1032–1044.
- Haralick, R. M., Shanmugam, K., and Dinstein, I. (1973). Textural Features for Image Classification. *IEEE Transactions on Systems, Man, and Cybernetics*, 3(6):610–621.
- Hatt, M., Majdoub, M., Vallières, M., Tixier, F., Le Rest, C. C., Groheux, D., Hindié, E., Martineau, A., Pradier, O., Hustinx, R., Perdrisot, R., Guillevin, R., El Naqa, I., and Visvikis, D. (2015). 18F-FDG PET uptake characterization through texture analysis: investigating the complementary nature of heterogeneity and functional tumor volume in a multi-cancer site patient cohort. *Journal of nuclear medicine*, 56(1):38–44.
- Hatt, M., Tixier, F., Pierce, L., Kinahan, P. E., Le Rest, C. C., and Visvikis, D. (2017). Characterization of PET/CT images using texture analysis: the past, the present... any future? *European journal of nuclear medicine and molecular imaging*, 44(1):151–165.
- Heiberger, R. M. and Holland, B. (2015). *Statistical Analysis and Data Display*. Springer Texts in Statistics. Springer New York, New York, NY.
- Janmahasatian, S., Duffull, S. B., Ash, S., Ward, L. C., Byrne, N. M., and Green, B. (2005). Quantification of lean bodyweight. *Clinical pharmacokinetics*, 44(10):1051–65.
- Khachiyan, L. G. (1996). Rounding of Polytopes in the Real Number Model of Computation. *Mathematics of Operations Research*, 21(2):307–320.
- Larue, R. T. H. M., van Timmeren, J. E., de Jong, E. E. C., Feliciani, G., Leijenaar, R. T. H., Schreurs, W. M. J., Sosef, M. N., Raat, F. H. P. J., van der Zande, F. H. R., Das, M., van Elmpt, W. J. C., and Lambin, P. (2017). Influence of gray level discretization on radiomic feature stability for different CT scanners, tube currents and slice thicknesses: a comprehensive phantom study. *Acta oncologica*, pages 1–10.
- Leijenaar, R. T. H., Nalbantov, G., Carvalho, S., van Elmpt, W. J. C., Troost, E. G. C., Boellaard, R., Aerts, H. J. W. L., Gillies, R. J., and Lambin, P. (2015). The effect of SUV discretization in quantitative FDG-PET Radiomics: the need for standardized methodology in tumor texture analysis. *Scientific reports*, 5(August):11075.
- Lewiner, T., Lopes, H., Vieira, A. W., and Tavares, G. (2003). Efficient Implementation of Marching Cubes' Cases with Topological Guarantees. *Journal of Graphics Tools*, 8(2):1–15.
- Lloyd, S. P. (1982). Least Squares Quantization in PCM. *IEEE Transactions on Information Theory*, 28(2):129–137.
- Lorensen, W. E. and Cline, H. E. (1987). Marching cubes: A high resolution 3D surface construction algorithm. *ACM SIGGRAPH Computer Graphics*, 21(4):163–169.

- Max, J. (1960). Quantizing for minimum distortion. *IEEE Transactions on Information Theory*, 6(1):7–12.
- Mazurowski, M. A., Czarnek, N. M., Collins, L. M., Peters, K. B., and Clark, K. (2016). Predicting outcomes in glioblastoma patients using computerized analysis of tumor shape: preliminary data. In Tourassi, G. D. and Armato, S. G., editors, *SPIE Medical Imaging*, volume 9785, page 97852T.
- Moran, P. A. P. (1950). Notes on continuous stochastic phenomena. *Biometrika*, 37:17–23.
- O’Rourke, J. (1985). Finding minimal enclosing boxes. *International Journal of Computer and Information Sciences*, 14(3):183–199.
- Schirra, S. (2008). How Reliable Are Practical Point-in-Polygon Strategies? In *Algorithms - ESA 2008*, pages 744–755. Springer Berlin Heidelberg, Berlin, Heidelberg.
- Shafiq-Ul-Hassan, M., Zhang, G. G., Latifi, K., Ullah, G., Hunt, D. C., Balagurunathan, Y., Abdalah, M. A., Schabath, M. B., Goldgof, D. G., Mackin, D., Court, L. E., Gillies, R. J., and Moros, E. G. (2017). Intrinsic dependencies of CT radiomic features on voxel size and number of gray levels. *Medical physics*, 44(3):1050–1062.
- Sled, J. G., Zijdenbos, A. P., and Evans, A. C. (1998). A nonparametric method for automatic correction of intensity nonuniformity in MRI data. *IEEE transactions on medical imaging*, 17(1):87–97.
- Sollini, M., Cozzi, L., Antunovic, L., Chiti, A., and Kirienko, M. (2017). PET Radiomics in NSCLC: state of the art and a proposal for harmonization of methodology. *Scientific reports*, 7(1):358.
- Solomon, C. and Breckon, T. (2011). Features. In *Fundamentals of Digital Image Processing*, chapter 9, pages 235–262. John Wiley & Sons, Ltd, Chichester, UK.
- Soret, M., Bacharach, S. L., and Buvat, I. (2007). Partial-volume effect in PET tumor imaging. *Journal of nuclear medicine*, 48(6):932–45.
- Stellinger, P., Latecki, L. J., and Siqueira, M. (2007). Topological equivalence between a 3D object and the reconstruction of its digital image. *IEEE transactions on pattern analysis and machine intelligence*, 29(1):126–40.
- Sun, C. and Wee, W. G. (1983). Neighboring gray level dependence matrix for texture classification. *Computer Vision, Graphics, and Image Processing*, 23(3):341–352.
- Thibault, G., Angulo, J., and Meyer, F. (2014). Advanced statistical matrices for texture characterization: application to cell classification. *IEEE transactions on bio-medical engineering*, 61(3):630–7.
- Todd, M. J. and Yldrm, E. A. (2007). On Khachiyan’s algorithm for the computation of minimum-volume enclosing ellipsoids. *Discrete Applied Mathematics*, 155(13):1731–1744.
- Unser, M. (1986). Sum and difference histograms for texture classification. *IEEE transactions on pattern analysis and machine intelligence*, 8(1):118–125.

- Vaidya, M., Creach, K. M., Frye, J., Dehdashti, F., Bradley, J. D., and El Naqa, I. (2012). Combined PET/CT image characteristics for radiotherapy tumor response in lung cancer. *Radiotherapy and oncology*, 102(2):239–45.
- Vallières, M., Freeman, C. R., Skamene, S. R., and El Naqa, I. (2015). A radiomics model from joint FDG-PET and MRI texture features for the prediction of lung metastases in soft-tissue sarcomas of the extremities. *Physics in medicine and biology*, 60(14):5471–96.
- Vallières, M., Kay-Rivest, E., Perrin, L. J., Liem, X., Furstoss, C., Aerts, H. J. W. L., Khaouam, N., Nguyen-Tan, P. F., Wang, C.-S., Sultanem, K., Seuntjens, J., and El Naqa, I. (2017). Radiomics strategies for risk assessment of tumour failure in head-and-neck cancer. *Scientific reports*, 7:10117.
- van Dijk, L. V., Brouwer, C. L., van der Schaaf, A., Burgerhof, J. G., Beukinga, R. J., Langendijk, J. A., Sijtsema, N. M., and Steenbakkers, R. J. (2017). CT image biomarkers to improve patient-specific prediction of radiation-induced xerostomia and sticky saliva. *Radiotherapy and Oncology*, 122(2):185–191.
- van Griethuysen, J. J. M., Fedorov, A., Parmar, C., Hosny, A., Aucoin, N., Narayan, V., Beets-Tan, R. G. H., Fillion-Robin, J.-C., Pieper, S., and Aerts, H. J. W. L. (2017). Computational Radiomics System to Decode the Radiographic Phenotype. *Submitted for publication*.
- van Velden, F. H. P., Cheebsumon, P., Yaqub, M., Smit, E. F., Hoekstra, O. S., Lammertsma, A. A., and Boellaard, R. (2011). Evaluation of a cumulative SUV-volume histogram method for parameterizing heterogeneous intratumoural FDG uptake in non-small cell lung cancer PET studies. *European journal of nuclear medicine and molecular imaging*, 38(9):1636–47.
- van Velden, F. H. P., Kramer, G. M., Frings, V., Nissen, I. A., Mulder, E. R., de Langen, A. J., Hoekstra, O. S., Smit, E. F., and Boellaard, R. (2016). Repeatability of Radiomic Features in Non-Small-Cell Lung Cancer [(18)F]FDG-PET/CT Studies: Impact of Reconstruction and Delineation. *Molecular imaging and biology*, 18(5):788–95.
- Wahl, R. L., Jacene, H., Kasamon, Y., and Lodge, M. A. (2009). From RECIST to PERCIST: Evolving Considerations for PET response criteria in solid tumors. *Journal of nuclear medicine*, 50 Suppl 1(5):122S–50S.
- Yan, J., Chu-Shern, J. L., Loi, H. Y., Khor, L. K., Sinha, A. K., Quek, S. T., Tham, I. W. K., and Townsend, D. (2015). Impact of Image Reconstruction Settings on Texture Features in 18F-FDG PET. *Journal of nuclear medicine*, 56(11):1667–73.
- Yip, S. S. F. and Aerts, H. J. W. L. (2016). Applications and limitations of radiomics. *Physics in medicine and biology*, 61(13):R150–66.
- Zhang, C. and Chen, T. (2001). Efficient feature extraction for 2D/3D objects in mesh representation. In *Proceedings 2001 International Conference on Image Processing*, volume 2, pages 935–938. IEEE.